Library note:

The following pages were not listed in the print copy this PDF was scanned from:

7, 24, 117, 133

VOLCANIC GEOLOGY AND PHYSICAL VOLCANOLOGY OF MOUNT MORNING, ANTARCTICA.

A thesis
submitted in partial fulfillment
of the requirements for the degree

of

Master of Science in Earth Science

at

The University of Waikato

By

TIMOTHY HUGH VAN WOERDEN

THE UNIVERSITY OF
WAIKATO
Te Whare Wānanga o Waikato

The University of Waikato
2006

ABSTRACT

Mount Morning is 70 km south of Ross Island and is part of the Cenozoic McMurdo Volcanic Group, which includes the presently active Erebus volcano. Few previous studies have investigated the mountain.

The main exposures occur on two ridges on the northwest of the mountain, the field area is a roughly 3x5 km area on the northern part of the Riviera Ridge. The exposed geology indicates two main episodes of volcanic activity; Miocene trachytes and trachyandesites and Quaternary basanites and phonolites.

This project is focused primarily on the Quaternary basanites and the objectives were:

- Describe the physical volcanology.
- Map and describe the surface geology and petrology and characterise the geochemistry of the rocks.
- Develop models for the origin and evolution of the magmas represented by the rocks.
- Characterise mantle xenoliths found in the area.

The Quaternary eruptives are represented by eroded scoria cone remnants, dikes, and lava domes and flows. Breccia pipes mark eroded vent areas. Four scoria cones have been mapped and sampled in detail and these are interpreted to have formed by hawaiian and strombolian style activity. They contain distinctive agglutinate beds which have formed lava flows as lapilli and spatter horizons have accumulated on the flanks of cones close to source.

The dominant rock-type is strongly porphyritic olivine and clinopyroxene basanite formed by crystal fractionation of olivine, clinopyroxene, opaque oxides, and minor amphibole, apatite and feldspar

A dike within one of the scoria cones contains a spectacular suite of abundant, large xenoliths. Ultramafic mantle xenoliths include peridotite and pyroxenites, crustal xenoliths are granulite and granite. The presence of these xenoliths indicates that some basanites are very primitive.

Acknowledgements

Spending a month in Antarctica carrying out the field work for this thesis was an incredible experience. I am incredibly lucky to have been given the opportunity to travel to such a unique and awe-inspiring environment.

To my companions during my time on Mount Morning, Richard, Alan and Adam, thank you for making it such an awesome and memorable time.

To Richard Price, Richard Smith and Roger Briggs, thank you for keeping me on track and providing lots of guidance and assistance with this project.

This research would not have been possible without the support of Antarctica New Zealand, I thank them and also the staff at Scott Base for the logistical support that enabled me to carry out my field work.

To all the staff in the Earth Science department, thank you for sharing your knowledge and enthusiasm for the earth sciences with all of us over the last few years.

A big thank you to everyone who assisted with my lab work, especially Renat Radosinsky, Ganqing Xu, Lorraine Paterson (University of Otago) for helping with microprobe analysis and Alan Greig (University of Melbourne) for carrying out the ICP-MS analyses.

Thanks to my family, Mum and Dad, Irene, and Oma and Opa, and also everyone else who has kept me motivated and encouraged (and distracted) me while I have been studying.

TABLE OF CONTENTS

APPENDICES

FIGURES

TABLES

CHAPTER FIVE

CHAPTER SIX

CHAPTER ONE - INTRODUCTION

1.1 MCMURDO VOLCANIC GROUP

The McMurdo Volcanic Group includes all the Cenozoic volcanic rocks found on the Western side of the Ross Embayment, Antarctica (*Kyle, 1990a*). These occur in a discontinuous volcanic belt over 2000 km long parallel to both the Transantarctic Mountains and Ross Sea Embayment (*Wörner, 1999*). Figure 1.1 shows the main occurrences of the McMurdo Volcanic Group rocks.

Within the McMurdo Volcanic Group are three distinct volcanic provinces (*Wörner, 1999*);

- Hallet
- Melbourne
- Erebus

The Hallet Province is the northernmost of the three and is a 260km chain of both on and offshore volcanoes along the Ross Sea coast in northern Victoria Land (*McIntosh and Kyle, 1990*).

The Melbourne province contains four main volcanic fields within which there are several large stratovolcanoes, including Mount Melbourne and Mount Overlord near the north end of the Terror Rift (*Kyle, 1990c*).

The Erebus Province is the southernmost province and most volcanics are found in two volcanic fields at the south end of the Terror Rift, centered around Mount Erebus on Ross Island and Mount Discovery 70 km SE of Ross Island on the mainland.

The Balleny Islands lie several hundred kilometers northeast of Victoria Land (*Verwoerd et al, 1990*) and were originally included as a fourth province of the McMurdo Volcanic Group. (e.g. in Kyle and Rankin, 1976) but they have since been excluded because they are geographically and tectonically unrelated to the other

McMurdo Volcanic Group rocks (*Kyle, 1990a*). They are believed to be related to a separate deep mantle plume source (*Lanyon et al., 1993*).

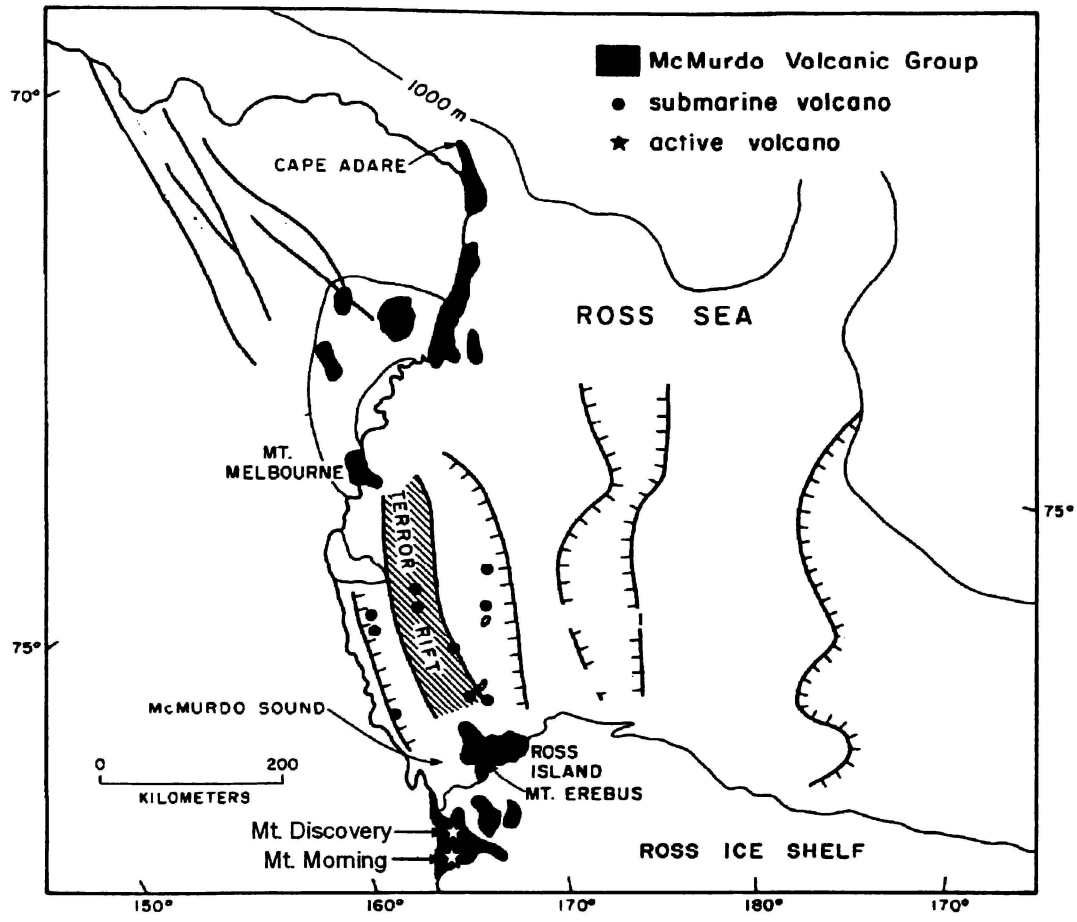

Fig. 1.1: Map showing the distribution of the McMurdo Volcanic Group rocks on the western side of the Ross Embayment and the Erebus Province at the southern end of the Terror Rift (adapted from *Kyle, 1990a*).

1.2 WEST ANTARCTIC RIFT SYSTEM

The Ross Sea Rift is an active zone of extension and subsidence between Marie Byrd Land and the Transantarctic Mountains (*Wörner, 1999*). The rift system measures about 3200 x 880 km and is depicted in Figure 1.2 as the large trough linking the Bellinghausen and Ross Seas (*LeMasurier, 1990*). Lithospheric thinning is indicated by the large basins making up the rift, each bounded by a system of ridges and grabens. The crust is 40-45 km thick under the Transantarctic Mountains but is thinned to 17-20 km under the Ross Sea (*Wörner, 1999*). The deepest of these grabens is the Terror Rift next to the Transantarctic Mountains.

Volcanism occurs on the east side of Marie Byrd Land and on the west side of the rift adjacent to the Transantarctic Mountains (*Wörner, 1999*).

The cross-section in Figure 1.3 shows the occurrence of volcanism on the thinned crust between the Transantarctic Mountains and the Terror Rift

The distribution of the McMurdo Volcanic Group is tectonically controlled by both the uplift of the Transantarctic Mountains and basin subsidence in the Ross Embayment (*Kyle, 1990a*). Volcanoes of the Erebus Province are possibly associated with crustal fractures and faults developed during earlier uplift and rifting. (*Kyle, 1981*)

Rifting in the Ross Embayment began around 95 Ma, following the breakup of Antarctica and Australia, but most activity has occurred since the Cenozoic. The Transantarctic Mountains are the uplifted shoulder on the margins of the rift and have formed since 60 Ma, probably in several separate phases of tectonism (*Wörner, 1999*). At the same time as the Transantarctic Mountains were being formed rifting and stretching was continuing in the Ross Sea and Marie Byrd Land reached its

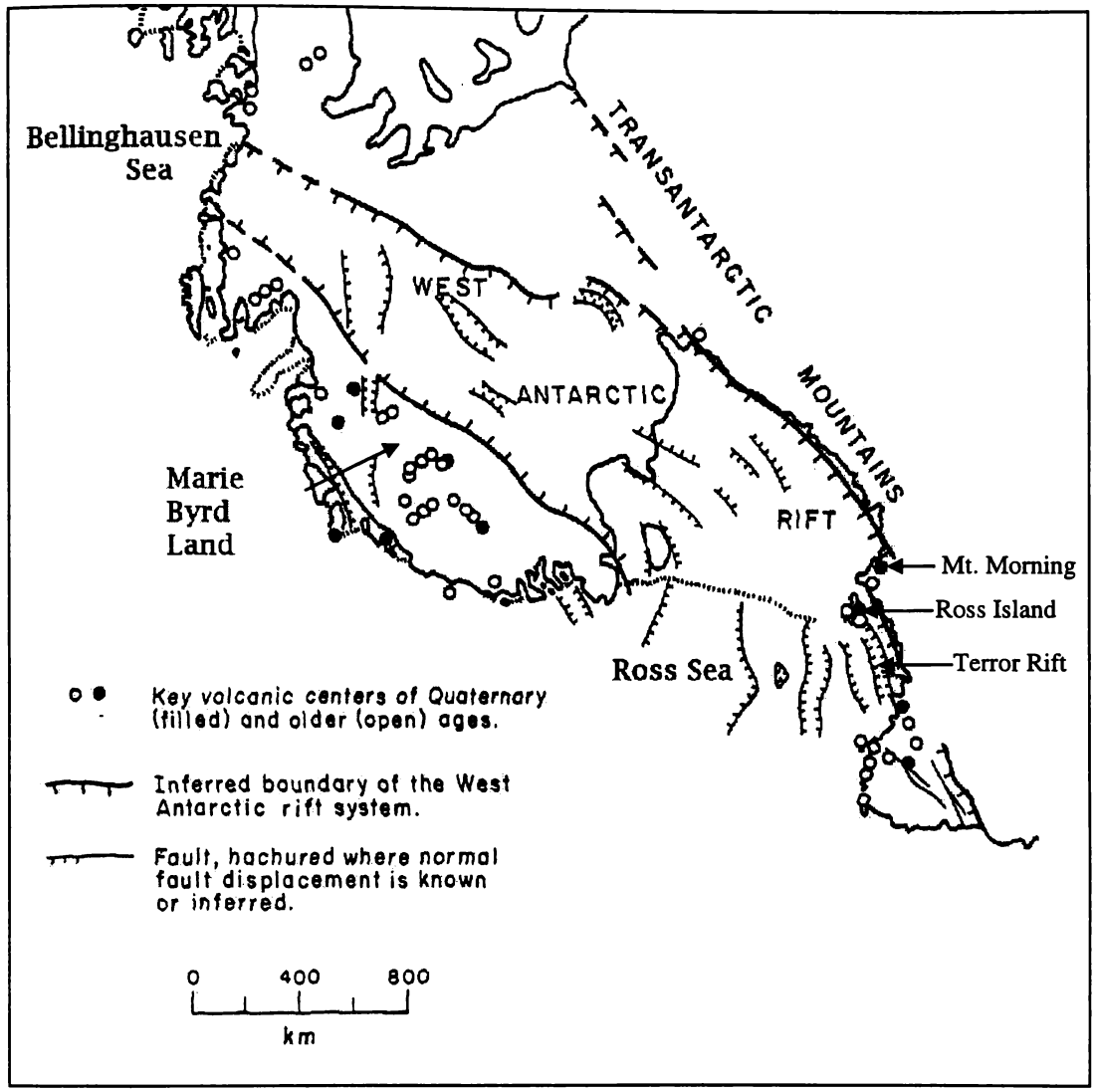

Fig.1.2: The West Antarctic Rift system (adapted from *LeMasurier, 1990*).

current position during the early Cenozoic (*Lawver, 1991*). There is possibly as much as 20 km of crustal offset between the uplifted Transantarctic Mountains and the subsiding Basins in Ross Sea (*Wörner, 1999*). Volcanism post-dates mountain building and early rifting and the volcanoes of the Erebus Province are possibly associated with crustal fractures and faults that have been present since the earlier uplift and rifting phase (*Kyle, 1981*).

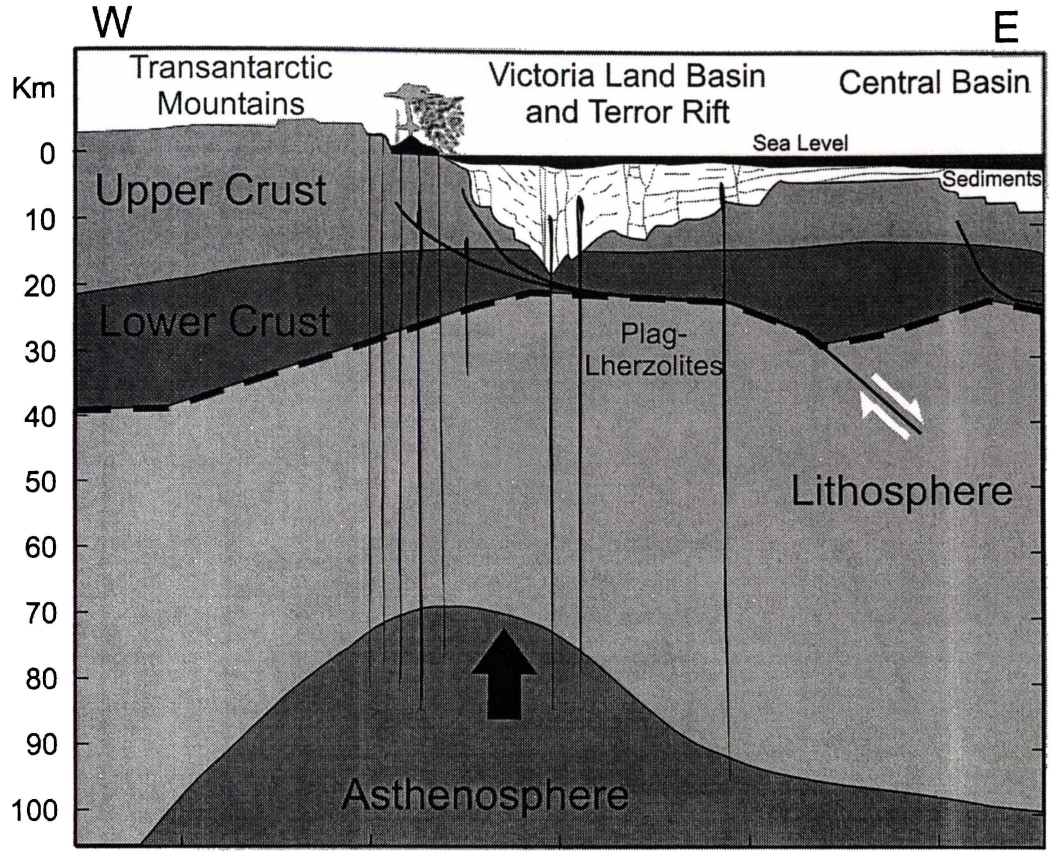

Fig.1.3: Cross section from the Transantarctic Mountains to the Terror Rift and Victoria Basin (Redrawn from *Wörner, 1999*).

1.3 EREBUS PROVINCE

The Erebus Volcanic Province is the most studied of the provinces in the McMurdo Volcanic Group; the earliest studies were those carried out by members of Scott's and Shackleton's expeditions in the early 1900's (*Kyle, 1990b*). Most volcanism in the Erebus Province has occurred in two subprovinces; Ross Island and Discovery. There are other minor occurrences in the Dry Valleys, Royal Society Ranges and several magnetic anomalies in the western Ross Sea may indicate the presence of volcanic rocks (*Kyle, 1990b*).

The Antarctic and subantarctic volcanoes are dominantly alkaline and are dominated by basaltic products, which make up over 70 % of the total erupted volume (*LeMasurier, 1990*). The most common rocks within the Erebus province

are basanites, phonolites and trachytes (Fig.1.4) but some intermediate compositions also occur (*Kyle, 1990b*).

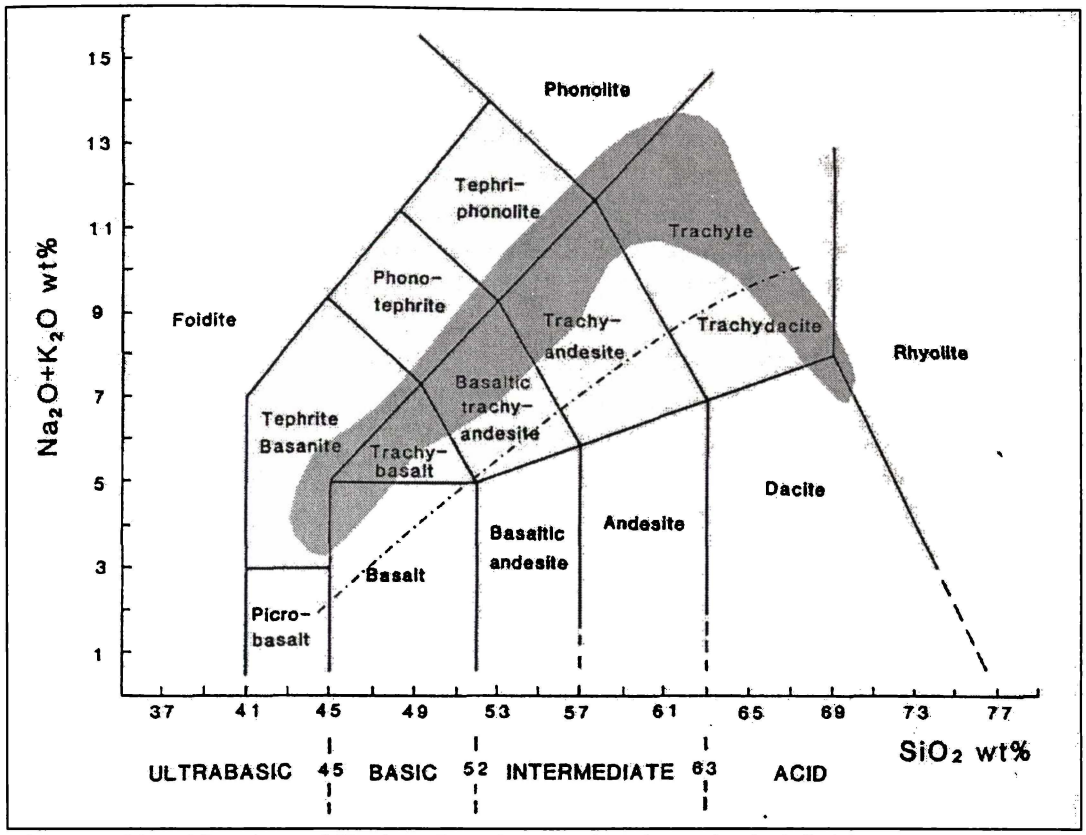

Fig.1.4: Classification of Erebus Province volcanics (shaded field) on a total alkali silica diagram. Dot-dashed line shows alkali/subalkali field boundary of Irvine and Baragar (*1971*). (Adapted from *LeBas et al., 1986* and *LeMasurier, 1990*)

Several magmatic lineages are represented in the Erebus Province. Rocks younger than 11 Ma are generally part of a basanite-tephrite-phonolite trend and have been subdivided into the Dry Valley Drilling Project and Erebus lineages (*Kyle, 1981*). The older (>11 Ma) rocks are mostly trachytic but fractionation trends are poorly defined because of the lack of exposure of these rocks. There are only three locations where trachytic rocks are found; Mason Spur and Riviera and Hurricane Ridges on Mount Morning (*Kyle, 1990b*).

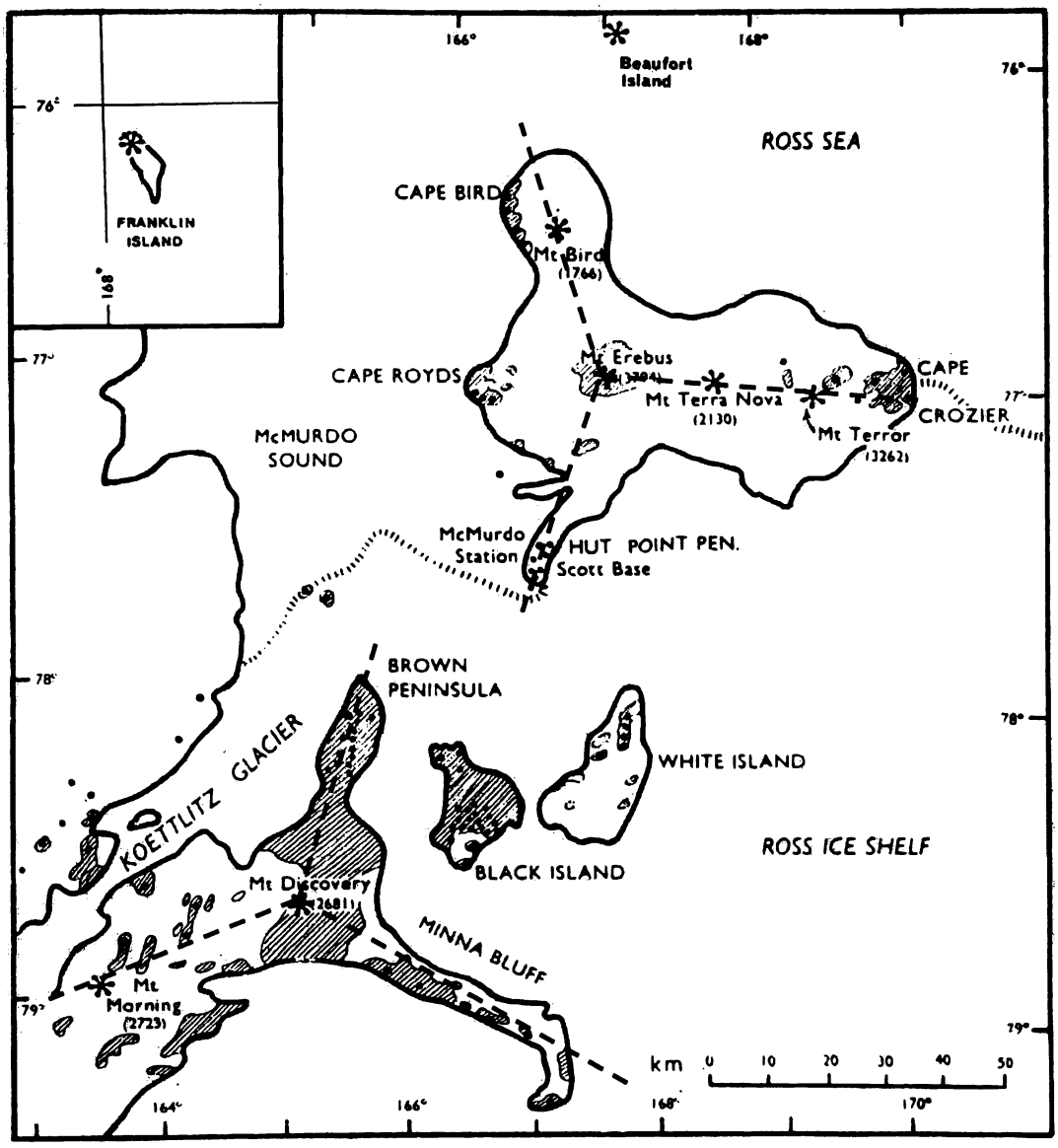

Fig.1.5: Erebus and Discovery volcanic centres showing the distribution of the main areas of volcanism and possible radial symmetry about Mounts Erebus and discovery. Adapted from Kyle and Cole *(1974).*

Volcanic glass in drill cores from McMurdo Sound indicates volcanism and erosion occurring back to the early Oligocene (~40 Ma) (*Kyle, 1990b*). The oldest surface exposures in the province are eroded trachyte centers ranging in age from 19-12 Ma on the lower slopes of Mount Morning at Gandalf Ridge, Riviera Ridge and Mason Spur (*Kyle, 1990b*).

Generally the ages of basanitic-phonolitic volcanics in the Discovery subprovince are greater than 4.5 Ma;

- Minna Bluff. 11.0 – 9.0 Ma (northern end)
  8.7 - 7.3 Ma (centre)
- Black Island 10.9 Ma (northern end)
- Mount discovery 5.3 – 4.4 Ma

The ages of volcanics in the Erebus subprovince are younger;

- Mount bird 4 – 3 Ma
- Mount Terror 2 – 0.6 Ma
- Hut Point Peninsula 1.8 – 0.4 Ma
- Mount Erebus >1 Ma

These age distributions agree well with Kyle's *(1990b)* suggestion of a mantle plume migrating from the Discovery to Erebus centre.

There has also been more recent volcanic activity in the Discovery subprovince at;

- Black Island 3.8 – 3.4 Ma
- Brown Peninsula 2.8 – 2.0 Ma
- Mount Morning > 2 Ma
- White Island 0.2 Ma

The volcanic centers in the McMurdo Volcanic Group and the Erebus Province contain many types of volcanic structures and landforms. Kyle (*1990a*) grouped these into three general types;

- Basaltic shield volcanoes
  e.g. Mount Bird and Mount Terror
- Stratovolcanoes, mainly trachytic or phonolitic
  e.g. Mount Discovery, Mount Erebus, Mount Morning

All reported ages are from Kyle, 1990*b*

- Basaltic scoria cones and flows, usually small and isolated but also occurring on the slopes of larger shield volcanoes and stratovolcanoes.

1.4 Mount Morning

There has been little previous geological investigation on Mount Morning. The existing literature includes the theses of Muncy *(1979)* and Wright-Grassham *(1987)* and a summary of all investigations prior to 1987 by Wright and Kyle *(Kyle, 1990b)*. The latter was published as a report in "Volcanoes of the Antarctic Plate and Southern Oceans", edited by LeMasurier and Thompson (*1990*). There have also been several reports on the wider McMurdo Sound area that have mentioned Mount Morning. For example Kyle *(1976)* investigated the mineralogy and geochemistry of the McMurdo Group Volcanic rocks including several samples from Mount Morning and Armstrong (*1978*) carried out K-Ar dating of McMurdo Group Volcanic rocks and included two samples from Mount Morning in his study.

Much of the mountain has a permanent snow and ice cover but there are good exposures on Riviera and Hurricane Ridges on the NE slopes of the mountain, and on the upper mountain (Fig. 1.6).

The geology exposed on the mountain records two main episodes of volcanic activity - Miocene and Quaternary. Miocene rocks are present as eroded subvolcanic trachyte and trachyandesite complexes on the lower mountain at Riviera Ridge and Gandalf Ridge (Fig.1.7). At Gandalf Ridge they unconformably overlie and cut Koettlitz Group basement units. The Miocene outcrops on Riviera Ridge are overlain unconformably by alkali basalt–trachyandesite domes and flows (*Wright and Kyle, 1987*).

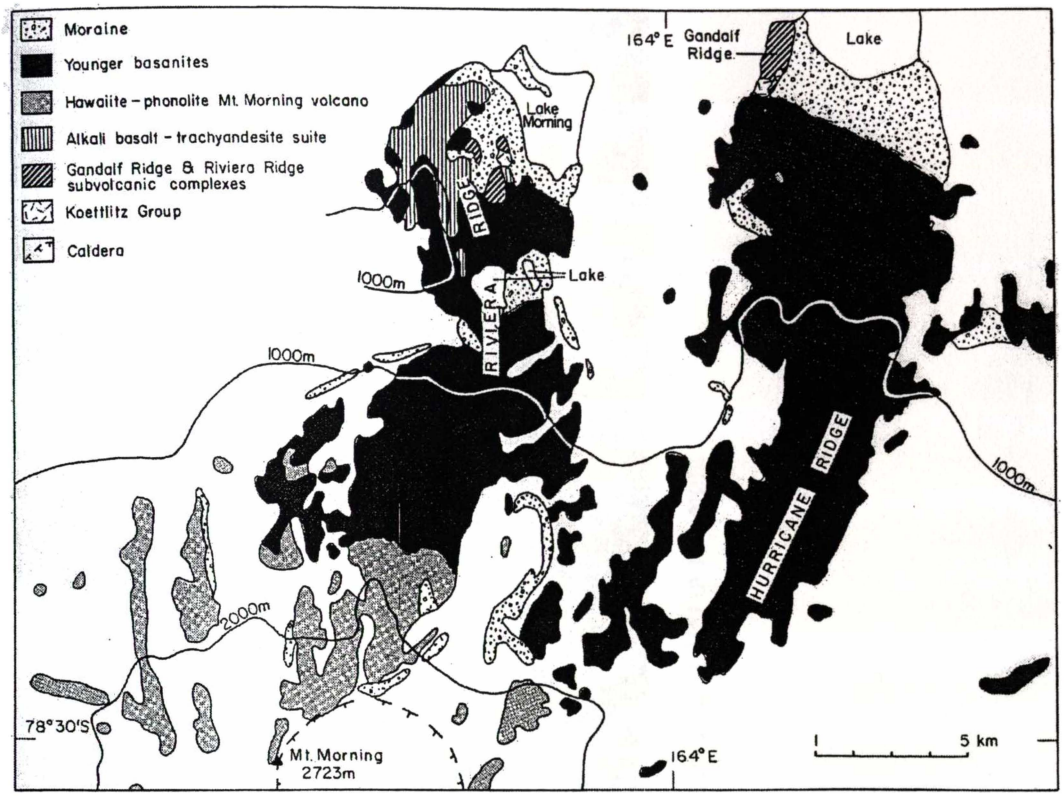

Fig.1.6: Geological map of Riviera and Hurricane Ridges, Mount Morning (*Wright and Kyle, 1987*).

The upper mountain is Quaternary in age *(Wright and Kyle, 1987).* There is a summit caldera 2 km wide and several phonolite domes occur on the upper slopes. The youngest volcanic products found on the mountain are Quaternary basanite cinder cones and lava flows found on Riviera and Hurricane Ridges (*Wright and Kyle, 1987*).

Wright and Kyle (*1987*) reported representative geochemical analyses and alkali-silica plots for samples of older (>11 Ma) and Quaternary volcanic rocks from Mount Morning. All data given are from the work of Muncy and Wright-Grassham. These show two distinct geochemical trends for each volcanic episode. The data for the older rocks define separate peralkaline and non-peralkaline trends, while the younger rocks form a basanite-phonolite trend.

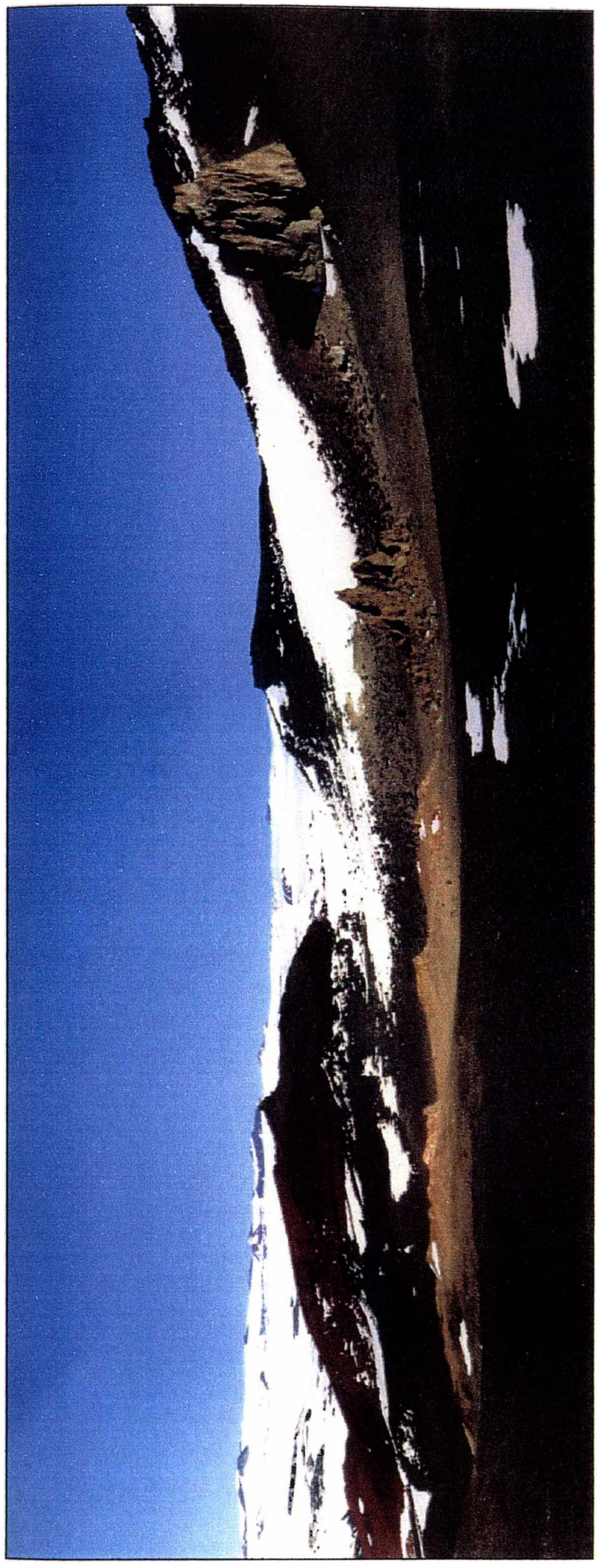

Fig.1.7: Trachyte pinnacles on Riviera Ridge. The largest pinnacle is estimated at 100 m in height.

CHAPTER TWO PHYSICAL VOLCANOLOGY

2.0 INTRODUCTION

This chapter concentrates on the structure and stratigraphy of the scoria cones within the field area, based on detailed stratigraphic columns made through the pyroclastic units of two typical, well exposed cones. Other associated features of the field area will also be discussed such as;

- lava flows
- lava domes
- dikes and sills
- vent breccias

Basanitic scoria cones are common on the lower slopes of the large phonolitic stratovolcano, Mount Morning. More than forty scoria cones or eroded cone remnants were observed during field work on the lower parts of Riviera and Hurricane Ridges. Four of these scoria cones occur within the field area covered by this study, all are glacially eroded remnants. The locations of these cones and other features of the field area are shown in Figure 2.1. Scoria Cones 1, 2 and 4 are extensively eroded, probably due to glacial activity. Erosion by glacial activity is interpreted because of the presence of striated surfaces and numerous erratic boulders, the largest erratic seen is shown in Figure 2.2.

All photos by T. vanWoerden unless noted otherwise.

Fig.2.1: Physical volcanology of part of Riviera Ridge, Mount Morning, Antarctica.

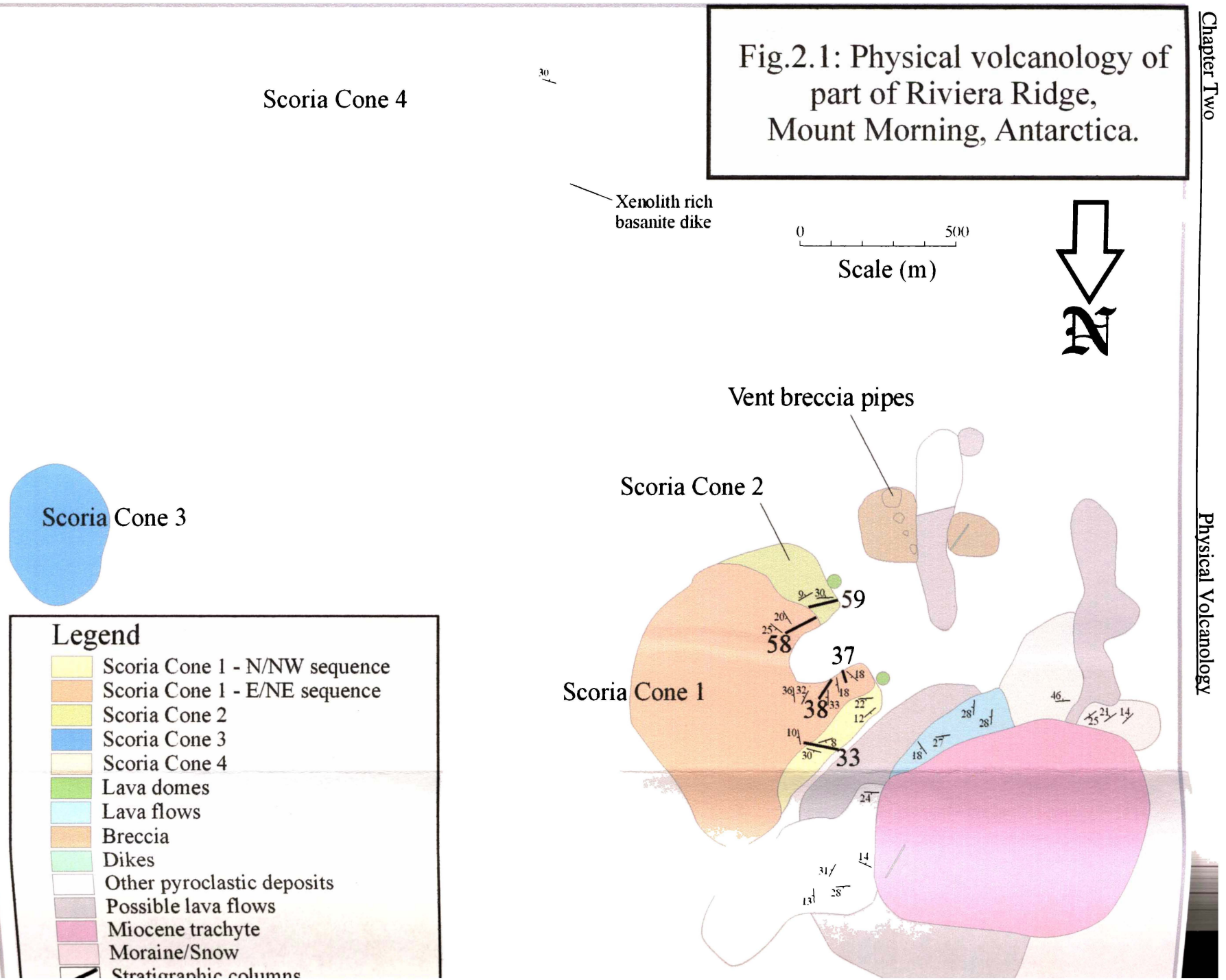

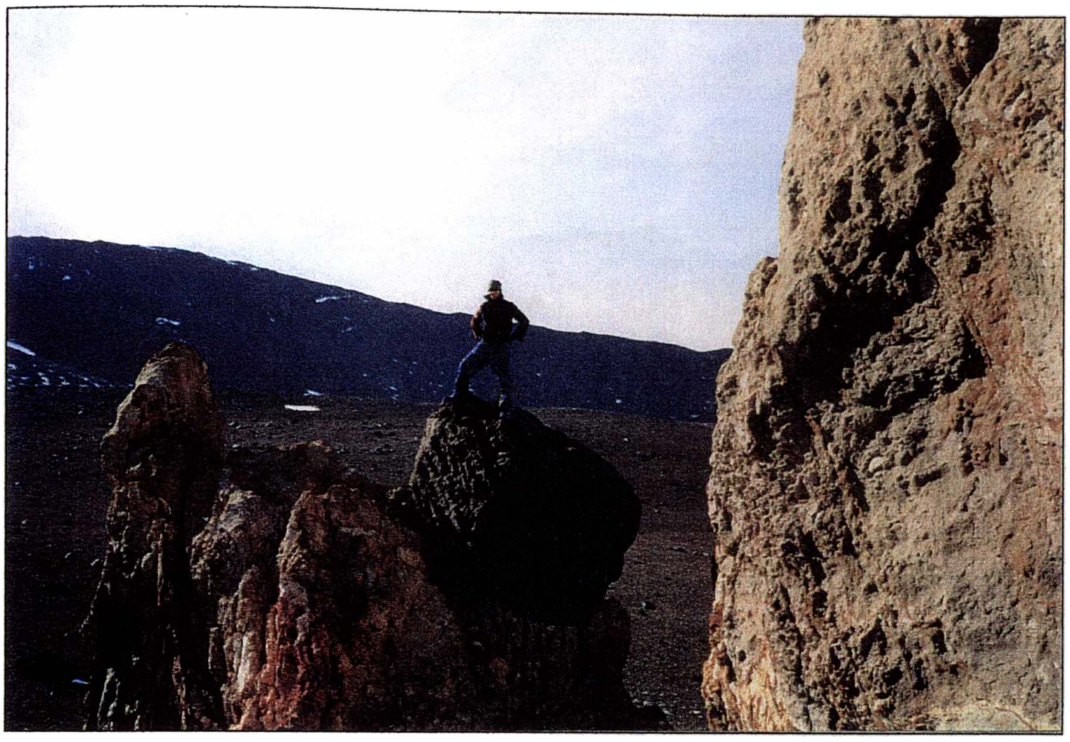

Fig.2.2: Large basaltic glacial boulder in an outcrop of trachyte.

2.1.1 SCORIA CONES

2.1.1.A SCORIA CONE 1

Scoria cone 1 is the largest in the field area, approximately 1 km in length. Four detailed stratigraphic sections (Figs. 2.17, 21, 25, 27) were described and drawn through the exposed pyroclastic sequences on the eastern and southern sides of this cone at locations 33, 37, 38 and 58 (Fig.2.1). The typical units of this cone are red brown and partially-densely welded with small bombs in a lapilli matrix. Two pyroclastic sequences are identified, one dipping towards the north and northwest and a sequence of units dipping towards the east and northeast. The basal contact of the northwest dipping sequence with the underlying geology is obscured by moraine and snow. The east and northeast dipping sequence unconformably overlies the northwest dipping sequence at Location 33 and overlies Scoria Cone 2 at Location 58.

Fig.2.3: The northernmost part of Scoria Cone 1, and Scoria Cone 2 viewed from the northwest. On the left are the northeast dipping units 58*a-k* of Scoria Cone 1 and on the right are the south to southwest dipping units of Scoria Cone 2.

2.1.1.B SCORIA CONE 2

This eroded scoria cone remnant underlies Scoria Cone 1, separated by an angular unconformity. A stratigraphic section was described and drawn (Fig. 2.30) through the pyroclastic sequence exposed on the western side of the cone. This scoria cone is characterised by a sequence of alternating agglutinated grey-brown units and bright red spatter units. The most distinctive of these agglutinate beds are in the upper units 59*a* and 59*b* and seen in Figure 2.4 as the gray bands near the top of the outcrop

Fig.2.4: Scoria Cone 2 viewed from the west. The pale layers near the top of the sequence are the agglutinate beds near the top of Unit 59*a*.

2.1.1.C SCORIA CONE 3

This cone is found on the eastern edge of the field area. It consists of two adjacent scoria cones, one of these is relatively intact and the other is extensively eroded. These cones are constructed from coarsely bedded spatter deposits containing large (up to 50 cm) bombs and thick coalesced agglutinate beds. Small (<1 cm) peridotite, pyroxene megacrysts and gabbro xenoliths were found.

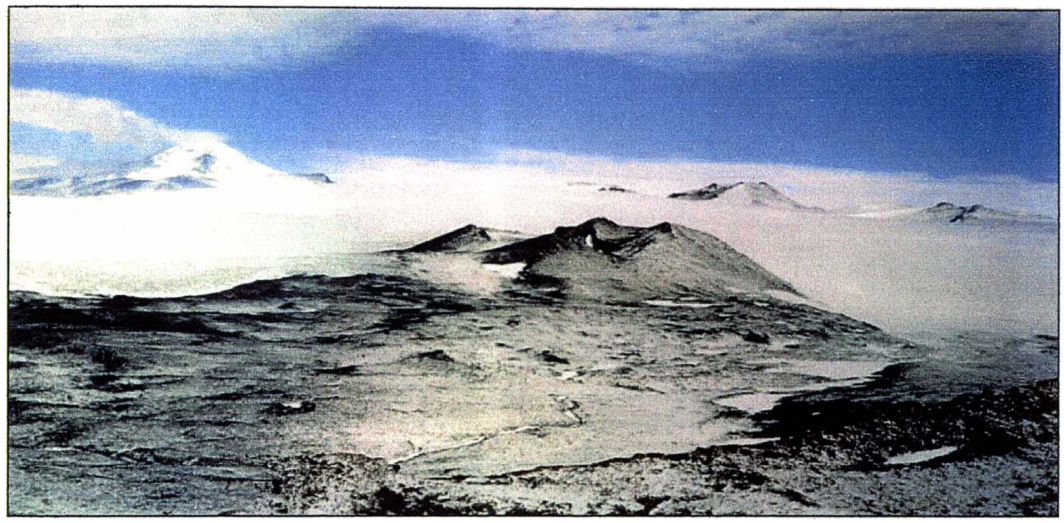

Fig.2.5: Scoria Cone 3 viewed from the west.

2.1.1.D SCORIA CONE 4

This cone is large and partially eroded, the exposed units dip towards the south and southeast. The basal contact is with pale orange brown breccia, which could be the underlying geology or a breccia from an initial vent clearing eruption. Mantle and lower crustal xenoliths are common as bombs in pyroclastic units and as inclusions in a large dike that occurs on the western side of the cone (Figs. 2.9, 5.6). The uppermost surface of the cone is a non-welded pyroclastic deposit containing very large breadcrust, spindle and ribbon bombs up to 1.5 m in size (Fig.2.7). The presence of these large bombs indicates proximity to a vent.

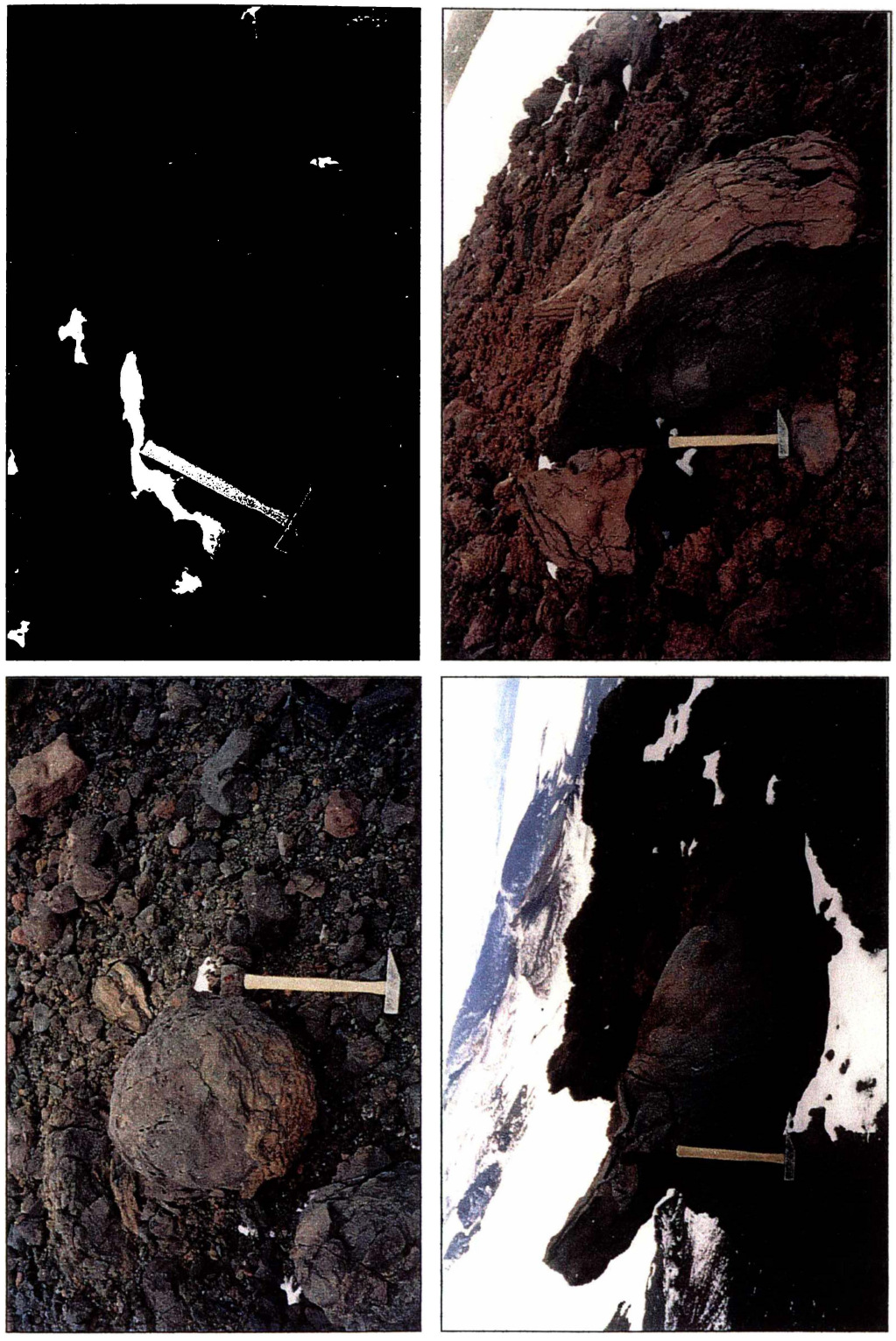

Fig.2.7: Large breadcrust (*a, b*) and spindle (*c, d*) bombs on the upper surface of scoria cone 4

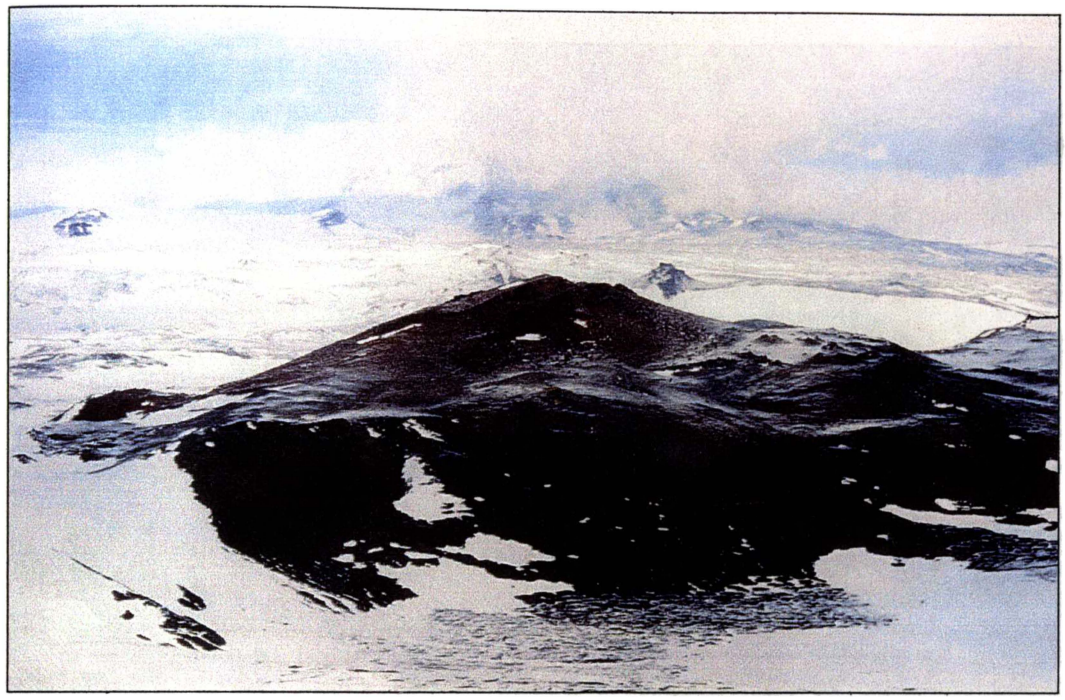

Fig.2.6: Scoria Cone 4 viewed from the south. (photo: A Martin)

2.1.2 LAVA FLOWS

There are two large lava flows in the field area, found next to each other at locations 3 and 4, separated by an 8 m thick pyroclastic deposit. The lower and upper flows are 8 and 5 m thick respectively and both have rubbly 'a'a type upper and lower margins up to 1.5 m thick enclosing a dense slightly jointed interior (Fig.2.8). Both flows are characterised by the occurrence of lower crustal xenoliths ranging in size from 1-20 cm (e.g. Fig.5.4).

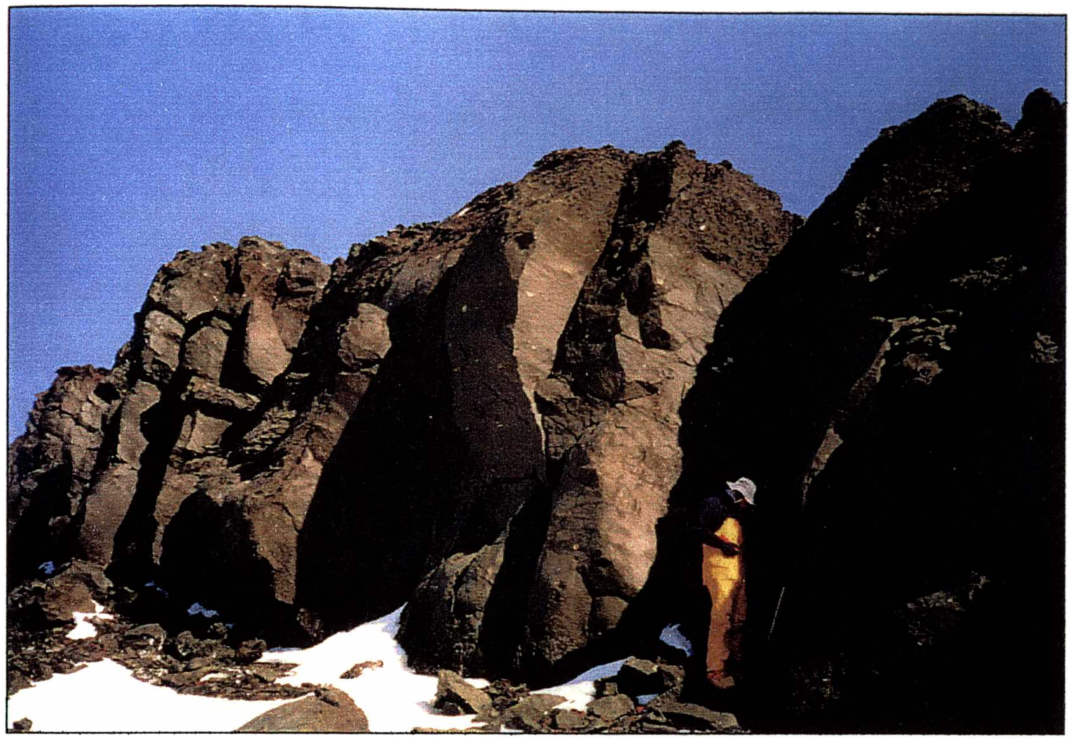

Fig.2.8: Thick jointed basanite lava flow at Loc 3.

2.1.3 LAVA DOMES

Three lava domes were identified in the field area, all roughly circular in shape with diameters estimated at 20-40 m (e.g. Fig. 2.9). The domes lie on the flanks of eroded scoria cones and appear to have been extruded following erosion of these cones. The dome adjacent to Scoria Cone 2 has been partially eroded to expose three dikes crosscutting it, possibly these were part of the feeder structures to the dome. This may indicate two episodes of erosion; the first occurring after the formation of the scoria cone but before dome emplacement and the second following the formation of the lava dome.

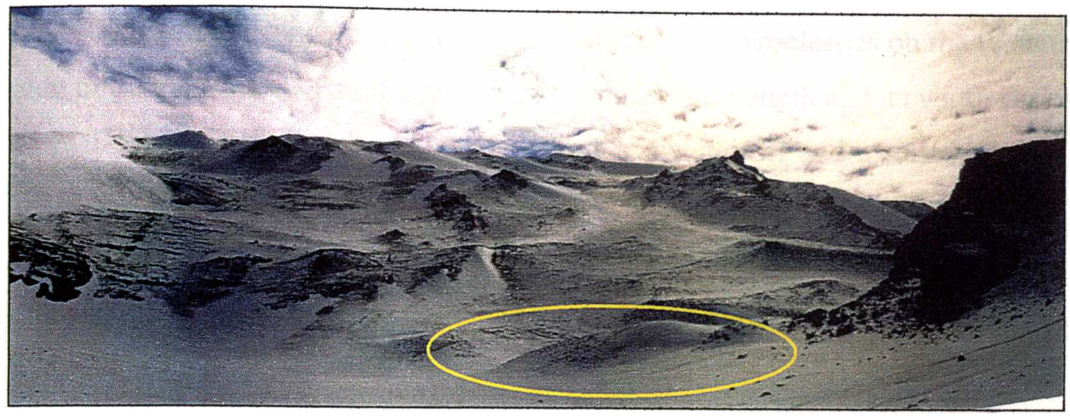

Fig.2.9: Lava dome adjacent to Scoria Cone 1 (circled).

2.1.4 DIKES

There are three large and many small dikes are found in the field area. Most of these have fine grained chilled margins and a rubbly interior.

Fig.2.10: Dike on Scoria Cone 4 showing abundant mantle and crustal xenoliths (photo: R. Price)

The largest dike is found intruded through breccia and pyroclastics on the western side of Scoria Cone 4. This dike is estimated at 1 km in length and its width varies from 1-5 m. There are several smaller dikes branching off and a series of small dikes *en echelon* to it. Mantle xenoliths are abundant in this dike (Figs. 2.9, 5.6) and suggest that this dike is a feeder structure to the vent that produced the adjacent pyroclastic deposits containing many mantle xenolith cored bombs.

The two other large dikes are each several hundred meters long and have a width of 0.5-1 m. One of these is intruded into breccia on the western ridge (Loc. 99) and the other into trachyte to the north of the field area (Loc. 23).

2.1.5 VENT BRECCIA

Four outcrops of a brown coloured breccia form a roughly north-south lineament approximately 500 m long. The largest outcrop is approximately 20-30 m tall and 100 m wide (Fig. 2.11).

Fig.2.11: The largest of four breccia outcrops. (photo A. Martin)

Both light and dark brown variations are seen in the breccia. The dark brown breccia has a 1-10 mm matrix containing abundant basanite clasts up to 40 cm, with some of these showing evidence for recycling. The lighter brown breccia is finer grained and contains fewer and smaller bombs. Both breccia types also contain inclusions of gabbro and phonotephrite and megacrysts of pyroxene. The majority of the breccia is massive, but some discontinuous layering occurs at a scale of tens of centimeters to meters and occasional fine grained laminations are found.

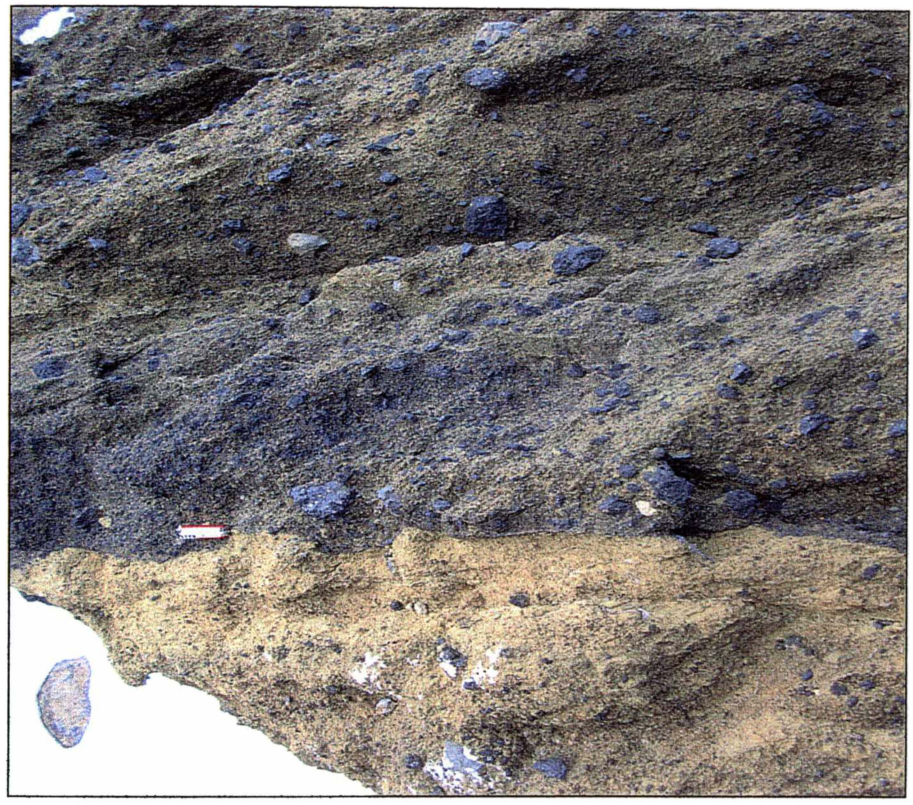

Fig.2.12: Part of breccia outcrop showing a contact between the light and dark breccia types. (photo: R. Price)

The largest breccia outcrop contains a dike and a sill of basanitic composition. The dike is sinuous and stretches for over 20 m up the face of the outcrop with a variable width of up to 1 m. The sill is approximately 80 cm thick. Fine grained veining occurs at several places in the breccia, which may be gas escape structures.

2.2 STRATIGRAPHY OF SCORIA CONE 1

2.2.1 UNIT 34

The stratigraphically lowest unit found on this scoria cone is a dark grey, westwards dipping, pyroclastic deposit found at Location 34. This unit consists of well sorted, fine-medium grained, olivine rich basanitic lapilli. Very weathered red-brown basaltic bombs are common, up to 60 cm in size. Some well developed bedding is seen, with partially welded layers approximately 25 cm thick separated by coarser non-welded subunits approximately 5 cm thick. This very dark unit is unlike any others found elsewhere on Scoria Cone 1 so may be part of an underlying sequence, or a lithic rich deposit from an initial vent clearing eruption

2.2.2 STRATIGRAPHIC COLUMN AT LOCATION 33

This column is described from the prominent cliffs on the northwestern side of Scoria Cone 1 and summarised in Figure 2.18. The stratigraphic column is a composite of four subsections and depicts approximately 28 m of section (Figs 2.13, 14). Thirteen pyroclastic units are identified, these are distinguished by colour, grain size, sorting, degree of welding and grading. Most units are red brown pyroclastic deposits, partially to densely welded, with large grey, scoriaceous, basanitic bombs and occasional blocks, in a matrix of fine-medium lapilli. The matrix in these units is olivine and pyroxene rich, although olivine crystals are hard to identify because they are weathered to a dark red colour. The matrix appears to be the same composition as the bombs and blocks.

Welding terms:

- non-welded - loose, non-resistant deposits
- partially welded - resistant, no/little deformation of bombs
- densely welded - resistant, bombs generally deformed
- extremely welded - very resistant and dense, individual grains are difficult to identify

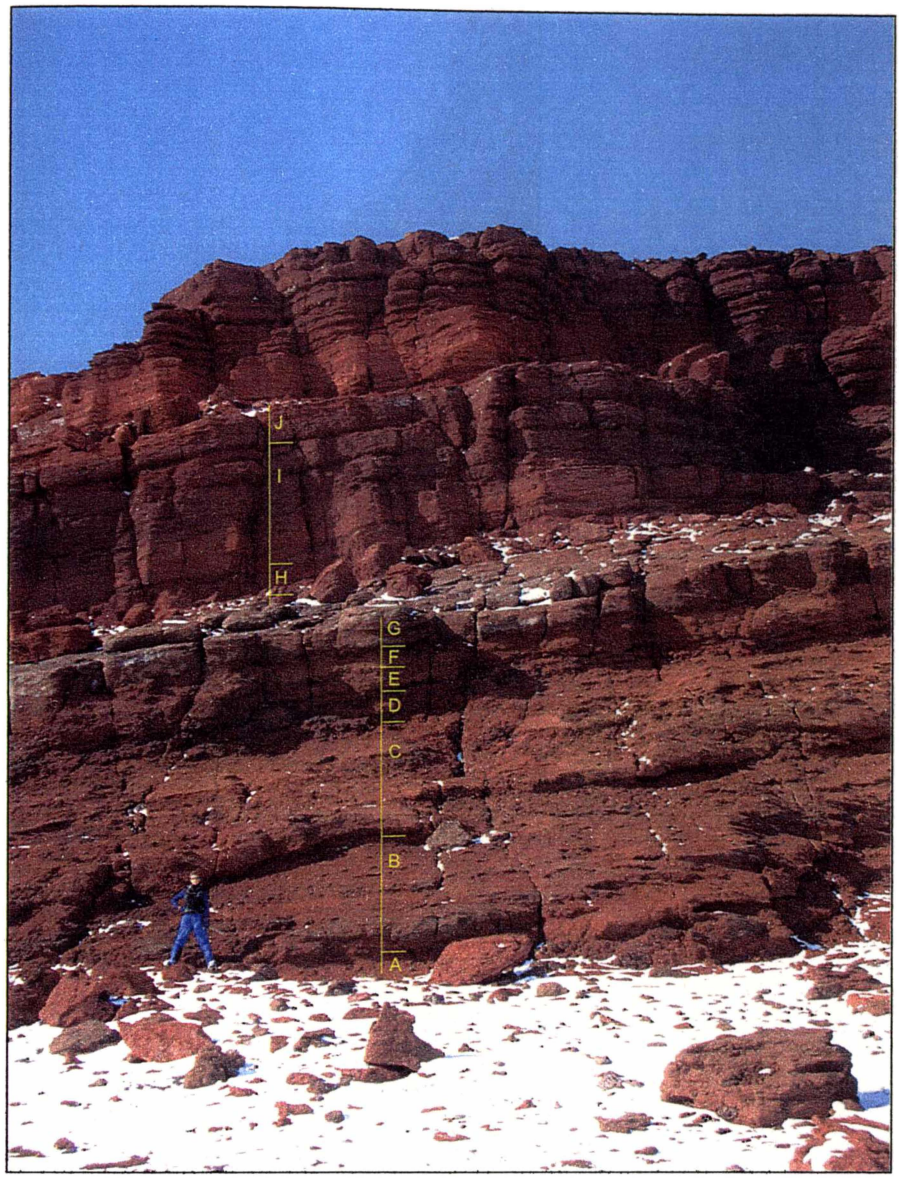

Fig.2.13: The lower part of the stratigraphic column described and drawn at location 33 showing units 33*a-j*.

Unit 33*a*

This is the lowest unit in the section logged at Location 33. It is a red brown partially-densely welded pyroclastic unit at least 1 m thick, and the lower contact lies beneath a cover of moraine and snow so cannot be identified. The unit is supported by a matrix of fine-medium lapilli (2-10 mm). Some of these fragments show ragged spatter and fluidal morphologies. Occasional vesicular basanitic bombs up to 20 cm occur.

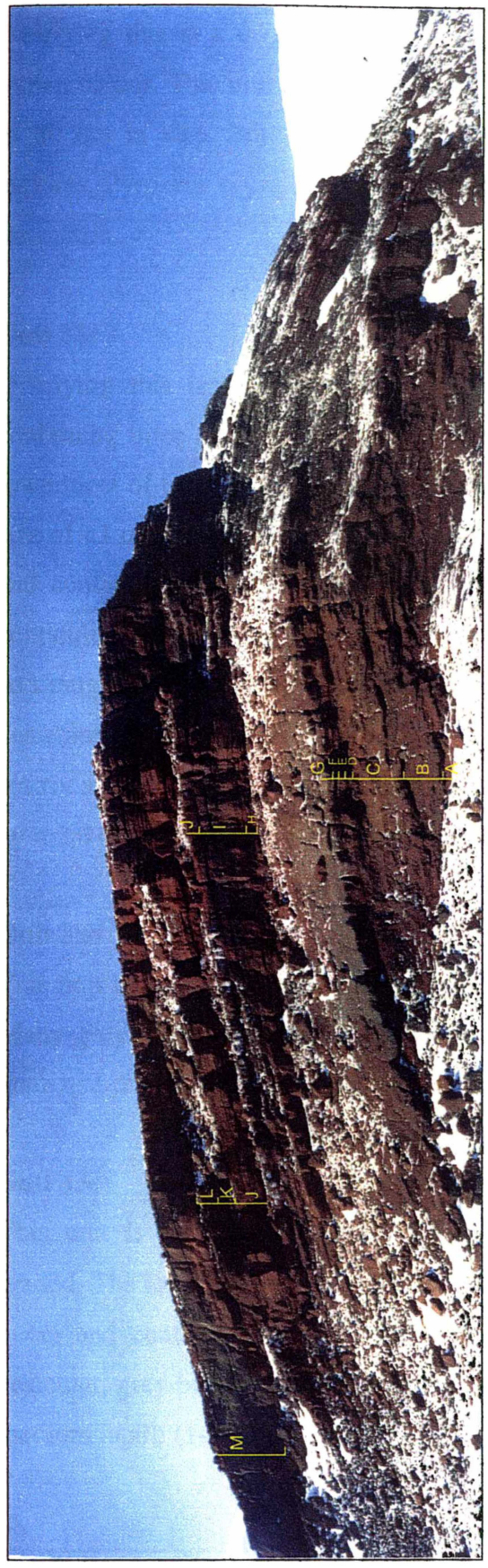

Fig.2.14: Scoria cone 1 at Location 33, showing the stratigraphic column described and drawn.

Unit 33*b*

Overlying this is a 0.75 m thick densely welded unit with a mottled red grey brown colour. This unit has a matrix of fine-medium lapilli supporting bombs up to 50 cm in size. Both the matrix clasts and the bombs have ragged spatter textures. Pyroxene crystals up to 3 mm and granite clasts up to 5 cm are found in the matrix.

Unit 33*c*

Overlying this is an orange buff coloured, partially to densely welded unit containing three reversely graded subunits; $33c_1$, $33c_2$ and $33c_3$. Unit $33c_1$ is the lowermost of these three subunits (Fig. 6.6). The base of this subunit has a grain size of <1 mm and this grades up over a height of 25 cm to a matrix of up to 3 cm and containing vesicular bombs up to 10 cm in size. This unit is very porous, containing many spaces between the matrix grains. Unit $33c_2$ is 50-60 cm thick and ranges from a coarse ash at its base up to a coarse pebbly matrix containing vesicular bombs up to 50 cm. Unit $33c_3$ is 60 cm thick and grades from a 2-3 mm matrix at its base, up to a 5-50 mm matrix containing blocks and vesicular bombs up to 50 cm of pyroxene rich basanite.

Unit 33*d*

This unit is a poorly sorted, densely welded, coarse pyroclastic unit 80 cm thick. Many grey brown vesicular pyroxene basalt bombs up to 40 cm are found in a matrix of red-brown fine-medium lapilli (5-30 mm).

Unit 33*e*

This unit is 50 cm thick, red brown, partially-densely welded and reversely graded. The lower 10 cm is coarse ash (1-2 mm), the centre 15 cm is coarser at 1-3 cm and contains grey vesicular bombs up to 2 cm. The upper 25 cm has vesicular, grey brown, slightly deformed basanitic bombs up to 30 cm set in fine-medium lapilli (1-5 mm).

Unit 33*f*

This unit is 50 cm thick, pale red brown, partially to densely welded and showing a hint of reverse grading. The lower 5 cm of the unit is coarse ash (0.5-2 mm) in size. This rapidly grades up into a homogenous, very poorly sorted subunit of pyroxene rich basanite blocks and bombs up to 30 cm supported in a 2-30 mm matrix.

Unit 33*g*

This unit is 1.2 m thick, red brown, densely welded and poorly sorted. Coarse layering occurs with 15-20 cm thick resistant layers are separated by less resistant 20 cm beds. The matrix is 2-20 mm and contains flattened vesicular bombs up to 50 cm long and 5 cm thick.

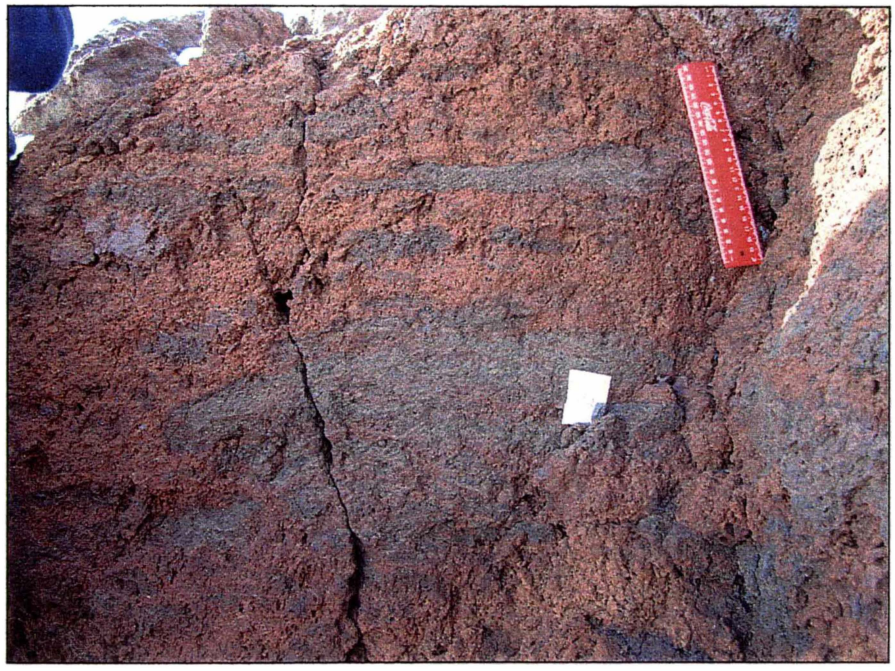

Fig.2.15: Unit 33*g* showing deformed and flattened bombs gray bombs in a red brown matrix (photo: R. Price).

Unit 33*h*

This unit is red, clast supported, partially welded and poorly sorted with a blocky surface appearance. It is supported by abundant blocks and vesicular grey brown bombs up to 15 cm. A bomb-free, ash and fine lapilli (1-5 mm) sized bed occurs 40 cm below the top of the unit.

Unit 33*i*

This partially welded red unit is 2 m thick and coarsely bedded. The matrix is 1-10 mm in the fine beds and 2-5 cm in the coarse beds. Vesicular bombs up to 70 cm and rare blocks up to 40 cm occur in both the fine and coarse beds. A discontinuous ash layer up to 15 cm thick in places occurs at the base of the unit. It contains laminations defined by grain size, alternating between 1-2 mm and <0.5 mm.

Fig.2.16: The fine laminated layer at the base of Unit 33*i* and the underlying blocky Unit 33*h* (photo R. Price)

Unit 33*j*

This partially welded unit is 4.5 m thick, is red in colour and is coarsely bedded. It contains four finer layers, each 40-100 cm thick and with an ash sized matrix (<1 mm). These are separated by coarse blocky clast supported layers containing 2-15 cm bombs. Occasional blocks up to 30 cm and vesicular bombs up to 40 cm occur in both the fine and coarse beds. Both blocks and bombs are pyroxene basanite, but containing less pyroxene than the lower units in this section.

Unit 33*k*

This unit is 1.5 m thick, red in colour, coarsely bedded, poorly sorted and non-welded, shown by its recessive nature. There is continuous range in clast size from 1-2 cm up to 50 cm. Most bombs have ragged spatter or fluidal textures.

Unit 33*l*

This is a 6 m thick, massive, densely welded red brown unit. The matrix has a grain size of 0.5-15 mm but due to the extent of welding the individual grains are barely identifiable. Grey brown vesicular basanitic bombs occur, up to 20 cm in size, some of them in very poorly defined bomb rich layers.

Unit 33*m*

The uppermost unit in this section is a 10 m thick, massive, fine grained, densely welded red brown unit. This unit dips towards the east and is unconformable with the lower NW dipping units. There unit thins towards the north, seen in Figure 2.14 as a decrease in thickness from left to right. Figure 2.17 shows the thick massive deposit forming a distinctive deposit at the top of this outcrop.

The lower 3 m of the unit is bedded with alternating fine and coarse beds. The finer beds are very well sorted and <4 mm in grain size while the coarser beds have a grain size of 2-3 cm. The upper part (~5 m) of the unit is made of very well sorted, very densely welded coarse ash and fine lapilli (1-5 mm), in parts welding is so intense that individual clasts are no longer visible. Bombs are very rare and small, up to only 10 cm in size. Figure 2.18 is a close up view of this welded

section. The pitting shows where small vesicular bombs have been weathered from the densely welded matrix.

Fig.2.17: Unit 33*m* forming a prominent bluff at the top of the outcrop.

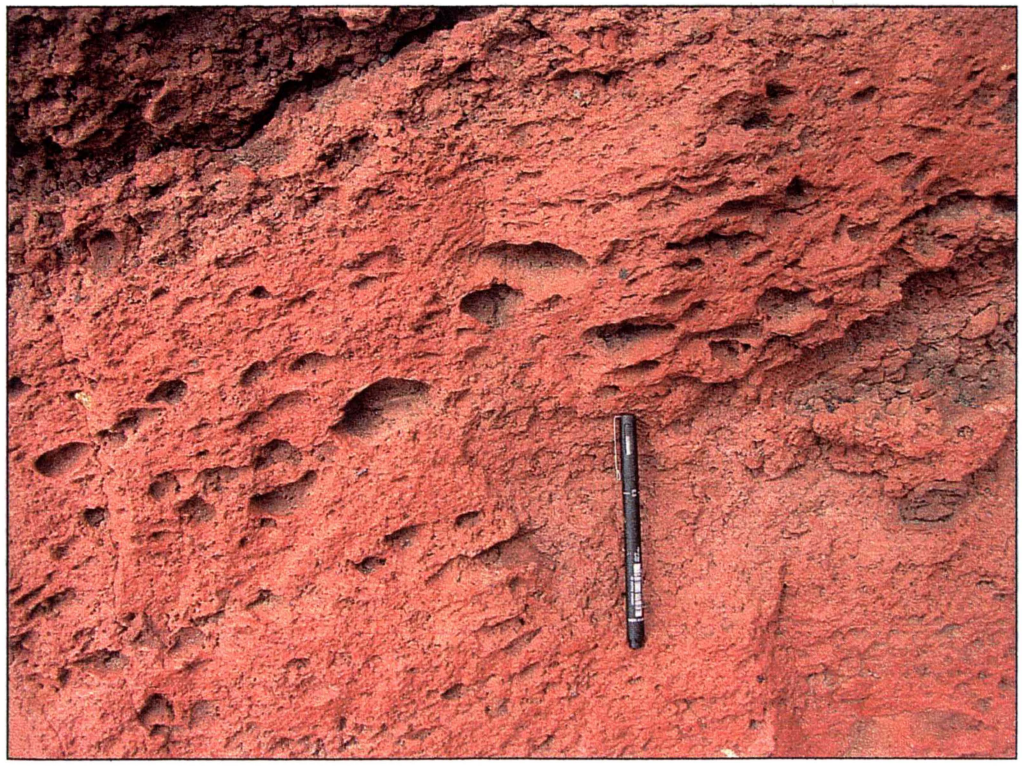

Fig.2.18: The densely welded upper part of unit 33*m* (photo: R. Price)

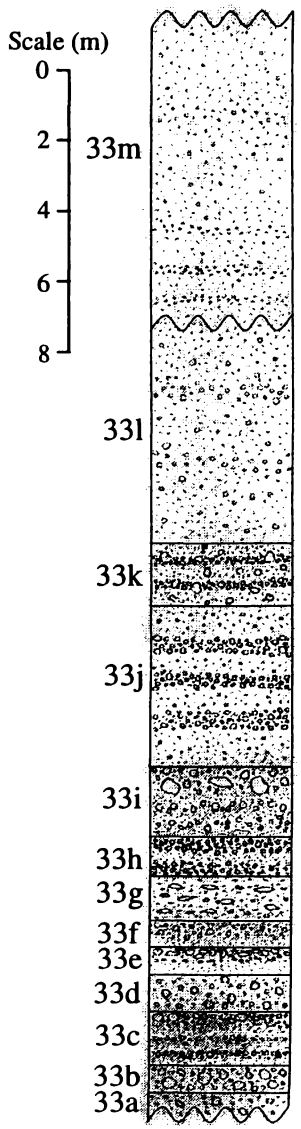

Unit	Colour	Welding	Matrix	Max. bomb size	Max. block size	Comment
33m	Red-brown	Extreme	1-50 mm	10 cm	-	Upper 5 m massive, Lower 3 m coarsely bedded
33l	Red-brown	Dense	0.5-15 mm	20 cm	-	Massive, occ. Bomb rich beds
33k	Red	Non-welded	Fine beds: <20 mm, Coarse beds: 20-80 mm clast supported	40 cm	40 cm	Coarse bedding
33j	Red	Partial	Fine beds: <10 mm Coarse beds: 10-150 mm clast supported	40 cm	40 cm	Coarse bedding
33i	Red	Partial	20-50 mm	70 cm	-	Coarsely bedded, V. fine laminated base
33h	Red	Dense	Clast supported <150 mm	15 cm, v. deformed	15 cm	Fine (1-5 mm) basal layer 10 cm thick
33g	Red-brown	Dense	2-20 mm	50 cm	30 cm	Poor sorting, Coarse bedding
33f	Pale red-brown	Partial-dense	2-30 mm	30 cm	30 cm	Poor sorting, Fine (0.5-2 mm) basal bed 5 cm thick
33e	Red-brown	Partial - dense	Upper: 1-5 mm, Base: 1-2 mm	30 cm	-	Reversely graded
33d	Red-brown	Dense	5-30 mm	40 cm	-	V. poor sorting
33c	Orange/ buff	Partial - dense	Upper: 5-50 mm, Base: <3 mm	50 cm	-	3x reversely graded subunits
33b	Red-grey-brown	Dense	10-30 mm	50 cm	-	V. poor sorting Granite xenoliths < 50 mm
33a	Red-brown	Partial - dense	2-10 mm	20 cm	-	Poor sorting

Fig. 2.18a: Scoria Cone 1 – descriptive stratigraphic column at Location 33.

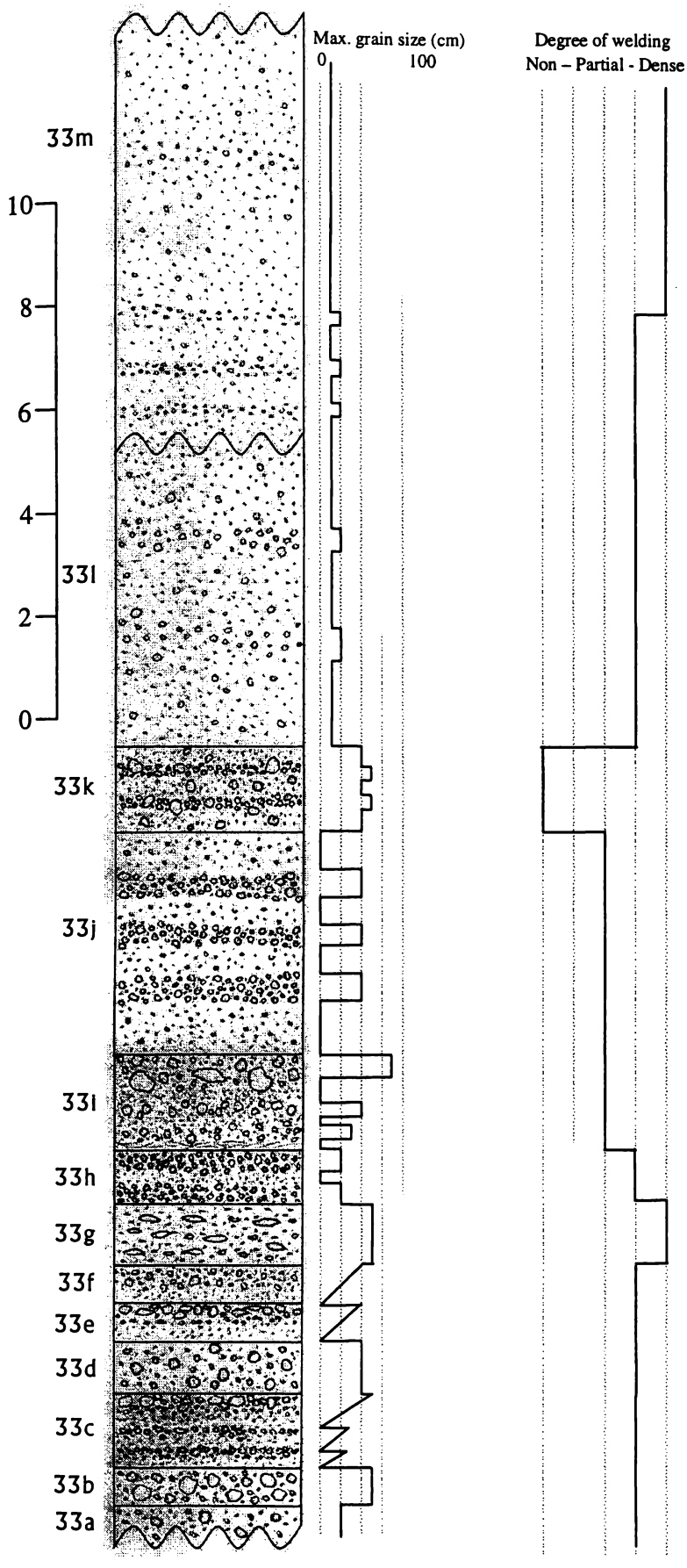

Fig. 2.18b: Scoria Cone 1 – stratigraphic column at Location 33.

2.2.3 STRATIGRAPHIC COLUMN AT LOCATION 37

This stratigraphic column describes a section approximately 40 m thick on the southern side of Scoria Cone 1 and summarised in figure 2.22. Twelve units (37*a-l*) were identified on the basis of colour, grain size, sorting, degree of welding and grading. Typical units in this stratigraphic column are red brown, coarse grained, bomb rich, partially welded and crudely bedded.

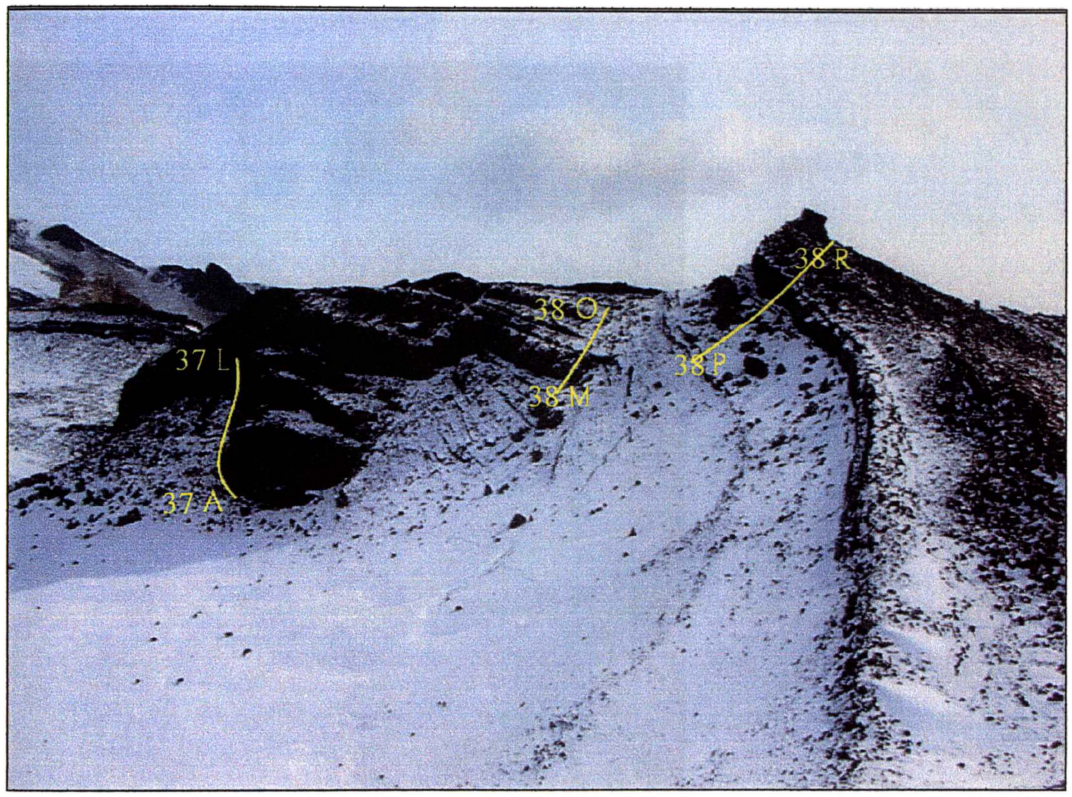

Fig.2.19: Photograph of the sequences described in stratigraphic columns 37 (units 37*a-l*) and 38 (units 38*m-r*) (photo: R. Price)

Unit 37*a*

This is the lowest unit in this sequence, it is an orange brown, partially welded pyroclastic deposit over 2.5 m thick. The basal contact is covered by snow and moraine. The matrix is fine lapilli (2-20 mm) and contains bombs of 5-30 cm. These clasts are both vesicular bombs and rare dense blocks, both composed of

pyroxene and olivine rich basanite. Some of the bombs are deformed to give the outcrop a streaky appearance. Rare granite inclusions are found.

Unit 37*b*

Overlying this is a 20 cm thick, pale grey, unit of agglutinated pyroclastic fragments. In parts the clasts are completely welded and deformed to give a streaky appearance and in others it has a rubbly surface and some clast outlines can still be seen. Small crustal xenoliths are common.

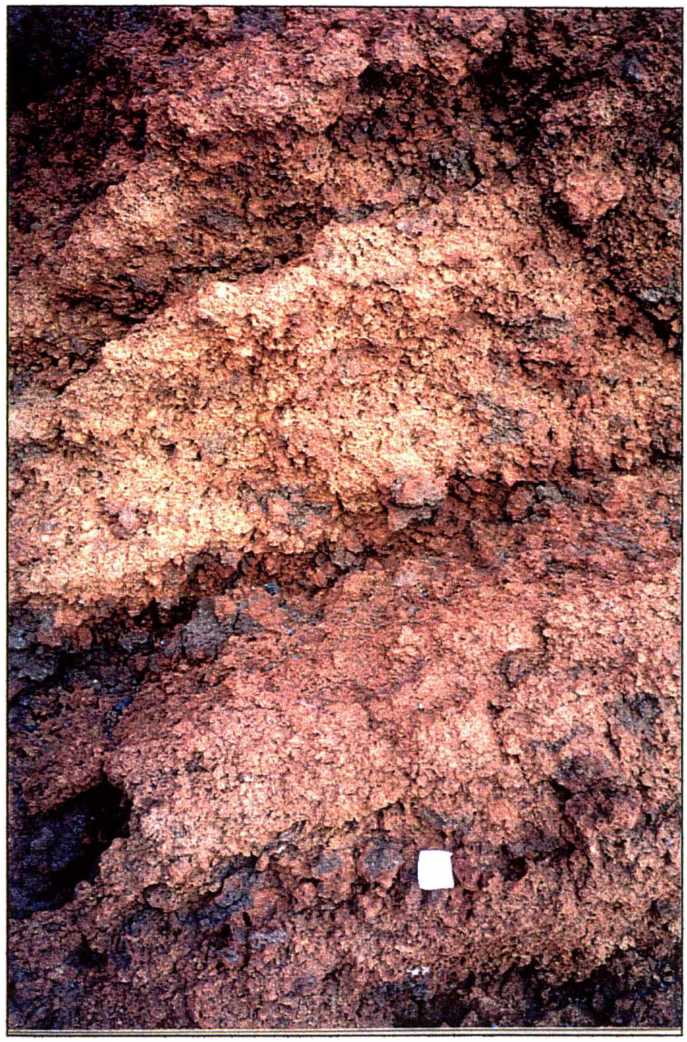

Fig.2.20: A typical deposit of stratigraphic column 37 (Unit 37*d*?). Coarsely bedded, partially welded pyroclastics with occasional beds of non-flattened bombs.

Unit 37*c*

This is a coarse grained, partially-densely welded, porous, bomb rich pyroclastic unit 2.8 m thick. It contains abundant grey basaltic bombs up to 15 cm in a red brown matrix of coarse ash and fine lapilli (1-10 mm). Many of the bombs are highly flattened to give the outcrop a streaky grey and red appearance.

Unit 37*d*

This is a coarse, partially-densely welded, crudely bedded pyroclastic unit 3.2 m thick. The bedding is defined by coarser medium lapilli (2-10 cm) and fine-medium lapilli (2-10 mm) layers. The finer beds are ~10 cm thick and are a yellow orange colour while the coarser beds are ~30 cm thick and a dark red brown colour. Bombs up to 40cm occur, none of these are flattened.

Unit 37*e*

This is a densely welded 3.2 m thick pyroclastic unit of coarse ash-medium lapilli containing deformed bombs up to 15 cm in size. These deformed bombs give the outcrop a streaky appearance. Fine grained layers of coarse ash-fine lapilli (1-10 mm) form discontinuous beds stretching for 2-3 m.

Unit 37*f*

This is a coarse, partially-densely welded, crudely bedded, 7.8 m thick pyroclastic unit. The lower 2.5 m of the unit contains bedding defined by continuous coarse (2-10 cm) and fine (2-10 mm) beds. Above this the unit grades up into a more welded and deformed part of the unit with a streaky appearance, similar to Units 37*c* and 37*e*.

Unit 37*g*

This is a red coloured, coarse, densely welded pyroclastic unit 4 m thick. It is clast supported and composed of ragged spatter fragments 1-10 cm in size. The outcrop is mainly massive but there are some more welded parts with a streaky appearance and occasional fine grained discontinuous layers.

Unit 37*h*

This is a massive, partially welded, bomb rich, red-brown pyroclastic unit 1.7 m thick. It has a matrix of fine to coarse lapilli (2-30 mm) containing abundant olivine rich basaltic bombs up to 50 cm. None of the bombs present show any flattening.

Unit 37*i*

This is a coarse, massive, red brown, partially welded pyroclastic unit 1.7 m thick. A well sorted matrix of fine-medium lapilli (1-4 cm) occasional larger bombs up to 20 cm in size. This unit is shown in Figure 2.21.

Unit 37*j*

This unit is 2.2 m thick, non-partially welded and crudely bedded. It is clast supported and contains ragged spatter fragments ranging in size from 0.5-10 cm and occasional larger bombs up to 30 cm in size. Bedding is defined by bomb rich layers roughly 10 cm thick. The outcrop is an orange brown colour but shows a change to a grey colour along the strike of the outcrop.

Unit 37*k*

This is a thin grey densely welded layer 40 cm thick. The matrix is very well sorted coarse ash-fine lapilli (2-20 mm). Small deformed bombs occur, the largest of these are 10-15 cm wide and 4 cm high and give the outcrop a streaky appearance. A pale blotchy surface alteration occurs on the surface of some clasts.

Unit 37*l*

This is the uppermost unit in the section, it is a sequence at least 10 m thick of dark red brown, crudely bedded, non-welded to partially welded pyroclastics. The bedding is defined by bomb rich layers, finer grained layers and more densely welded deformed streaky layers.

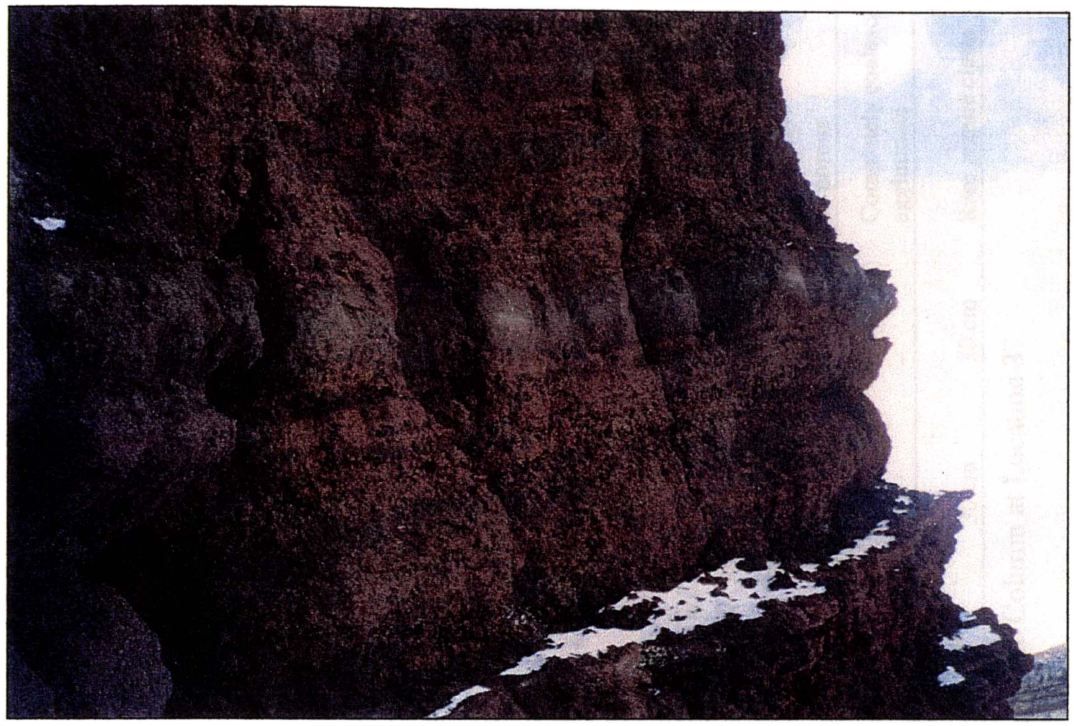

Fig. 2.21: Partially welded, coarsely bedded pyroclastics of unit 37*l*.

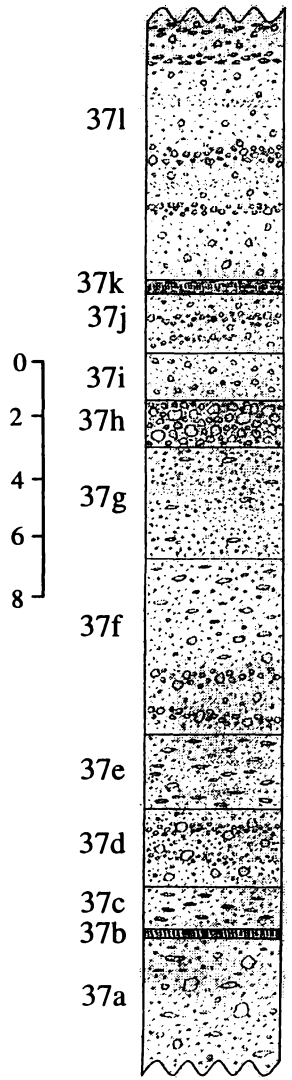

Unit	Colour	Welding	Matrix	Max. bomb size	Max. block size	Comment
37l	Orange-brown	Weak-partial	5-100 mm clast supported	30 cm	-	Bedding defined by; -bomb rich beds - -fine grained beds
37k	Grey	Dense	2-20 mm	15 cm, deformed	-	V. densely welded
37j	Orange-brown-grey	Partial	5-100 mm clast supported	30 cm	-	Bedding defined by bomb rich beds
37i	Red-brown	Partial	10-40 mm	20 cm	-	Well sorted, massive
37h	Red-brown	Partial	2-30 mm	50 cm	-	Massive
37g	Red-brown	Dense	10-100 mm clast supported	50 cm	30 cm	Massive, occ fine grained beds
37f	Red-brown	Partial - dense	Coarse: 20-100 mm, Fine: 2-10 mm	Some larger clasts deformed	-	Crude bedding defined by grain size
37e	Red-brown	Dense	1-10 mm	15 cm, deformed	-	Discontinuous fine grained (1-10 mm) beds
37d	Orange-red-brown	Partial - dense	Coarse: 20-100 mm, Fine: 2-10 mm	40 cm	-	Bedding defined by grain size
37c	Red-brown	Dense	1-10 mm	15 cm, deformed	-	V. porous
37b	Grey	Extreme		-	-	Completely coalesced agglutinate
37a	Orange-brown	Partial	2-20 mm	30 cm	30 cm	Rare granite clasts

Fig.2.22a: Scoria Cone 1 – Stratigraphic Column at Location 37

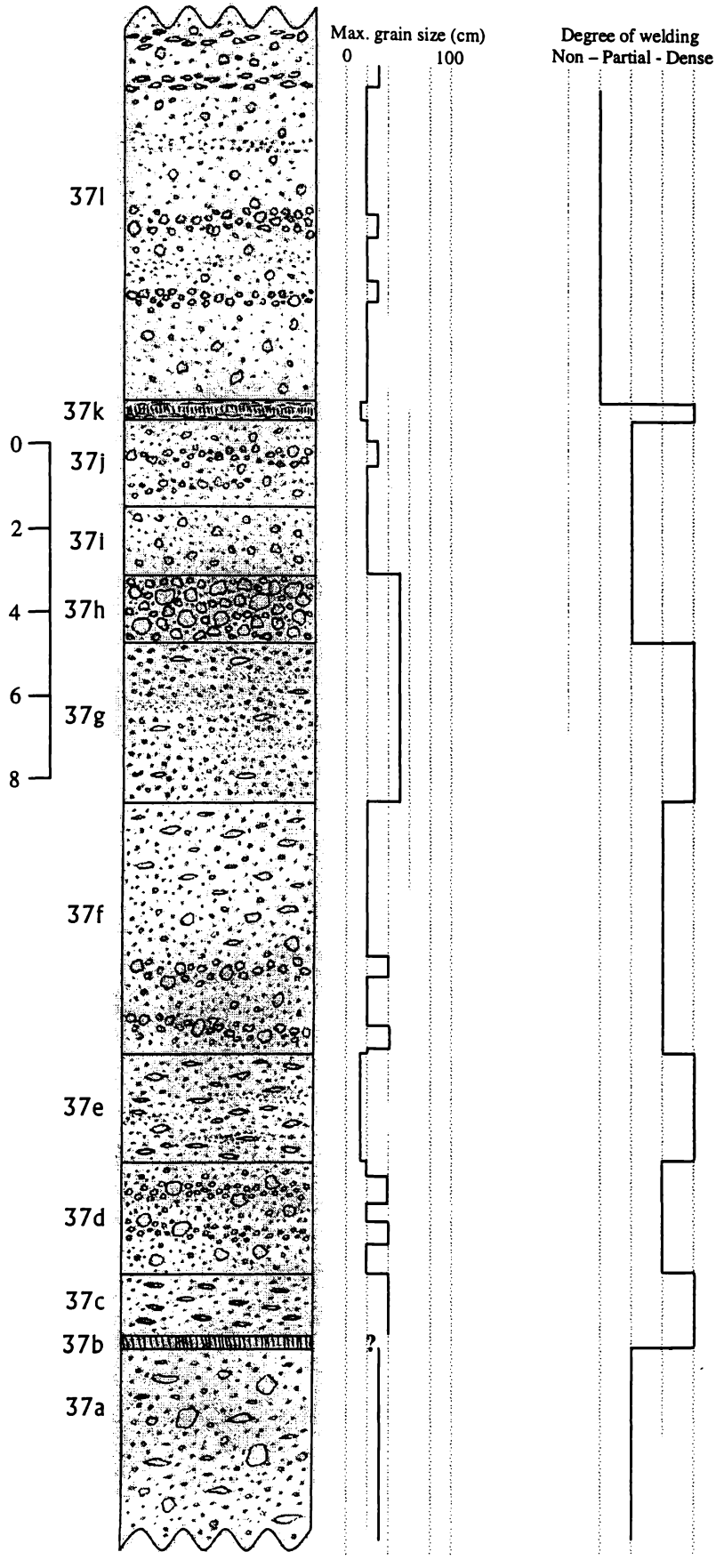

Fig.2.22b: Scoria Cone 1 – Stratigraphic Column at Location 37

2.2.4 SCORIA CONE 1 – STRATIGRAPHIC COLUMN AT LOCATION 38

This column describes a series of pyroclastic units with a total thickness of approximately 30 m on the southern side of Scoria Cone 1 and summarised in Figure 2.26. Nine units (38*m-u*) were identified on the basis of colour, grain size, sorting, degree of welding and grading. There is approximately 10 m of section not logged between the top of unit 37*l* and the base of this section. Units 38*m-r* can be seen in Figure 2.19.

Unit 38*m*

This unit is the lowest unit of the section beginning at Location 38. It is a 3.5 m thick grey densely welded deposit. In the most welded part of the unit the individual grains are not visible and above and below this there is a gradual transition into a streaky deposit of highly deformed clasts.

Unit 38*n*

Overlying this unit is a dark grey, coarsely bedded, moderately welded unit 2.2m thick. The bedding is defined by alternations of 5-10 cm thick ash layers (1-2 mm) and 40 cm thick fine-medium lapilli layers (2-50 mm). Bombs are rare and slightly flattened.

Unit 38*o*

This is a 90 cm thick, moderately welded pyroclastic unit. The matrix is yellow brown coarse ash-fine lapilli (1-10 mm). Only a few grains in the matrix have fluidal textured surfaces. Many vesicular grey basaltic bombs ranging in size from 1-10 cm occur throughout the unit.

Fig. 2.23: Yellow brown unit 38*p*.

Unit 38*p*

There is 2-3 m of snow cover separating this from unit 37*o*, it may be that the units identified as 38*o* and 38*p* are actually the upper and lower parts of the same yellow brown grey unit. This is a dark yellow grey clast supported unit composed of scoria ranging in size from fine lapilli to small bombs (2-100 mm). Larger bombs up to 20 cm of grey vesicular basalt are rare. This unit is seen in Figure 2.23

Unit 38*q*

This massive, moderately-densely welded grey brown unit forms a distinctive bluff 8 m tall (Fig. 2.24). The matrix is composed of coarse ash-fine lapilli (1-10 mm) and contains abundant bombs and blocks up to 60 cm in size.

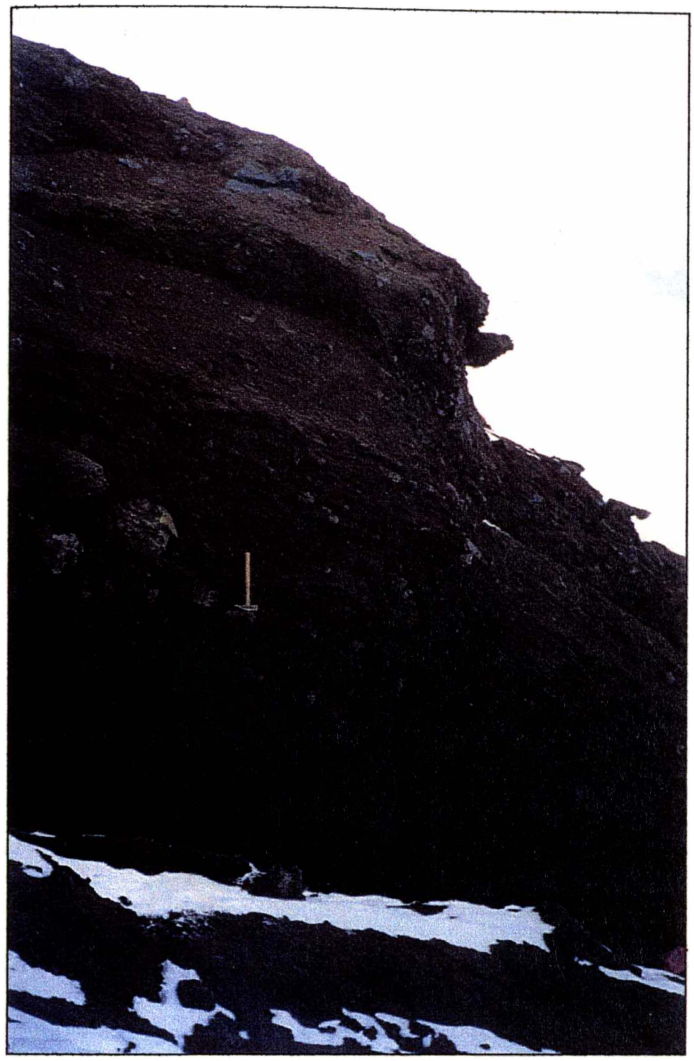

Fig.2.24: The thick, bomb and block rich unit 38*q*.

Unit 38*r*

This is a 6 m thick red brown densely welded pyroclastic deposit with some coarse bedding. The majority of the clasts have fluidal textures and range from coarse ash-medium lapilli (1-50 mm). The bedding is distinguished by slightly coarser and finer beds, some very bomb rich with bombs up to 15 cm in size.

Unit 38*s*

This is a very densely welded red brown spatter deposit forming a darker band 5 m thick between the red units 38*r* and 38*t*. Clast outlines are not easily

identifiable. Where they can be seen the fragments are coarse ash sized (1-2 mm). Rare larger bombs and blocks occur.

Unit 38*t*

This is a very highly welded red spatter deposit 1.8 m thick. It contains bombs up to 15 cm in a coarse ash-medium lapilli matrix (1-40 mm), many fragments show obvious fluidal texturing.

Unit 38*u*

This unit is a 1 m thick, coarse, dark brown deposit of densely welded fragments, they majority with fluidal textures. Slight grading in this unit, near the base it has a grain size of 1-10 cm and this decreases to 2-30 mm near the top. Occasional blocks occur up to 40 cm in size, one of these is shown in Figure 2.25.

Fig.2.25: Unit 38*u* showing a large basanite block in a fine grained spatter matrix.

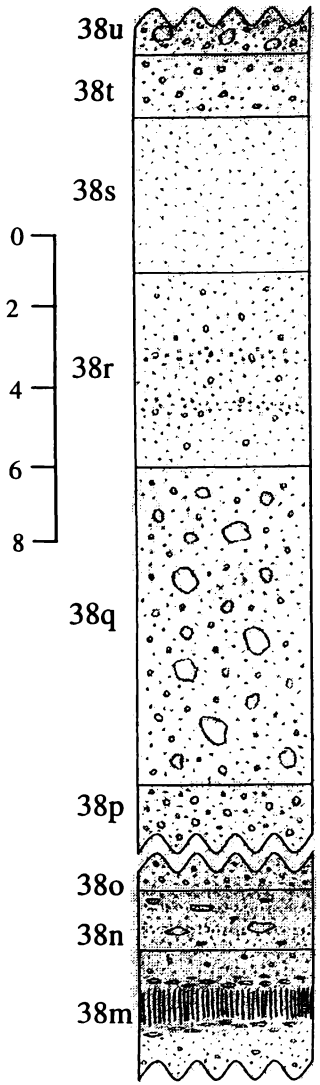

Unit	Colour	Welding	Matrix	Max. bomb size	Max. block size	Comment
38u	Dark brown	Dense	Upper: 2-30 mm Lower: 10-100 mm	-	40 cm	
38t	Red	Dense	1-40 mm	15 cm	-	
38s	Dark brown	Dense-extreme	1-2 mm	15 cm	-	
38r	Red-brown	Dense	1-50 mm	15 cm	-	Bedding defined by grain size
38q	Red-brown	Partial-dense	1-10 mm	60 cm	60 cm	
38p	Yellow-brown	Partial	2-100 mm, clast supported	20 cm	-	Possibly 38o, 38p are part of the same unit
38o	Yellow-brown	Partial	1-10 m	10 cm	-	
38n	Dark grey	Partial	Coarse: 2-50 mm Fine: 1-2 mm	-	-	Bedding defined by grain size
38m	Grey	Dense-extreme	Unknown d.t. amount of welding	-	-	Completely coalesced agglutinate bed

Fig. 2.26a: Scoria Cone 1 – Stratigraphic Column at Location 38

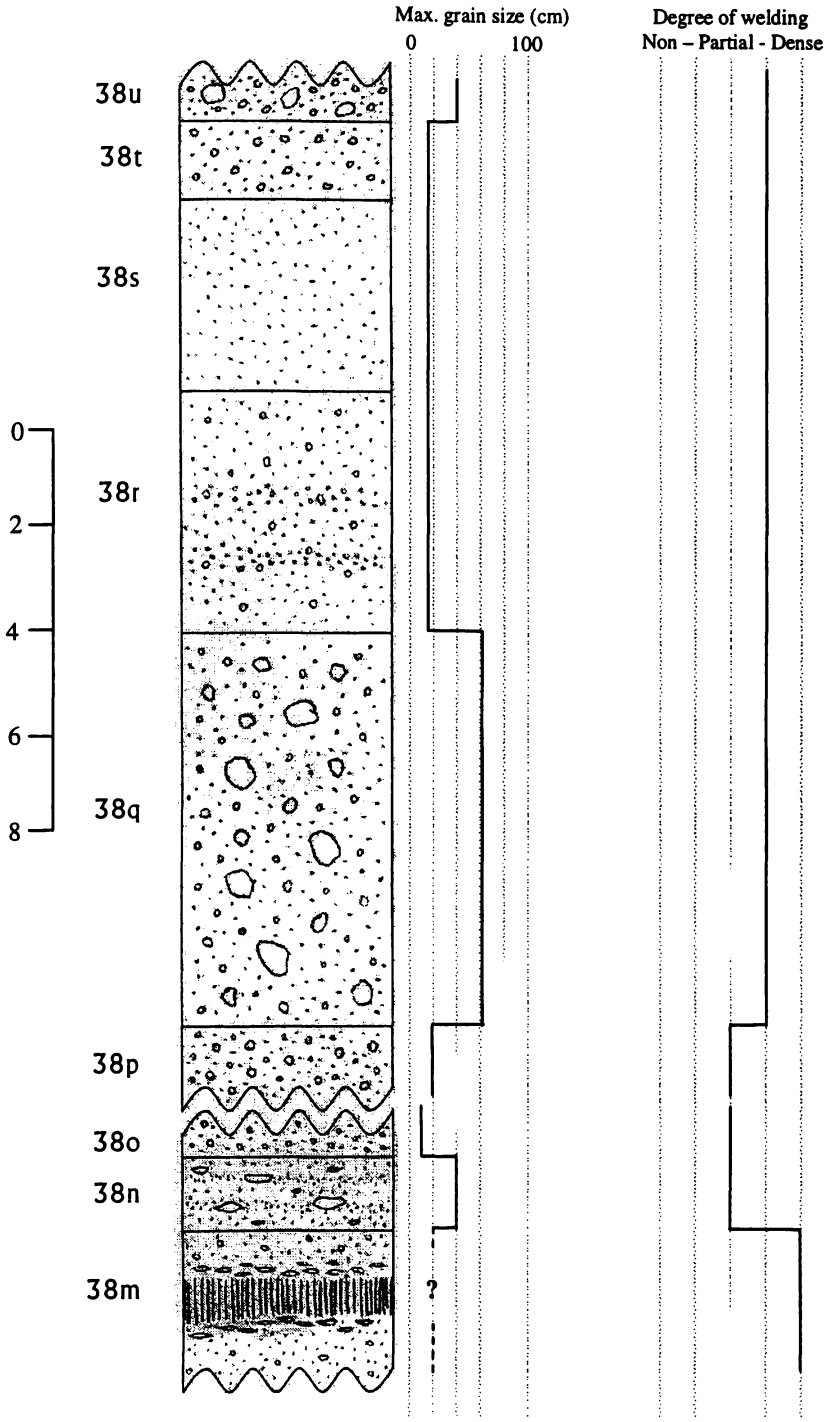

Fig. 2.26b: Scoria Cone 1 – Stratigraphic Column at Location 38

2.2.5 STRATIGRAPHIC COLUMN AT LOCATION 58

This column describes a series of pyroclastic units with a total thickness of approximately 40 m at the southern end of Scoria Cone 1. Eleven units (58*a-k*) were identified on the basis of colour, grain size, sorting, degree of welding and grading.

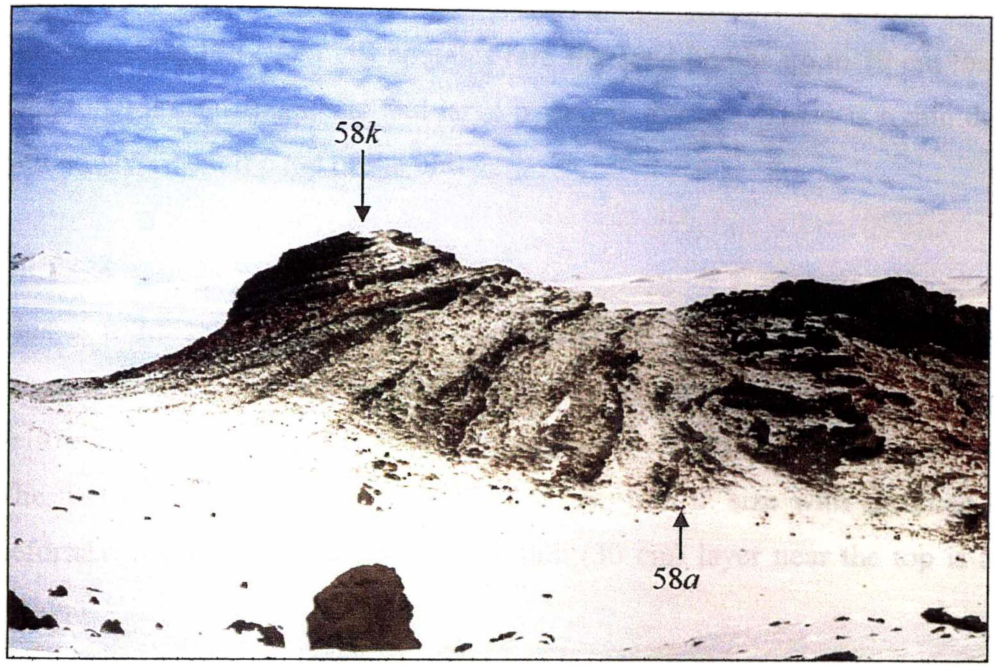

Fig.2.27: Sequence described in stratigraphic column 58.

Unit 58a

This is the lowest unit exposed in this sequence. It is a 1.7 m thick, dark brown, coarse pyroclastic unit intruded by a lensoidal dike of olivine rich basanite up to 2 m thick. The pyroclastics have a coarse ash-medium lapilli (1-10 mm) base and a coarser 3-100 mm centre containing vesicular bombs up to 30 cm long. The intrusion of the dike has fused and baked the contact with the pyroclastics, so that individual grains can no longer be identified along this contact.

Unit 58b

This unit is a 4.4 m thick dark red brown pyroclastic unit. Flattened grey vesicular bombs, with abundant crustal fragments up to 3 cm and pyroxene crystals up to 2 cm occur in a coarse ash-fine lapilli matrix. The upper 60-70 cm of the unit is densely welded.

Unit 58c

This is a 3.3 m thick yellow brown, slightly purple pyroclastic unit. A matrix of fine-coarse lapilli (2-50 mm) contains rare flattened bombs up to 20 cm long and occasional crustal fragments and large pyroxene crystals. There is a thin densely welded layer near the top of the unit

Unit 58d

This is a 3.8 m thick pyroclastic unit similar to unit 58*c* but distinguished by larger and more common bombs. The base and center of the unit is a blotchy yellow brown colour, while in the upper part it changes to a red-brown colour. The unit is clast supported by fragments 1-80 mm in size with common larger deformed bombs up to 35 cm long. A thin (30 cm) layer near the top is highly welded.

Unit 58e

This unit is 6.8 m thick pyroclastic deposit forming a red brown bluff. The matrix is composed of coarse ash-medium lapilli (1-30 mm), many with ragged spatter textures, these contain abundant blotchy grey basaltic bombs up to 40 cm in size. There is a thick extremely welded olivine rich basanite bed near the top of the unit, with gradational change to deformed agglutinate above and below.

Unit 58f

This is a 2.5 m thick, bright red, highly welded spatter deposit. The unit is clast supported by ragged spatter fragments ranging in size from 2-100 mm, although it is difficult to identify individual grains due to the amount of welding. Weak layering is shown by streaky deformed clasts up to 15 cm in size.

Fig.2.28. Bright red spatter deposit unit 58*f*.

Unit 58g

This is a 3.7 m thick, red brown unit with a distinctive streaky grey fabric caused by deformed vesicular bombs. The unit is clast supported and has a grain size of 2-50 mm, most fragments have ragged spatter textures.

Unit 58h

This unit is 80 cm thick, red grey in colour and similar to the underlying Unit 58*g*. The unit has several resistant, densely welded layers alternating with erosive, non-partially welded layers each 15-20 cm thick.

Unit 58i

This is a bright red, 3 m thick spatter deposit very similar to unit 58*f*. The unit is clast supported and made of 2-100 mm clasts, most with fluidal or ragged spatter textures. Occasional basaltic blocks up to 30 cm in size occur.

Unit 58j

This is a 2 m thick, non-partially welded, recessive, grey brown spatter deposit, similar to unit 58g and 58h. Grain size is typically coarse ash-medium lapilli (1-40 mm) lapilli with ragged spatter clasts and rare deformed bombs up to 15 cm in size.

Unit 58k

This is the uppermost unit in the sequence and forms a red brown 5 m thick bluff capping the underlying units. The unit is composed of lapilli-fine bombs (2-100 mm) with a very streaky appearance and containing many crustal fragments. Several discontinuous highly welded grey layers 20 cm thick and several meters long appear in the center of the unit. The upper part of the unit is densely-extremely welded for a thickness of 1-1.5 m.

The upper units of columns 38 and 58 can be correlated. The thick bluff forming units 38*q* and 58*e* are equivalent, and the yellow brown units 38*o, p* are equivalent 58*c, d.* The units in column 58 display higher degrees of welding than their equivalents in column 38. Units 58*c, d, e* contain agglutinate beds but their equivalent units in column 38 do not. This may indicate that the deposits of column 58 deposits are closer to the vent than those in column 38. This is consistent with a vent positioned to the southwest of these deposits.

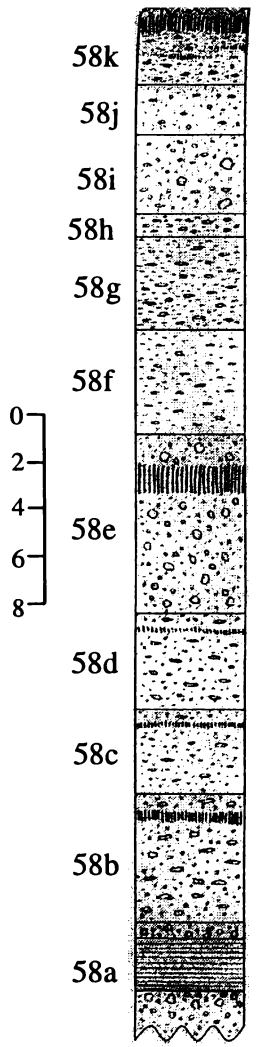

Unit	Colour	Welding	Matrix	Max. bomb size	Max. block size	Comment
58k	Grey-brown	Dense	3-100 mm, clast supported		-	Rare crustal fragments Thick agglutinate bed
58j	Grey-brown	Non-partial	2-50 mm	15 cm, deformed	-	
58i	Bright red	Dense	1-50 mm	10 cm	30 cm	
58h	Red-grey	Partial-dense	2-50 mm	10 cm, deformed	-	Bedding defined by alternating erosive/resistant beds
58g	Red-brown	Dense	2-50 mm	10 cm, deformed	-	
58f	Bright red	Dense	2-100 mm, clast supported	15 cm, deformed	-	
58e	Dark brown	Dense-extreme	2-100 mm, clast supported	40 cm	-	Thick agglutinate bed
58d	Yellow-brown	Dense	2-80 mm	30 cm, deformed	-	Thin agglutinate bed
58c	Yellow-brown	Dense-extreme	2-50 mm	20 cm	-	Occ. Px xtals and crustal frags Thin agglutinate bed
58b	Dark red-brown	Dense-extreme	2-30 mm	30 cm	-	Px. xtals <20 mm Crustal frags <30 mm Thin agglutinate bed
58a	Dark brown	Dense-extreme	2-100 mm clast supported Base: 1-10 mm	30 cm	-	Contains a basanitic dike

Fig.2.29a: Stratigraphic column at Location 58 of Scoria cone 1

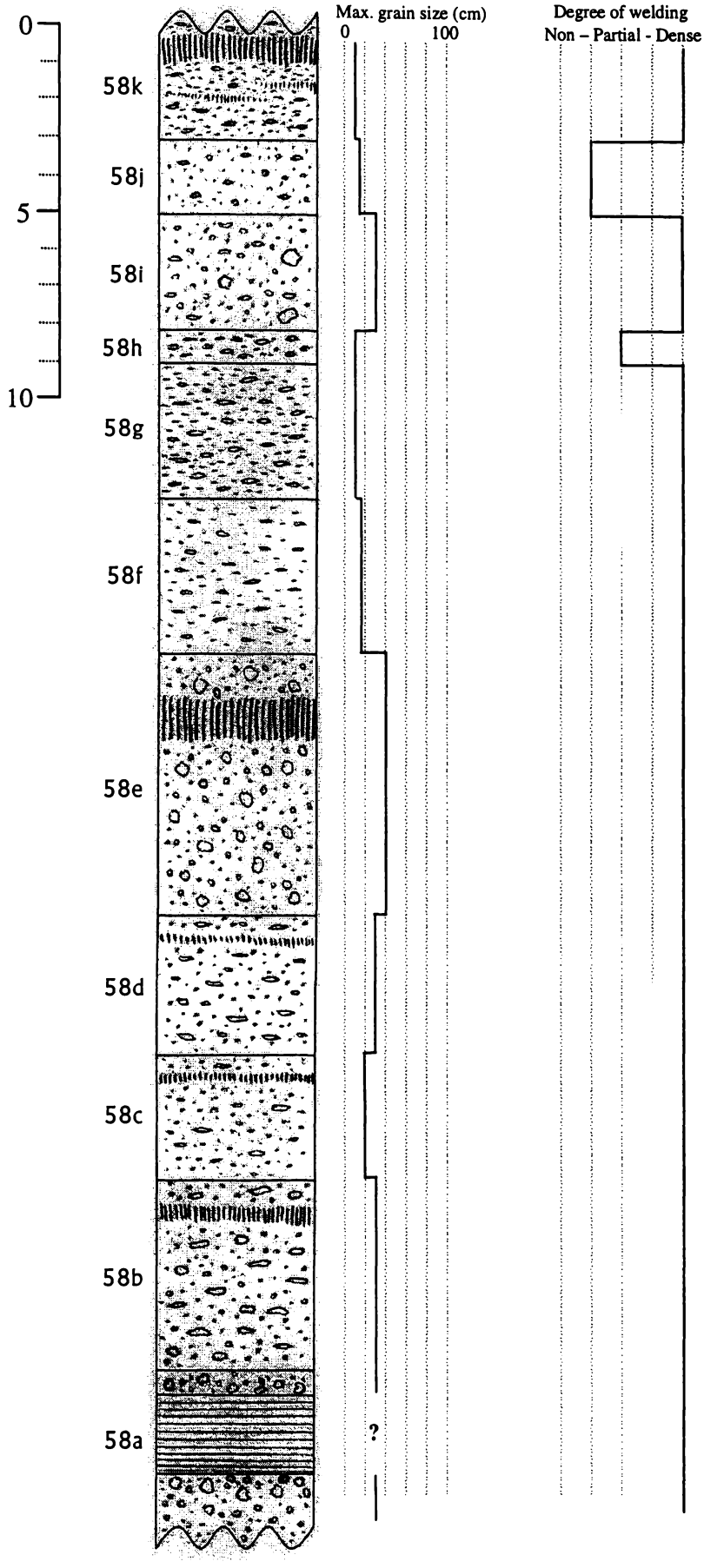

Fig.2.29b: Stratigraphic column at Location 58 of Scoria Cone 1

2.3 STRATIGRAPHY OF SCORIA CONE 2

2.3.1 STRATIGRAPHIC COLUMN AT LOCATION 59

Twelve pyroclastic units are identified and described, these are distinguished by; colour, grain size, sorting, degree of welding and grading. The stratigraphic column is summarised in Figure 2.31.

Unit 59*l*

This is the stratigraphically lowest unit in the exposed stratigraphic sequence of scoria cone 2. It is a densely welded deposit of red brown coarse pyroclastic fragments at least 3 m thick. It is a clast supported deposit of medium lapilli (1-4 cm). An 80 cm thick section near the top of the unit is extremely coalesced and agglutinated into olivine rich basanite.

Unit 59*k*

This is a grey brown, densely welded, massive, bomb rich pyroclastic unit 7 m thick. Rounded grey vesicular bombs up to 40 cm in size are common in a matrix of fine-medium lapilli (2-20 mm). At least two discontinuous bright red units similar to units 59*d, j* occur within the rest of the unit.

Unit 59*j*

This is a fine grained, bright red and densely welded unit 5 m thick. The matrix is made of fine lapilli (2-10 mm), but the amount of welding makes it difficult to distinguish individual grains. Rounded grey vesicular bombs up to 15 cm in size are common.

Unit 59*i*

This 1.1m thick unit has an extremely welded olivine rich basanite core 40 cm thick. Above and below the core the unit grades into streaky deformed clasts then to a rubbly grey deposit.

Unit 59*h*

This is a fine grained red-brown, partially welded pyroclastic unit 5 m thick. The matrix consists of well sorted, angular fine lapilli (3-10 mm). Grey vesicular bombs are scattered throughout the unit, some concentrated in bomb rich beds.

Unit 59*g*

This is a partially welded, coarsely bedded grey-brown unit 4 m thick. The ragged spatter textured clasts making up the unit are typically lapilli size (5-60 mm), although larger (up to 25 cm) vesicular grey bombs occur, some concentrated into bomb rich horizons.

Unit 59*f*

This is a prominent 1.2 m thick, bright red partially to highly welded unit. Vesicular grey bombs up to 10 cm are found in a matrix of fine-medium lapilli (2-30 mm).

Unit 59*e*

This unit is 12 m thick and composed of grey-brown pyroclastic debris. Vesicular grey bombs up to 40 cm in size are found in a matrix of medium-coarse lapilli (5-50 mm). Several bright red, 1-2 m thick, bands of densely welded spatter deposit similar to unit 59*d* occur through the unit.

Unit 59*d*

This is a 2 m thick, bright red deposit. The unit is clast supported and is made of fine lapilli to fine bomb sized ragged spatter fragments. The unit is coarsely bedded with partially welded resistant layers alternating with non-partially welded recessive layers.

Unit 59*c*

This is a 6 m thick recessive unit of dark red brown, crudely bedded, partially welded pyroclastics. It is a clast supported unit of medium lapilli-small bomb

sized ragged spatter fragments. Larger grey brown flattened vesicular bombs (40 x 10 cm maximum) also occur.

Unit 59*b*

This is a 5 m thick, grey brown, massive pyroclastic unit. The matrix is fine-medium lapilli (2-20 mm) and contains rare bombs up to 20 cm in size and also rare crustal fragments. In most parts the unit is partially-densely welded with a rubbly or streaky deformed texture, but a layer 60-100 cm thick is extremely welded to a dense lava with a gradational change to highly deformed, rubbly textured, densely welded deposit above and below.

Fig.2.30: Thin, completely coalesced agglutinate bed in unit 59*b*.

Unit 59*a*

This is the uppermost unit in the sequence, it is a 13 m thick, grey brown, pyroclastic unit with weak bedding. The unit is generally moderately welded, but has an extremely welded olivine rich basanite layer 1-1.5 m thick near the top. The matrix is coarse ash-medium lapilli (1-20 mm) and contains rare bombs up to 15 cm in size. Large (up to 1 m) blocks are rare in this unit.

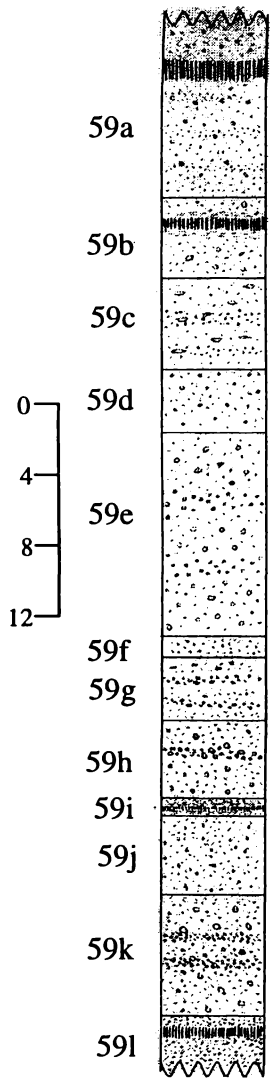

Unit	Colour	Welding	Matrix	Max. bomb size	Max. block size	Comment
59a	Grey-brown	Densely	1-20 mm	15 cm	100 cm	Thick (1.5 m) agglutinate bed
59b	Grey-brown	Densely	2-20 mm	20 cm	-	Thick (1 m) agglutinate bed
59c	Dark red-brown	Partial	3-100 mm	40 cm	-	Recessive
59d	Bright red	Non-densely	2-80 mm	15 cm	-	Bedding defined by resistant/recessive beds
59e	Grey-brown	Densely	5-50 mm	40 cm	-	Contains several thin bright red beds
59f	Bright red	Densely	2-30 mm	10 cm	-	
59g	Grey-brown	Partial	5-60 mm	25 cm	-	Occ. bomb rich beds
59h	Red-brown	Partial-dense	3-10 mm		-	Occ. bomb rich beds
59i	Grey	Dense-extreme			-	Thin agglutinate bed (40 cm)
59j	Bright red	Dense	2-10 mm	15 cm	-	
59k	Grey-brown	Dense	2-20 mm	40 cm	-	Contains several thin bright red beds
59l	Grey-brown	Dense	10-40 mm		-	Thick agglutinate bed (80 cm)

Fig.2.31a: Scoria Cone 2 – Stratigraphic Column at Location 59.

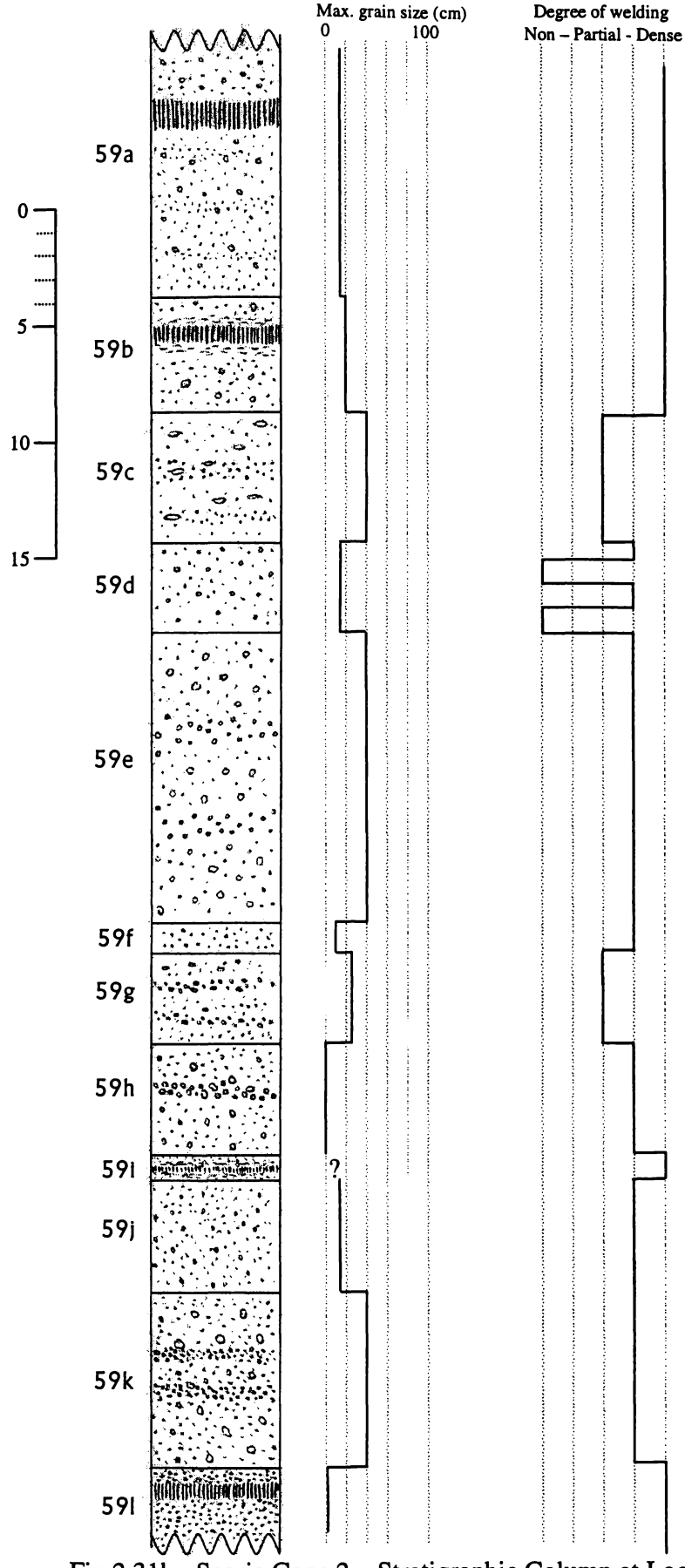

Fig.2.31b: Scoria Cone 2 – Stratigraphic Column at Location 59.

CHAPTER THREE PETROLOGY

3.0 ROCK TYPE CLASSIFICATION

The Mount Morning rocks have been classified using the total alkali-silica diagram of Le Bas *et al*, (1986) as a basanite-phonolite series (Fig.3.1). Basanitic compositions are the most common in the field area. There is a relatively continuous compositional range of basanites, from 42.6 to 49.1 SiO_2 wt%. Trachyte outcrops at only two locations (95, 96) in the field area.

This basanite-phonolite trend is similar to other basanite-phonolite lineages such as;

- Dunedin Volcanics *(Coombs and Wilkinson, 1969)*
- Tristan da Cunha *(Le Roex et al., 1990)*
- Erebus Province volcanics. e.g. Mount Erebus, Mount Discovery, Hut Point Peninsula, Brown Peninsula *(Kyle, 1976; Kyle et al., 1979; Kyle, 1981)*

Previous analyses from Riviera and Hurricane Ridges and Mason Spur (on the southeastern flank of Mount Morning) by Muncy *(1979)* and Wright-Grassham *(1987)*, are summarised in Kyle *(1990b)* and shown as shaded fields in Figure 3.1. All the data from this study plots within the range of previous analyses of the Quaternary geology from Mount Morning.

The rocks have been separated into five petrographic groups on the basis of their major and trace element chemistry. These groupings are consistent in most major and trace element variation diagrams (e.g. Fig.3.1), and rare earth element plots.

The symbols used in Fig. 3.1 are consistent in all geochemistry plots

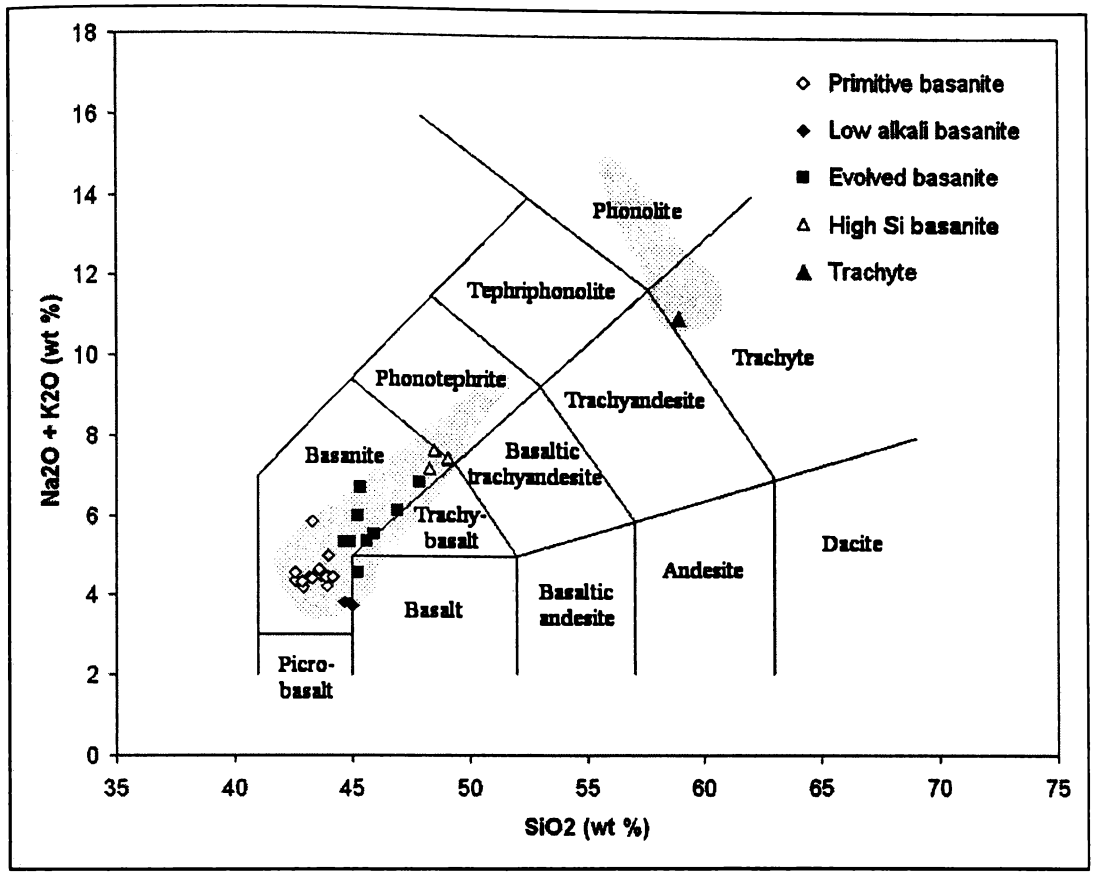

Fig.3.1: Total-alkali silica classification for Mount Morning rocks. Shaded fields are compositions of Quaternary Mount Morning and Mason Spur volcanic rocks from Kyle *(1990b)*. (Volatile free, all iron as FeO, field boundaries from Le Bas *et al., 1986*)

These five main petrographic groups observed are;

- Trachyte
- High Si basanite
- Evolved basanite
- Primitive basanite
- Low alkali basanite

The trachyte composition lies within the shaded field representing the Quaternary phonolites and trachytes analysed by Muncy *(1979)* and Wright-Grassham *(1987)*. It plots very close to the trachyte-trachyandesite field boundary.

The high silica basanite group forms a tight cluster in the high silica corner of the basanite field with silica contents of 48.3-49.1 weight percent and total alkali values of 7.2-7.7 weight percent.

The evolved basanite group has a large variation in both silica (44.7-47.9 wt%) and total alkali (4.6-6.9 wt%) contents. One member of this group is strictly classified as basalt and others plot very close to the basanite-trachybasalt boundary.

The primitive basanites form a tight group with little variation in silica (42.6-44.2 wt%) or total alkali (4.2-4.7 wt%) contents, although two samples form outliers to this main cluster with total alkali contents of 5.0 and 5.9 weight percent.

The low alkali basanites are all very similar in composition, forming a tight group with little variation in silica (44.7-45.0 wt%) or total alkali (3.7-3.8 wt%) content.

Fig.3.2: Geological map of field area on Riviera Ridge, Mount Morning, Antarctica.

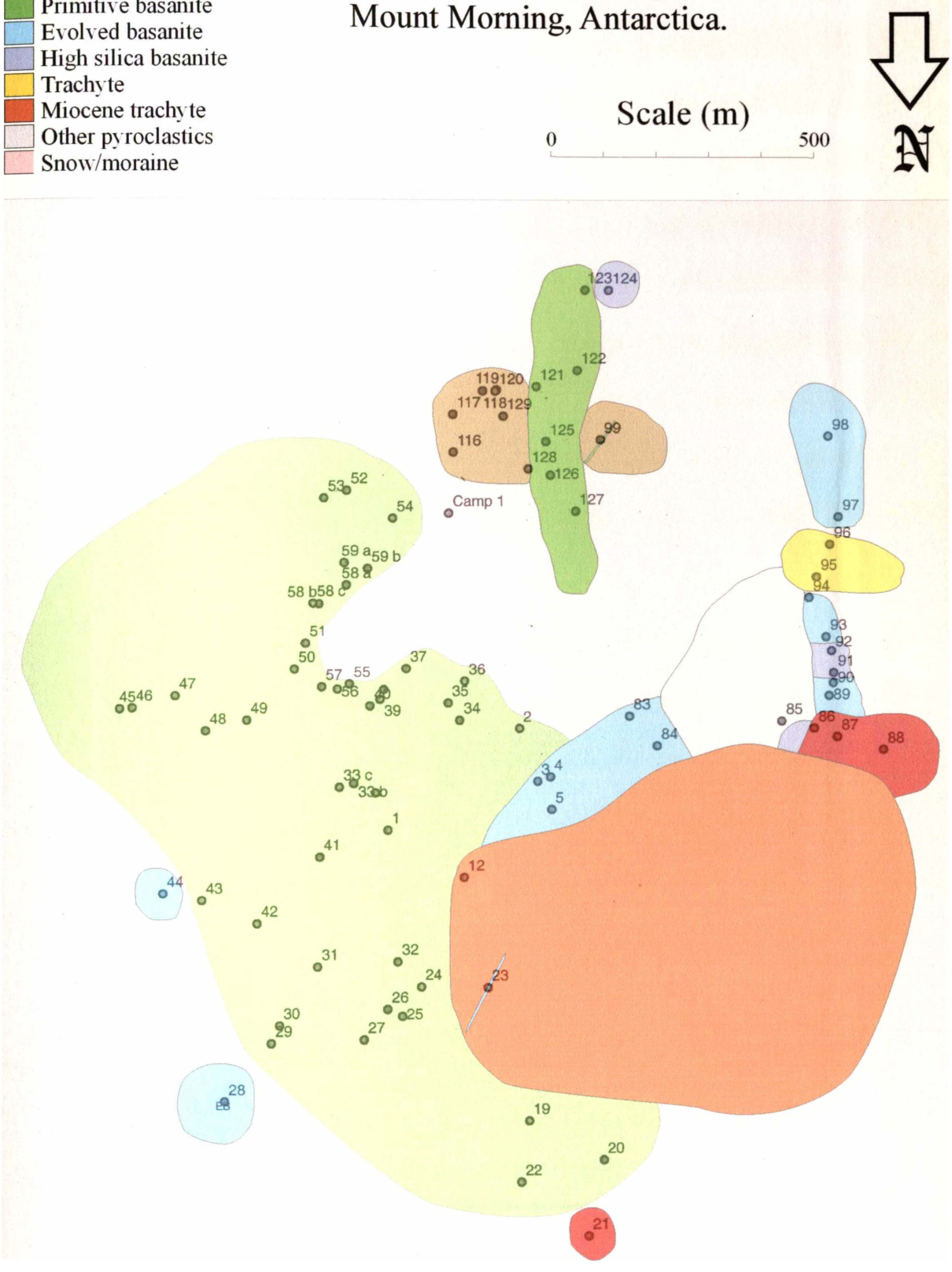

3.1 PETROGRAPHIC DESCRIPTIONS

3.1.1 TRACHYTE

Trachyte is found at two adjacent locations (Loc. 95 and 96) high on the ridge to the west of the field area (Fig.3.2). In hand specimen this rock appears pale, crystal rich and aphyric. In thin section the rock is seen to be fine grained (<0.5 mm) and dominated by feldspar (~75 %) and pale green pyroxenes (~15 %), with minor (<6 %) olivine, apatite, and opaque oxides (Fig.3.3).

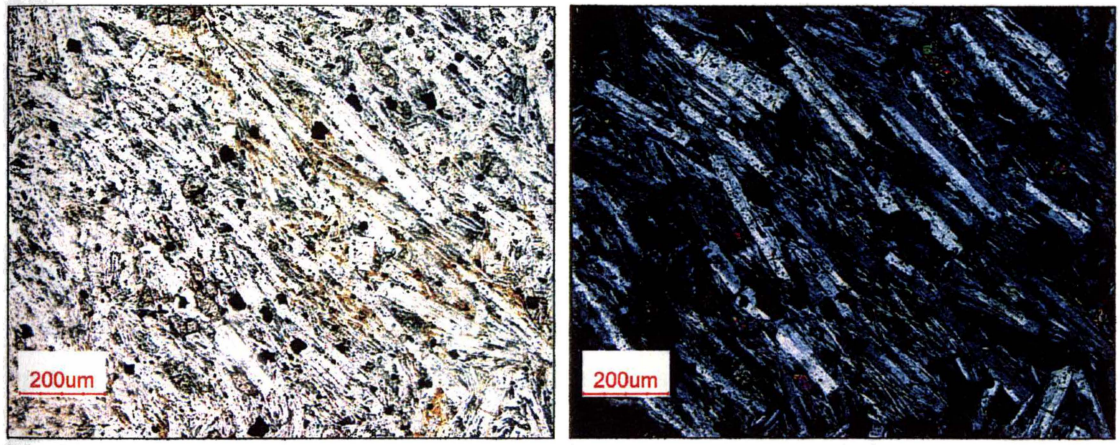

Fig.3.3: Typical thin section of a trachyte in *(a)* plane polarised light and *(b)* crossed polarised light.

Feldspar

The feldspars are oligoclase and anorthoclase, occurring as crystals 0.25-0.50 mm long. Some areas of a typical thin section show an alignment of crystals in a trachytic texture (Fig.3.3) while in others the crystals are arranged randomly. There are also some larger,

---

Mineral abundances were determined by point counts of several representative thin sections from each petrographic group (Appendix 2.2) Mineral chemistry was analysed by microprobe analysis of minerals from representative samples (Appendix 2.4).

blockier feldspar phenocrysts up to 1.5 mm and subhedral to anhedral. Many of these have resorbed, reaction rims characterised by inclusions of glass and opaque oxides, an example is shown in Figure 3.4.

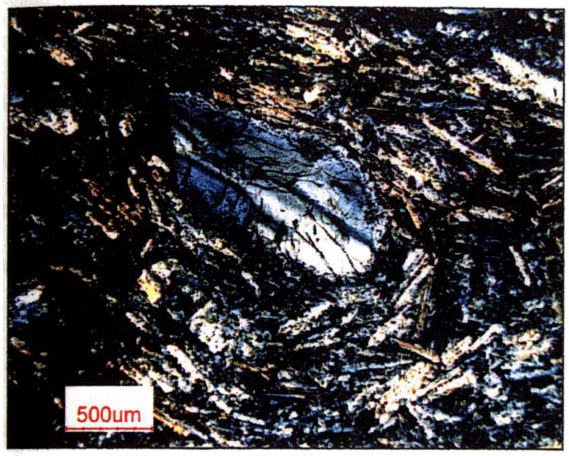

Fig.3.4: Large feldspar phenocryst in trachyte. (crossed polarised light)

Clinopyroxene

Pale green crystals of diopside and hedenbergite make up over 14 % of the rock. They are up to 0.3 mm in size and anhedral or subhedral in shape. Some display a pale yellow to pale green pleochroism.

Opaque oxides

Magnetite crystals make up 6 % of the rock. Individual crystals are up to 0.25 mm in size and either subhedral and equant or anhedral with irregular edges.

Olivine

Olivine crystals which make up 6 % of the rock are subhedral or anhedral and mostly equant and up to 1.5 mm in size. There is little alteration of olivine, only a thin orange brown alteration product occurring around the rim and in fractures of some crystals. Some of the larger crystals are heavily embayed with feldspar infilling fractures and embayments.

Apatite

Pale brown, rare (<1 %), fluid inclusion rich, apatites are euhedral and needle-like or prismatic and up to 0.2 mm in size.

3.1.2 BASANITE

Most of the basanite in the field area is similar in petrology. The basanites of the low alkali, primitive and evolved basanite groups are typically strongly porphyritic, containing large (up to 8 mm) phenocrysts of olivine and augite, with minor feldspar, amphibole and opaque oxides in a groundmass dominated by opaque oxides, augite and feldspar. Most basanites are poorly vesicular, although some samples have vesicularities of up to 20 %. The high silica basanites are less porphyritic, dominated by feldspar and often show a trachytic alignment of crystals.

3.1.2*a* HIGH SILICA BASANITE

High silica basanites were found at three locations in the field area (Loc. 86.A, 91, 124) and as bombs in the large breccia outcrop at location 118 (Fig.3.2). Four samples were examined and all are aphyric in hand specimen and either grey or rusty brown in colour depending on the amount of oxidation.

Typical basanites are porphyritic and dominated by feldspar (~60 %), and also contain large phenocrysts (up to 2.5 mm) of olivine and opaque oxides with minor pyroxene, apatite and calcite in a groundmass of feldspar and opaque oxides.

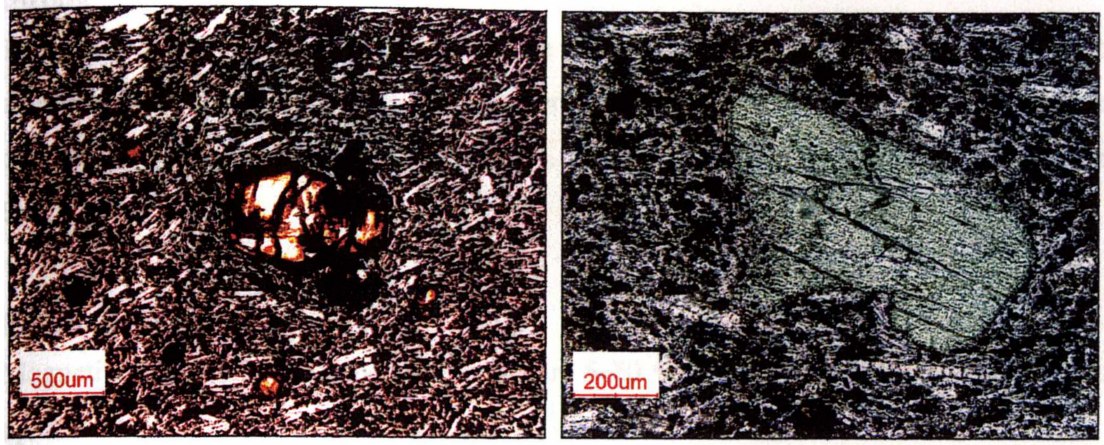

Fig.3.5: Altered olivine *(a)* and pale green pyroxene *(b)* phenocrysts in high silica basanite. (both in plane polarised light)

Feldspar

This makes up approximately 60 % of the rock and mostly occurs as subhedral crystals of plagioclase, ranging from andesine to labradorite in composition, up to 0.5 mm in size and showing either indistinct twinning or simple twinning. There are also rare larger phenocrysts up to 2.5 mm in size. All of these are anhedral and extensively resorbed (Fig.3.6).

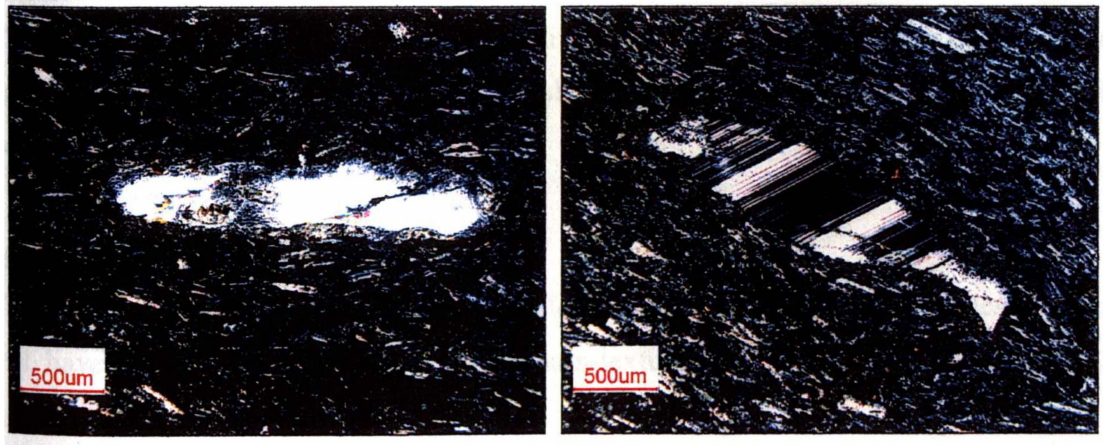

Fig.3.6: Large feldspar phenocrysts in high silica basanite. Note strong resorption of phenocrysts and flow alignment of groundmass plagioclase. (both in crossed polarised light)

Olivine

These pale yellow or colourless crystals are up to 1.5 mm in size and are both subhedral and anhedral in shape. Many show alteration around their rims and along fractures or are completely altered to blood red iddingsite. An altered olivine phenocryst is shown in Figure 3.5*a*.

Opaque oxides

Magnetite crystals are common and make up 5-20 % of the rock. Individual crystals are up to 0.75 mm and equant and subhedral in shape

Calcite

Calcite is identified by relief and high birefringence. It occurs in small patches and infilling cracks to form veins, some continuous for over 10 mm.

Pyroxene

Pale green pyroxene (probably diopside) phenocrysts are rare (<1 %), subhedral, and up to 0.75 mm in size (Fig.3.5*b*).

Apatite

Very pale brown, fluid inclusion rich, apatites are rare (<2 %), and up to 0.5 mm. They are euhedral in shape, either needle-like or showing a hexagonal cross-section through the crystal.

Groundmass

The groundmass consists of fine grained feldspar, augite and opaques. Samples 86.A and 91 have a well defined trachytic groundmass texture (e.g. Fig.3.6*b*), while sample 124 shows no alignment of crystals.

3.1.3*b* EVOLVED BASANITE

Evolved basanite occurs as outcrops high on the western ridge (89, 97, 98), and as dikes (23, 122) and as lava flows (3, 4.B). They are strongly porphyritic with large (up to 8 mm) subhedral and anhedral phenocrysts of olivine, augite, altered amphibole, opaque oxides and feldspar, in a feldspar dominated groundmass making up 35-40 % of the rock.

Rare peridotite and lower crustal micro-inclusions up to 3.5 mm in size are found in evolved basanites from some localities (e.g. Loc. 4.B, 97). Peridotite inclusions are granuloblastic textured with equant grains of olivine and pyroxene 0.3-1.2 mm in size (Fig.3.7). Small (<1 mm) granulite and granite crustal inclusions are rare and made up of equant, equigranular feldspar and pyroxene crystals 0.3 mm in size.

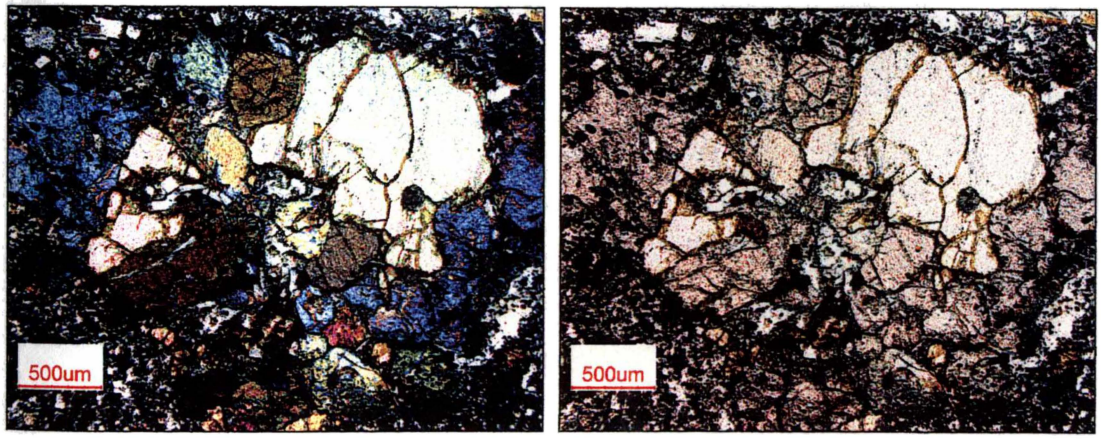

Fig.3.7: Peridotite micro-inclusion in evolved basanite in *(a)* plane polarized light and *(b)* crossed polarised light.

Many crystals contain inclusions of other minerals. These can be used to interpret the order of crystallisation. Apatite is found as inclusions in phenocrysts of olivine (Fig.3.9), pyroxene, feldspar and altered amphibole (Fig.3.11*b*). Feldspar occurs as inclusions in pyroxene (Fig 3.10*a*) and opaque oxide inclusions are found in pyroxene and feldspar

crystals. Therefore it is thought that olivine, pyroxene and amphibole were the first to crystallise, followed by feldspar, and then opaque oxides and apatite.

Feldspar

Plagioclase is abundant (18-43 %) and found as subhedral to anhedral phenocrysts up to 6 mm in size. Feldspars are typically labradorite and bytownite, although some rare alkali feldspar also occurs. Many plagioclase phenocrysts show extensive resorption rims (e.g. Fig.3.8*a*) and sieve textures characterized by inclusions of opaques and glass, some with further overgrowths around the original resorbed crystal.

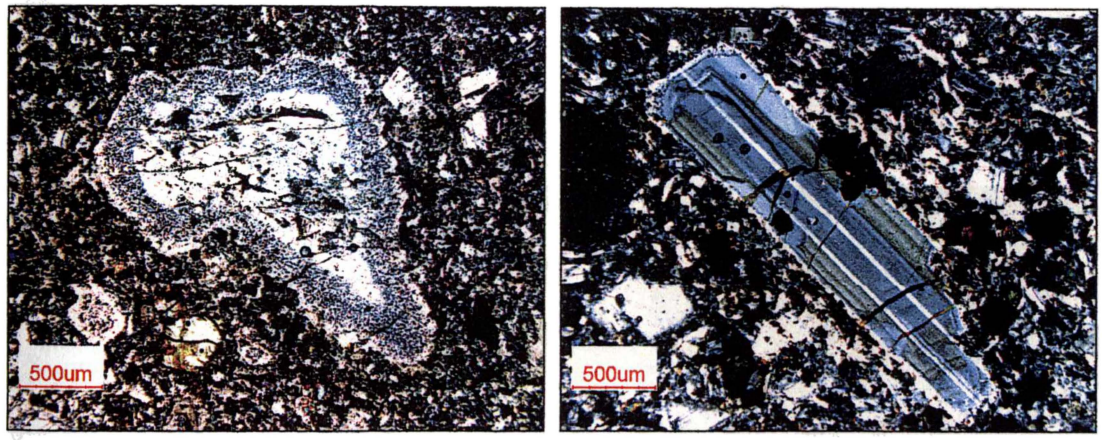

Fig.3.8: Feldspar phenocrysts in evolved basanite. (both in crossed polarised light)

Olivine

Large (up to 8 mm maximum), pale yellow or colourless olivine crystals are common (9-21 %), and mostly subhedral, although some are euhedral and anhedral. Generally they are relatively unaltered with only a fine rim of orange or brown alteration (Fig.3.9).

Fig.3.9: Partially altered olivine phenocryst containing an apatite inclusion in evolved basanite (plane polarised light).

Pyroxene

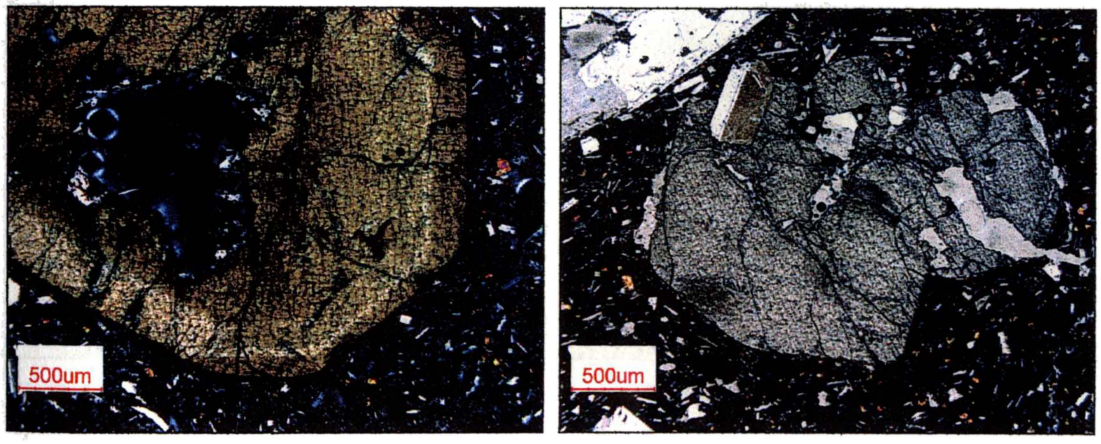

Fig.3.10: Diopside phenocrysts in evolved basanite. *(a)* zoned and *(b)* with an included feldspar crystal. (both in crossed polarised light).

These occur as large (up to 5 mm) pale purple brown and pale brown diopside phenocrysts with abundances of 3-22 %. Some show a pale yellow brown to pink/purplish brown pleochroism. Diopside occurs as euhedral, subhedral and rare anhedral crystals, some with resorbed reaction rims defined by inclusions of opaque oxides. Some crystals show zoning from a pale green core to purplish brown edges in

plane polarized light and many more show light/dark oscillatory zoning in crossed polarised light. A zoned diopside crystal is shown in Figure 3.10*a*. Yellow brown to pale green pleochroic pyroxenes are very rare.

Amphibole

These only occur in some of the basanites of this group, being most abundant (6 %) in samples from locations 89, 97 and 98. Amphiboles are completely pseudomorphed with no remnant core of the original crystal left (Fig. 3.11). The pseudomorphs are up to 2.5 mm in maximum dimension and made up of opaque oxides, olivine, pyroxene, feldspar and calcite with a dark opaque rich rim. Some contain inclusions of apatite (e.g. Fig. 3.11*b*).

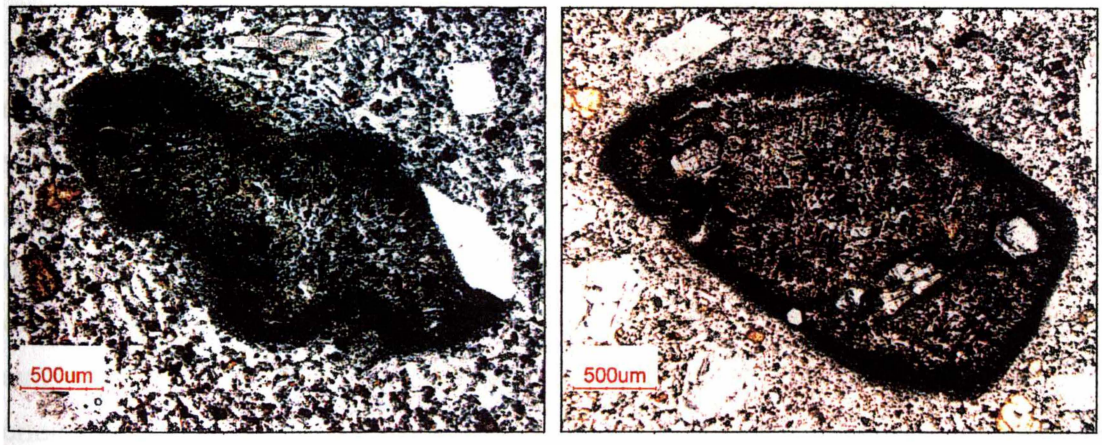

Fig.3.11: Altered amphiboles in evolved basanite. Note apatite inclusions in *(b)*. (both in plane polarised light)

Opaque oxides

These range in abundance from 4-20 %, and are both ilmenite and magnetite in composition. Individual crystals are up to 8 mm, and generally equant and subhedral.

Calcite

Calcite is rare (<1 %) and occurs as interstitial patches and as infills in fractures.

Apatite

Pale brown or grey apatites are rare (<2 %), and occur as small (up to 0.6 mm) euhedral crystals, either needle-like or showing a hexagonal cross-section through the crystal. Apatite is found as inclusions in olivine, altered amphibole and pyroxene.

Groundmass

The groundmass is fine grained (<0.1 mm), generally makes up 35-40 % of the rock, and is composed mainly of feldspar, with some opaque oxides and augite. In some samples (e.g. 23) the groundmass has a trachytic texture.

3.1.4*c* PRIMITIVE BASANITE AND LOW ALKALI BASANITE

The primitive basanite and low alkali basanite groups are indistinguishable mineralogically and so are therefore described together here. These groups include all the samples from scoria cone deposits. All samples examined are strongly porphyritic, with large (up to 5 mm) phenocrysts of olivine, clinopyroxene, feldspar and opaque oxides in a fine grained groundmass making up 55-80 % of the rock and dominated by opaque oxides (Fig. 3.11). All rocks of this group are slightly vesicular with vesicularities ranging from 1-12 %. Some samples show elongated vesicles with a consistent orientation (e.g. sample 28).

Large, abundant ultramafic and crustal xenoliths were found at location 74 in a primitive basanite. Small (<5 cm) crustal inclusions are common in some primitive basanite scoria cone deposits, for example units 37*a*, 58*b, c, k.* Micro-inclusions of these compositions are seen in thin sections of many samples of both primitive (e.g. 12.B, 45, 58.A.1, 74, 130) and low alkali basanite (e.g. 21). Aggregates of large (up to 2 mm) olivine crystals are common, some containing inclusions of chrome spinel (Fig.3.14). Peridotite micro-inclusions up to 4 mm in size, and composed of olivine (up to 2 mm), clinopyroxene (up

to 1.5 mm) and rare feldspar (<0.5 mm) are rare. Small (up to 1 mm), fine grained, pyroxenite micro-inclusions made up entirely of equigranular clinopyroxene grains up to 0.3 mm in size are rare.

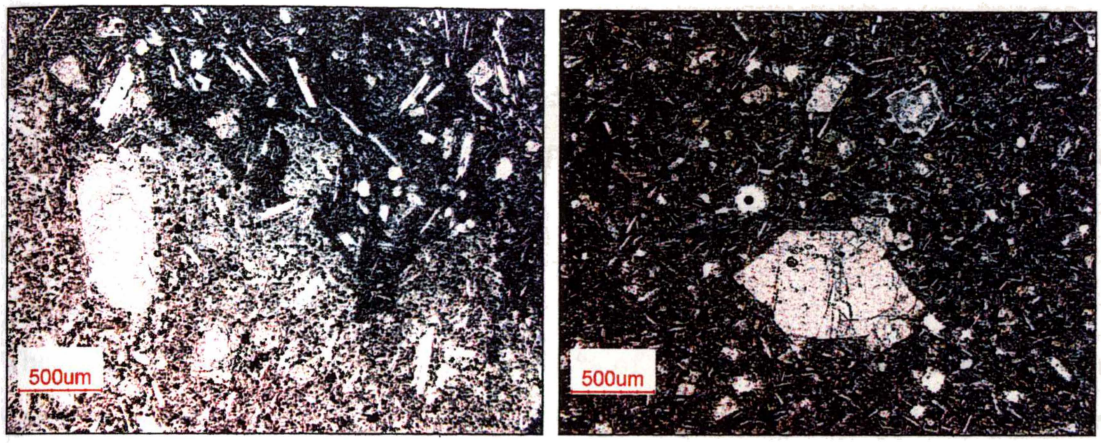

Fig.3.12: Typical basanites of the primitive and low alkali groups (both in plane polarised light). *(a)* shows a diffuse boundary between dark opaque rich groundmass and lighter more feldspar rich groundmass. *(b)* shows an olivine phenocryst in a dark opaque rich groundmass

Olivine

The majority of phenocrysts are olivine (32-75 % of phenocrysts), which are typically pale yellow or colourless, up to 5 mm in size and euhedral or subhedral in shape. Most crystals are very fresh but some show slight alteration around the rims and in fractures (Fig.3.11*b*).

Pyroxene

These are pale brown diopside, some with a slight purplish tinge, occurring as euhedral, subhedral and anhedral phenocrysts up to 4.5 mm in size and making up 0-8 % of the rock. Some crystals show zoning from a pale yellow to green pleochroic core to a purple brown outer rim and others show oscillatory zoning in cross polarized light.

Feldspars

Plagioclase occurs as labradorite and bytownite crystals up to 5 mm in size. They make up 4-15 % of the rock.

Opaque oxides

These are chrome spinels, ranging in abundance from 2-7 %. They are up to 0.5 mm in size and equant and subhedral. Some are present as inclusions in olivine and pyroxene (Fig. 3.14).

Groundmass

The groundmass typically makes up 50-80 % of the rock. It is dominated by opaque oxides and is commonly 'streaky' with lighter, feldspar rich and darker opaque rich parts as shown in Figure 3.11*a*. Also some fine grained diopside is present. Some samples have an extremely fine grained groundmass (e.g. Fig 3.13).

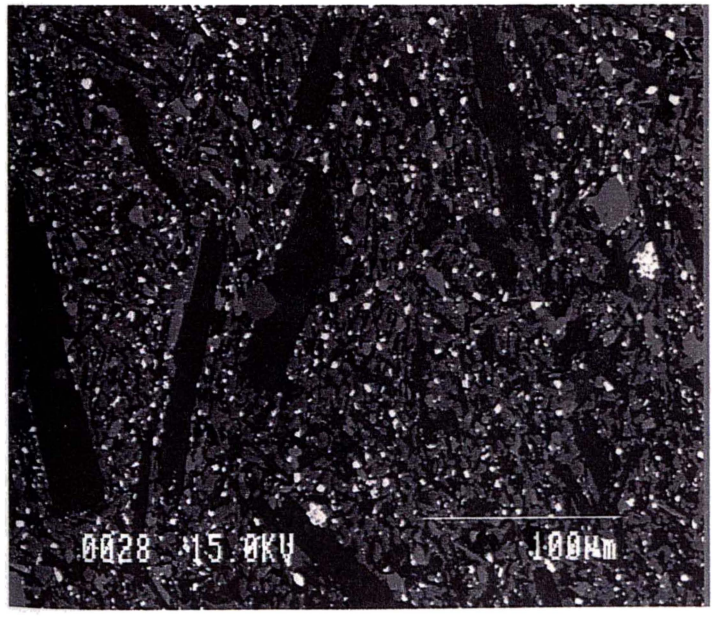

Fig.3.13: Back scattered electron microscope image of the groundmass of a primitive basanite (21, low alkali basanite group). The dark grey is feldspar, medium grey is diopside and occasional larger olivine, and the bright spots are small opaque grains.

3.2 MINERAL CHEMISTRY

Minerals from six samples representative of the rock types present in the field area were analysed by electron microprobe. The samples analysed were;

- Trachyte (sample 95)
- High silica basanite (sample 91)
- Evolved basanites (sample 3, 97)
- Primitive basanite (45)
- Low alkali basanite (21)

Phenocrysts of olivine, clinopyroxene, opaque oxides and feldspar were analysed for the major element oxides; SiO_2, Al_2O_3, Na_2O, K_2O, CaO, MgO, MnO, FeO* and TiO_2. Two opaque oxide crystals shown by energy-dispersive spectrometry to contain significant chromium were also analysed for chromium and nickel.

3.2.1 OLIVINE

Olivine compositions vary with increasing differentiation of the host rock, from magnesium rich (Fo_{76}) in the most primitive basanites and steadily increasing in iron content through the evolved and high silica basanites to iron rich (Fo_{18}) compositions in trachyte (Fig.3.15).

Olivine in the most primitive basanites (samples 21, 45) is generally magnesium rich ($Fo_{76} - Fo_{56}$). Some olivine phenocrysts in the primitive basanite show compositional zoning (Fig.3.14) with the crystal rim ($Fo_{69} - Fo_{68}$) containing less magnesium than the core ($Fo_{76} - Fo_{74}$). Occasional small opaque grains are found as inclusions of chrome spinel in olivine phenocrysts (Fig.3.14*b*). Chrome spinel inclusions in olivine

phenocrysts were also reported by Kyle *(1981)* in basanites of the DVDP drill holes and Hut Point Peninsula.

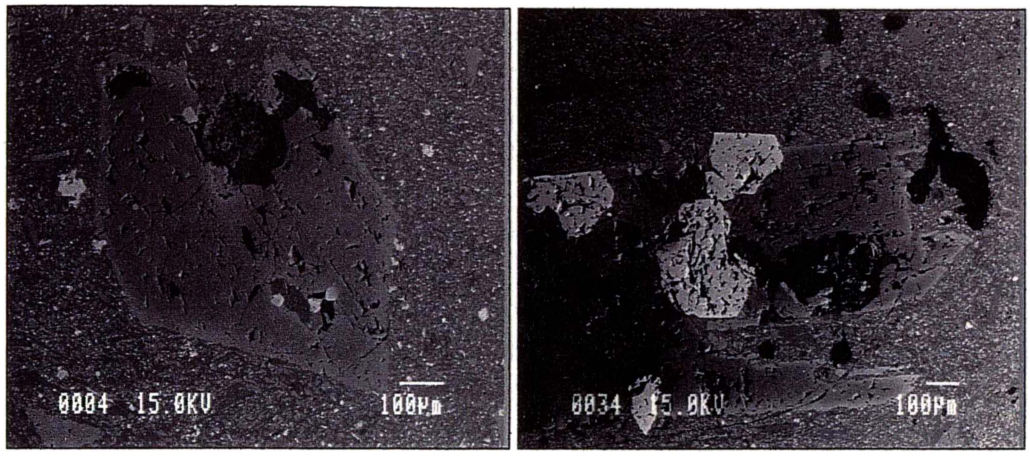

Fig.3.14: Zoned olivine phenocrysts in primitive basanite *(a)* and low alkali basanite *(b)*. (back scattered electron microscope images)

None of the olivine crystals analysed in the more evolved rock types shows any compositional zoning. The evolved basanite group (samples 3, 97) contains olivine with compositions ranging from Fo_{64}-Fo_{59}. The high silica basanite (sample 91) contains olivines with compositions from Fo_{54}-Fo_{38} and olivine in trachyte (sample 95) is extremely iron rich, with compositions of Fo_{19}–Fo_{18}. These compositional variations show that the olivines have crystallized from progressively more iron enriched melts, suggesting progressive differentiation as a consequence of crystal fractionation.

Calcium content in olivine is consistently low (0.12 to 0.47 wt% CaO) for all basanites and is slightly higher in the trachyte (0.84–1.13 wt% CaO). Kyle *(1981)* uses the lack of any rapid calcium increase in olivine with increasing differentiation to infer that decreasing temperature rather than decreasing pressure was the important physical factor during the progressive crystallisation of these rocks.

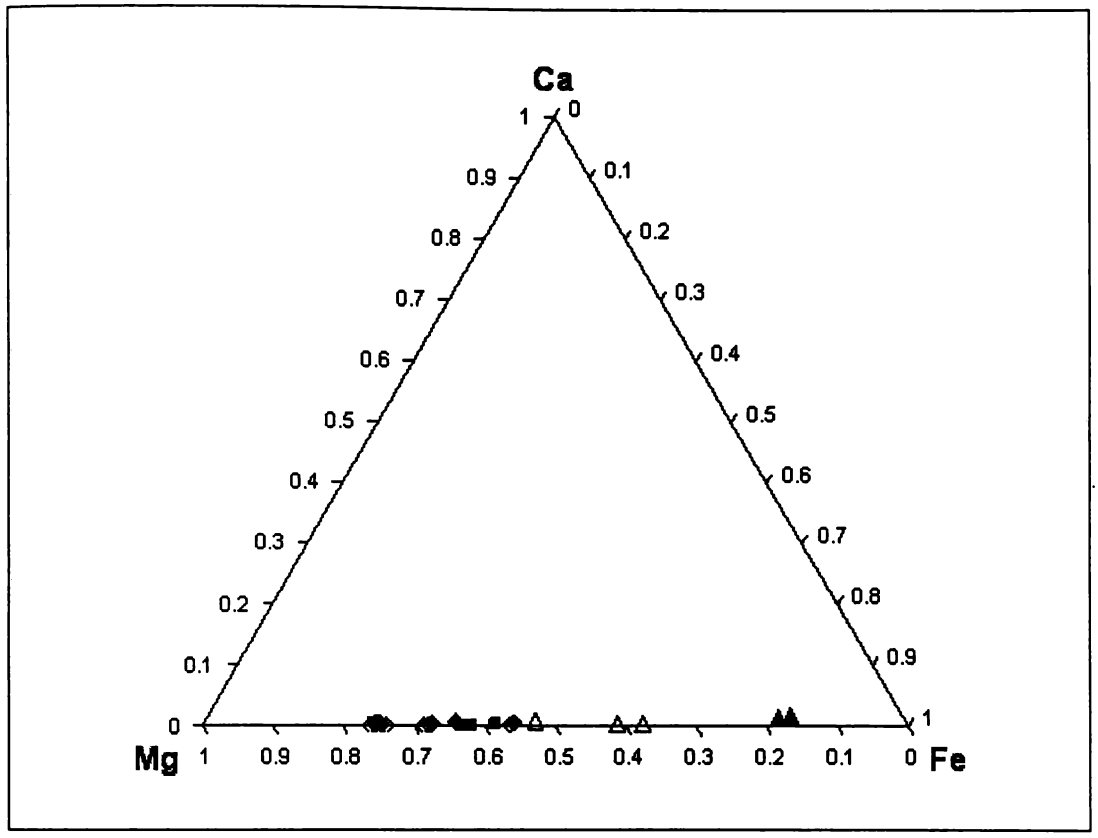

Fig.3.15: Compositions of olivine in Mount Morning rocks.

3.2.2 CLINOPYROXENE

The clinopyroxenes occurring as phenocrysts in basanite are classified as diopside (Fig.3.16) using the classification scheme of Morimoto *(1988)*. They show little variation in composition, although those from the low alkali basanite group (sample 21) are slightly poorer in iron than those from the evolved basanite group (samples 3, 97). Generally the pyroxenes in basanite are calcium (21.0-22.4 wt% CaO) and magnesium (11.4–15.0 Mg wt% MgO) rich with lesser amounts of iron (5.6–9.6 Fe wt%) and titanium (0.5-3.3 TiO_2 wt%).

Two pyroxenes crystals from trachyte were analysed, they are classified as diopside and hedenbergite in composition. They are calcium (19.5-21.4 wt% CaO) and iron (15.0–19.6 wt% FeO) rich, with little magnesium (<10 wt% MgO)

Although some pyroxenes show zoning patterns (e.g. Fig.3.10), none of the analysed pyroxene phenocrysts showed any compositional variations between the core and rim of the crystal.

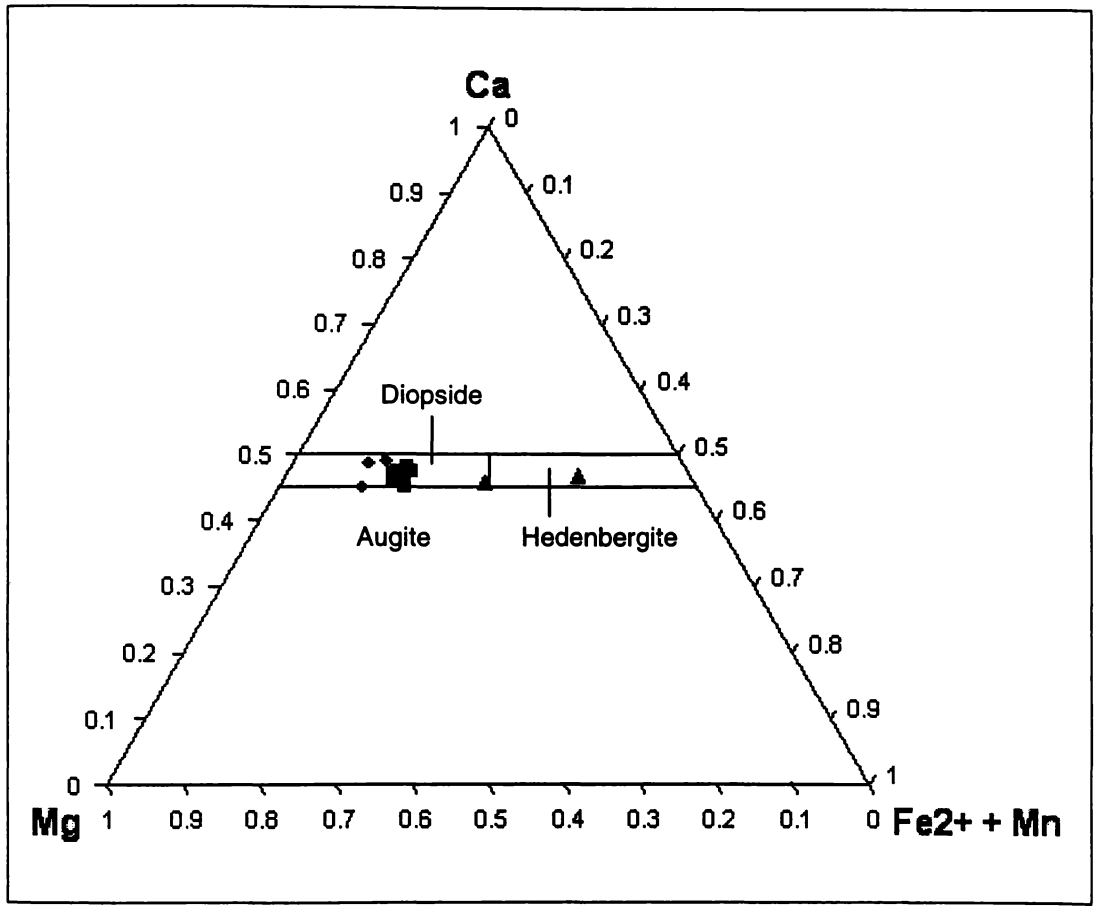

Fig.3.16: Classification of clinopyroxenes

3.2.3 OPAQUE OXIDES

Several different compositions of opaque oxides occur in the analysed rocks from the field area, these were classified with the classification scheme of Haggerty *(1981)* in Figure 3.18. The most primitive basanite samples (samples 21, 45) contain opaque oxides as chrome spinel. Two of these were analysed, one is an inclusion in a zoned olivine phenocryst (Fig.3.14) in low alkali basanite (sample 21), and the other is a phenocryst in primitive basanite (sample 45). Both of these crystals show compositional zoning, although it is more prominent in the analysed crystal from sample 45. The cores of these crystals are rich in aluminium (20.4-29.1 wt% Al_2O_3), chromium (29.5-40.1 wt% Cr_2O_3) and magnesium (10.1-13.5 wt% MgO) while the rim is composed of mainly iron (51.4-52.7 wt% FeO*) and titanium (13.8-14.8 wt% TiO_2).

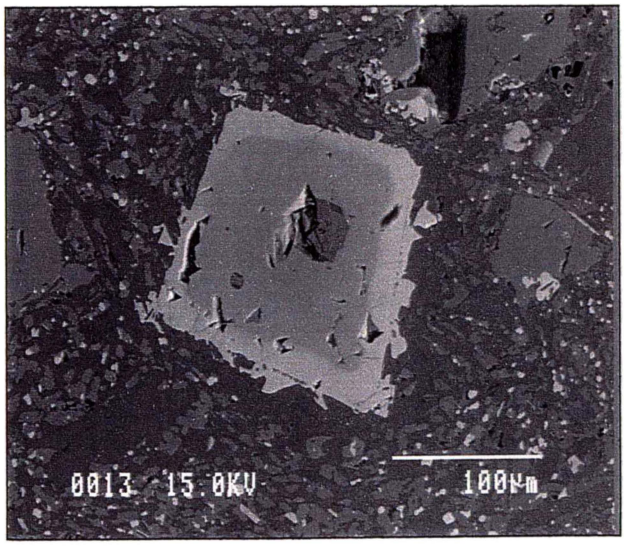

Fig.3.17: Back scattered electron microscope image of a chrome spinel in primitive basanite, showing a zoning pattern.

The evolved basanites contain small opaque grains of two compositions, titanomaghematite only in sample 3 and ilmenite only in sample 97. Titanomaghematite crystals are iron rich (28.8-31.1 wt% FeO, 39.7-40.3 wt% Fe_2O_3) with lesser amounts of magnesium, titanium and aluminium. The ilmenites analysed are titanium (42.1-53.9 wt% TiO_2) and iron (40.3-50.4 wt% FeO) rich.

High silica basanite and trachyte contain magnetite with less titanium and magnesium but very high iron contents, up to 75 wt% FeO* in some crystals from trachyte.

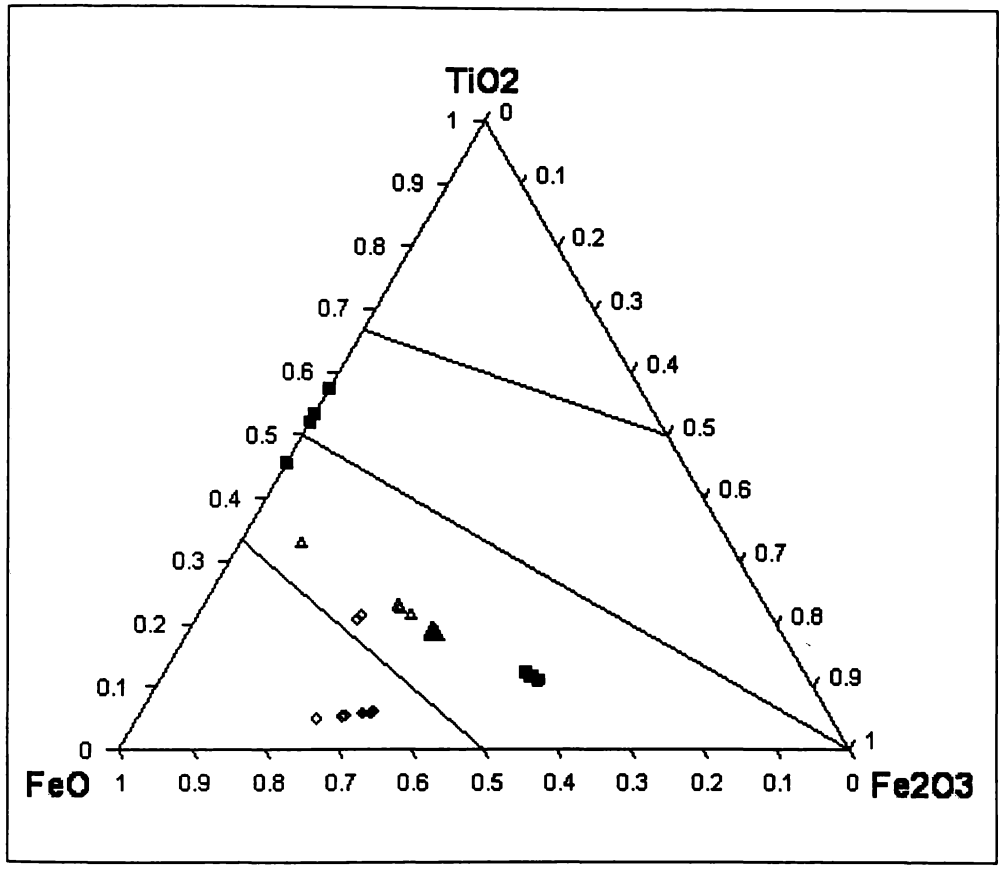

Fig.3.18: Classification of opaque oxides

The chrome spinel phenocrysts in the primitive and low alkali basanites probably have a xenolithic origin but the other opaques appear to have crystallised from their host magma. There is a general decrease in magnesium and an increase in iron content of these opaque oxides with increasing differentiation of the host rocks and this is consistent with crystallisation from melts that have progressively decreased in magnesium and increased in iron content as olivine and pyroxene have fractionated. Coexisting magnetite and ilmenite are not found in any of the analysed samples

3.2.4 FELDSPAR

Plagioclase is the dominant feldspar present, with a wide range of compositions from An_{24}–An_{75} including oligooclase, andesine, labradorite and bytownite. The alkali feldspars anorthoclase and sanidine are rare.

The most primitive basanites (low alkali and primitive basanite groups) contain the most calcium rich feldspars (labradorite – bytownite) and there is very little variation in composition among the crystals analysed (An_{69} –An_{75}).

The evolved basanites contain calcium rich plagioclase feldspars with more alkali rich compositions rare. Feldspars in sample 3 have a small range of compositions from labradorite to bytownite (An_{59} - An_{73}). One of these occurs in association with quartz suggesting it origininated from a disaggregated lower crustal granulitic or upper crustal granite xenolith. Plagioclase in granulites and pyroxenites from Mounts Sidley and Hampton, Marie Byrd Land, were analysed by Wysoczanski *(1995)* and had compositions ranging from An_{39}-An_{77}. Assuming that granulites and pyroxenites from the McMurdo Volcanics have similar compositions then these plagioclase grains could feasibly be xenolithic in origin. Sample 97 contains a wide range of feldspar compositions, phenocrysts of labradorite were identified as well as zoned crystals

with large compositional differences between the core and rim of the crystal. For example an oligoclase crystal has an overgrowth of labradorite over and an andesine crystal has a rim of sanidine.

Feldspar in high silica basanite (91) occurs as andesine and labradorite, with a range of compositions from An_{39} to An_{55}. Feldspar occurring in trachyte (95) is both oligoclase (An_{27} to An_{30}) and anorthoclase in composition.

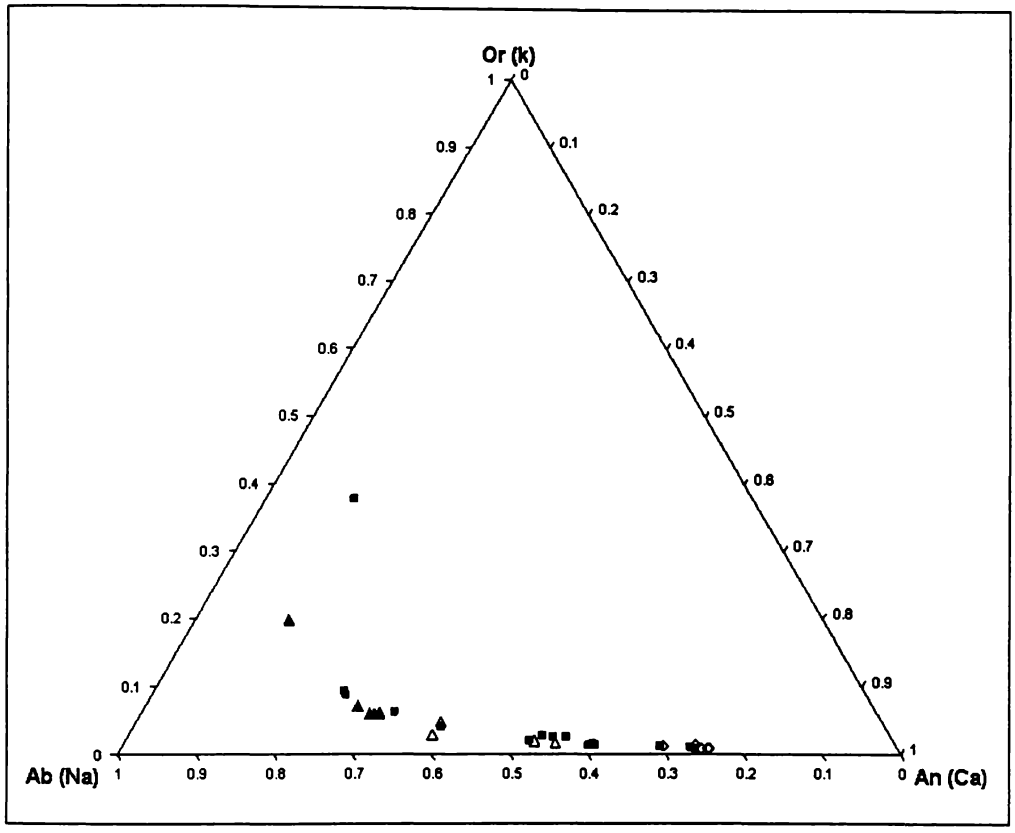

Fig.3.19: Orthoclase-Albite-Anorthoclase feldspar classification diagram

With increasing differentiation of the host rock the feldspars generally become more alkali rich, changing in composition from bytownite to labradorite to andesine and oligoclase. Some of the feldspar phenocrysts present may have originated from disaggregated crustal xenoliths and can be more correctly called xenocrysts.

3.3 MAGMATIC CONDITIONS

Kyle *(1976)* used the four geothermometers in attempt to determine the mineral crystallization temperatures for samples from the Pleiades, and DVDP drill holes 1 and 2. The gethermometers used were;

- magnetite-ilmenite *(Buddington and Lindsley, 1964)*
- plagioclase *(Kudo and Weill, 1970)*
- olivine-chromite *(Jackson, 1969)*

Of these four geothermometers, the Buddington and Lindsley *(1964)* magnetite-ilmenite geothermometer gave the most reliable temperature estimations, as long as the oxides analysed were not oxidised. Oxidation of the oxides results in the estimated temperatures being too low.

The olivine-clinopyroxene geothermometer of Powell and Powell *(1974)* is pressure dependent and gave satisfactory estimates of quench temperatures in Kyle *(1976)* following a correction for the depth of crystallization of phenocrysts. However even after corrections were made the temperatures were still lower than that expected.

The plagioclase geothermometer of Kudo and Weill *(1970)* used by Kyle *(1976)*, for a variety of McMurdo Volcanic Group rocks gave results consistently higher than experimental liquidus temperatures and were considered too high.

The olivine-chromite geothermometer of Jackson *(1969)* gave unsatisfactory results for DVDP basanites analysed by Kyle *(1976)*, leading to a suggestion that this geothermometer was not applicable to chromite analysed by electron microprobe in terrestrial igneous rocks.

Magnetite-ilmenite geothermometry was not possible in this study due to the absence of coexisting magnetite and ilmenite. The other three geothermometers were not considered due to the errors noted by Kyle *(1976)*. Three DVDP basanites analysed by Kyle *(1976)* gave temperature estimates ranging from 955-985 °C, calculated using the magnetite-ilmenite geothermometer of Buddington and Lindsley *(1964)*.

CHAPTER FOUR GEOCHEMISTRY

4.0 MAJOR ELEMENT CHEMISTRY

The analysed samples are all nepheline normative, indicating that they are silica undersaturated (Appendix 2.3). Normative nepheline ranges from 16–28 %. Normative leucite is also present in some samples at up to 6 % indicating extreme silica undersaturation.

In silica variation diagrams (Fig.4.1) the major element oxides show trends consistent with formation of these lavas by fractional crystallization of olivine, clinopyroxene and titanomagnetite, with amphibole, feldspar and apatite also fractionating in more evolved rocks. These fractionation trends are similar to those found for other basanite-phonolite series, e.g. Dry Valley Drilling Project *(Kyle, 1981)* Tristan da Cunha *(Le Roex et al., 1990)* and Dunedin Volcanics *(Coombs and Wilkinson, 1969).*

4.1 TRACE ELEMENT CHEMISTRY

On silica variation diagrams (Fig.4.2*a-d*) the ferromagnesian trace elements Ti, V, Cr, Ni, and Cu show progressive depletion in abundance from basanite to phonolite. This is consistent with these elements being compatible in and depleted by fractionation of

---

Symbols used are consistent across all plots (major element, minor element, REE, spider diagram)

- Trachyte solid triangle
- High Si basanite hollow triangle
- Evolved basanite solid square
- Primitive basanite hollow diamond
- Low alkali basanite solid diamond

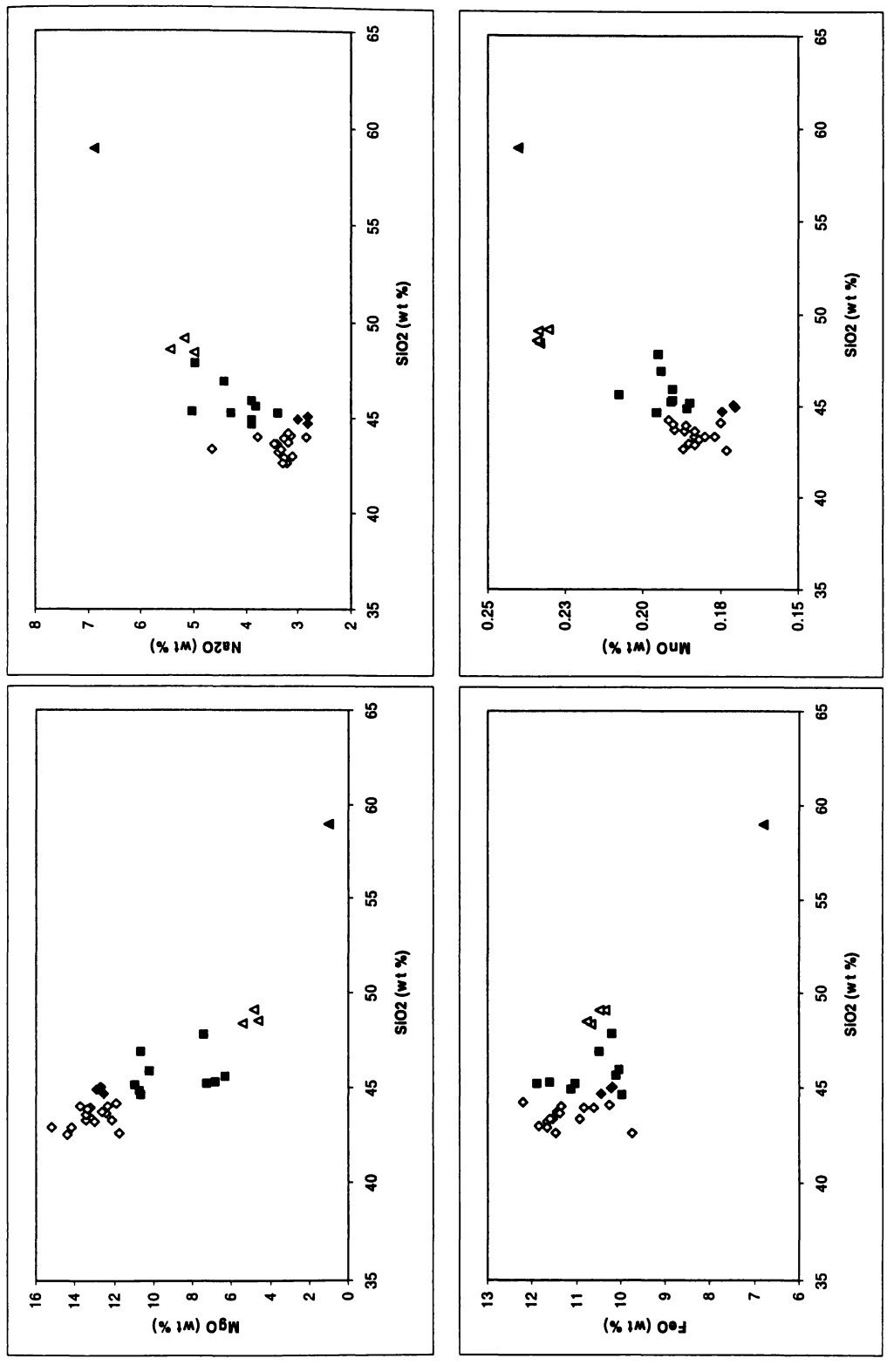
Na2O (wt %)
SiO2 (wt %)
MnO (wt %)
SiO2 (wt %)
MgO (wt %)
SiO2 (wt %)
FeO (wt %)
SiO2 (wt %)

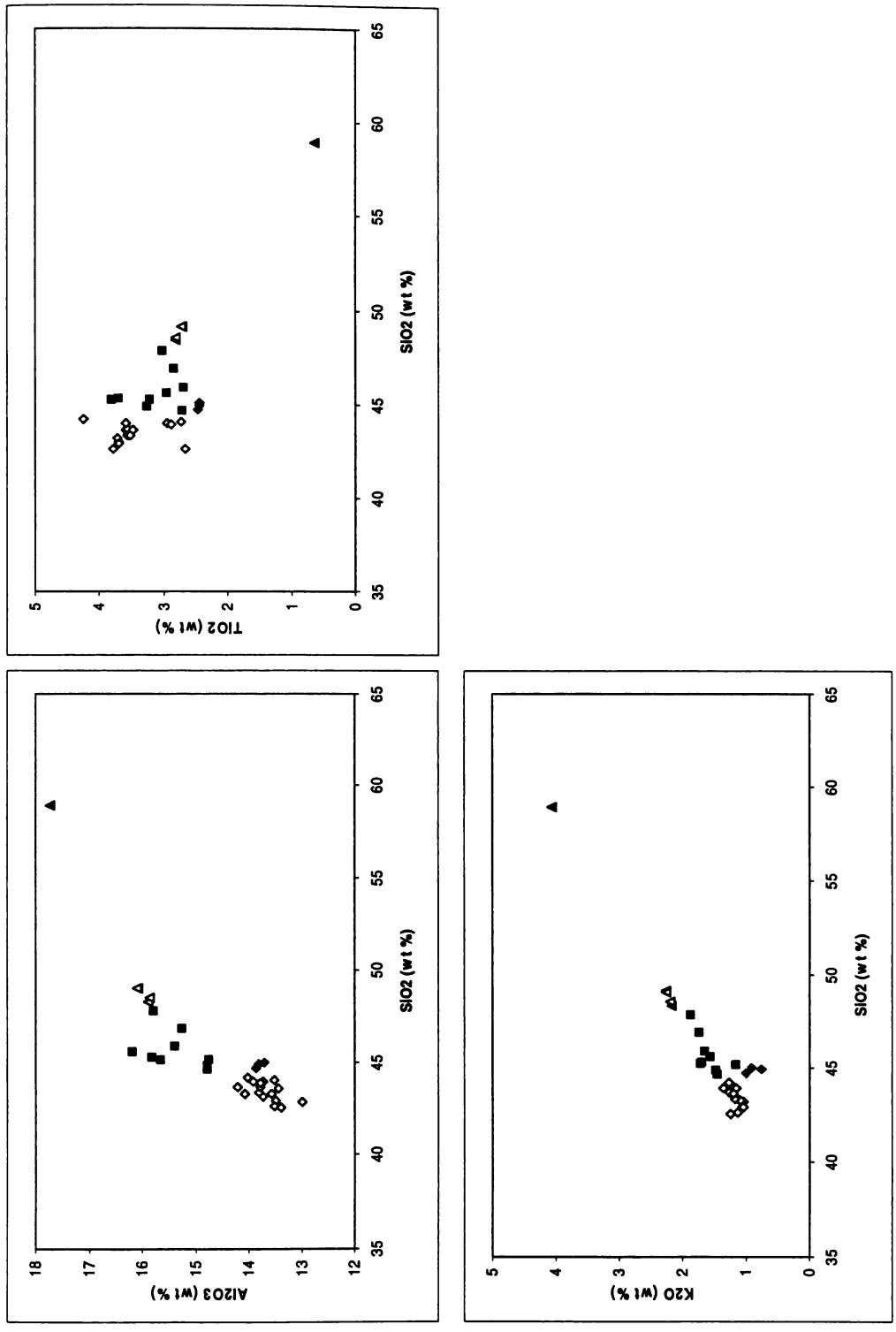

Fig. 4.1*a-g*: Variation of major element oxides plotted against silica.

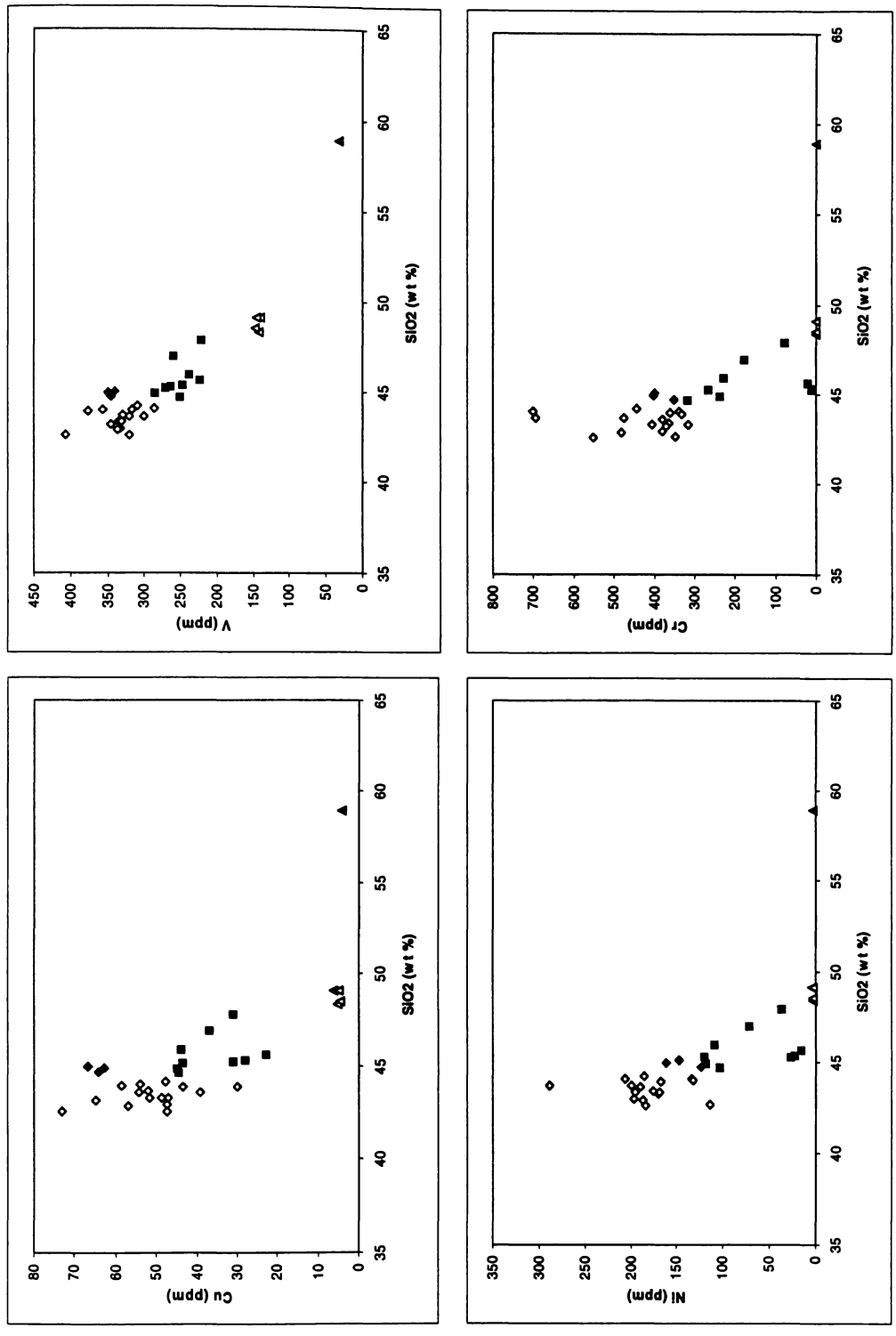

Fig. 4.2*a-d*: Variation of trace elements (Cu, V, Ni, Cr) plotted against silica.

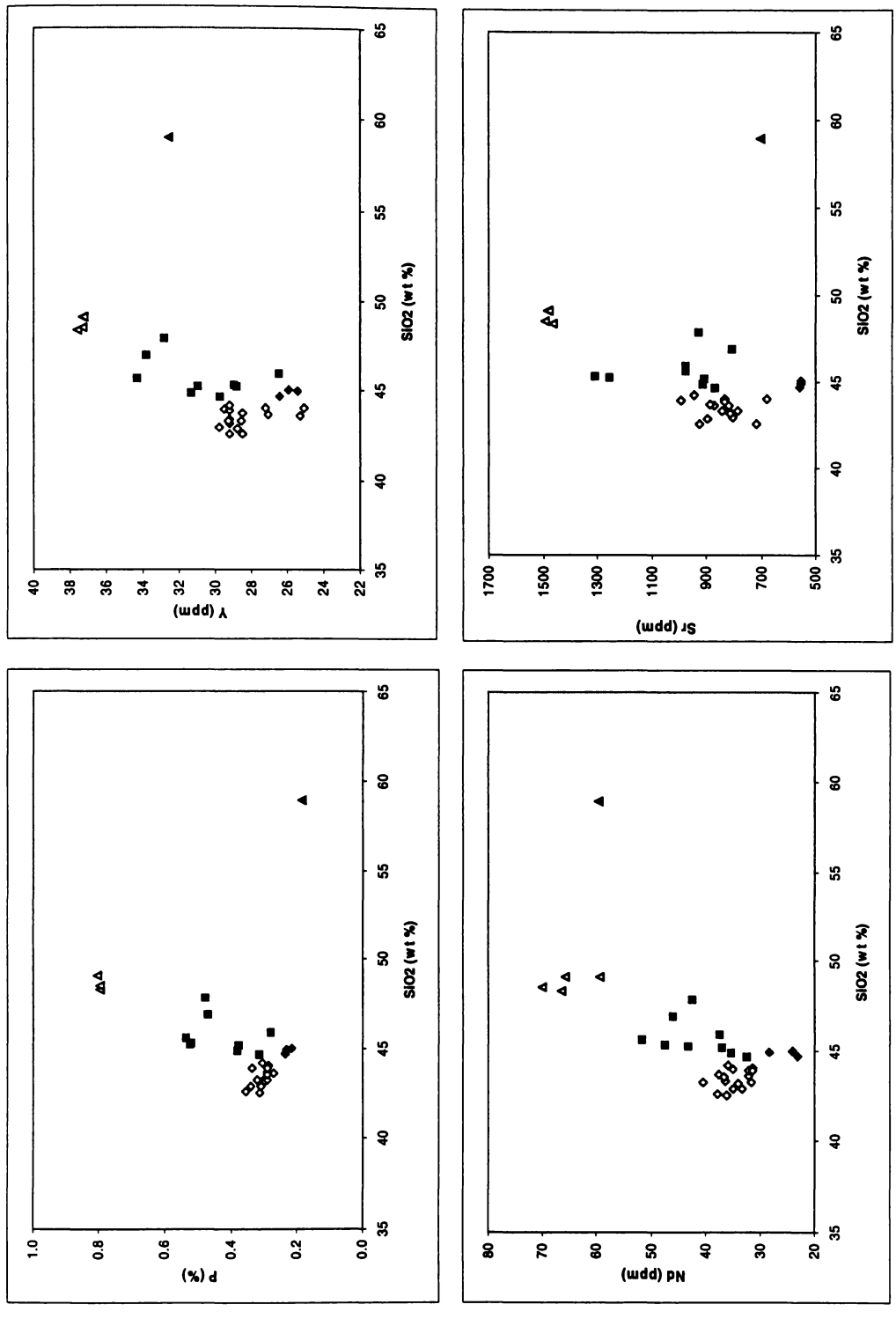

Fig. 4.3*a-d*: Variation of trace elements (P, Y, Nd, Sr) plotted against silica.

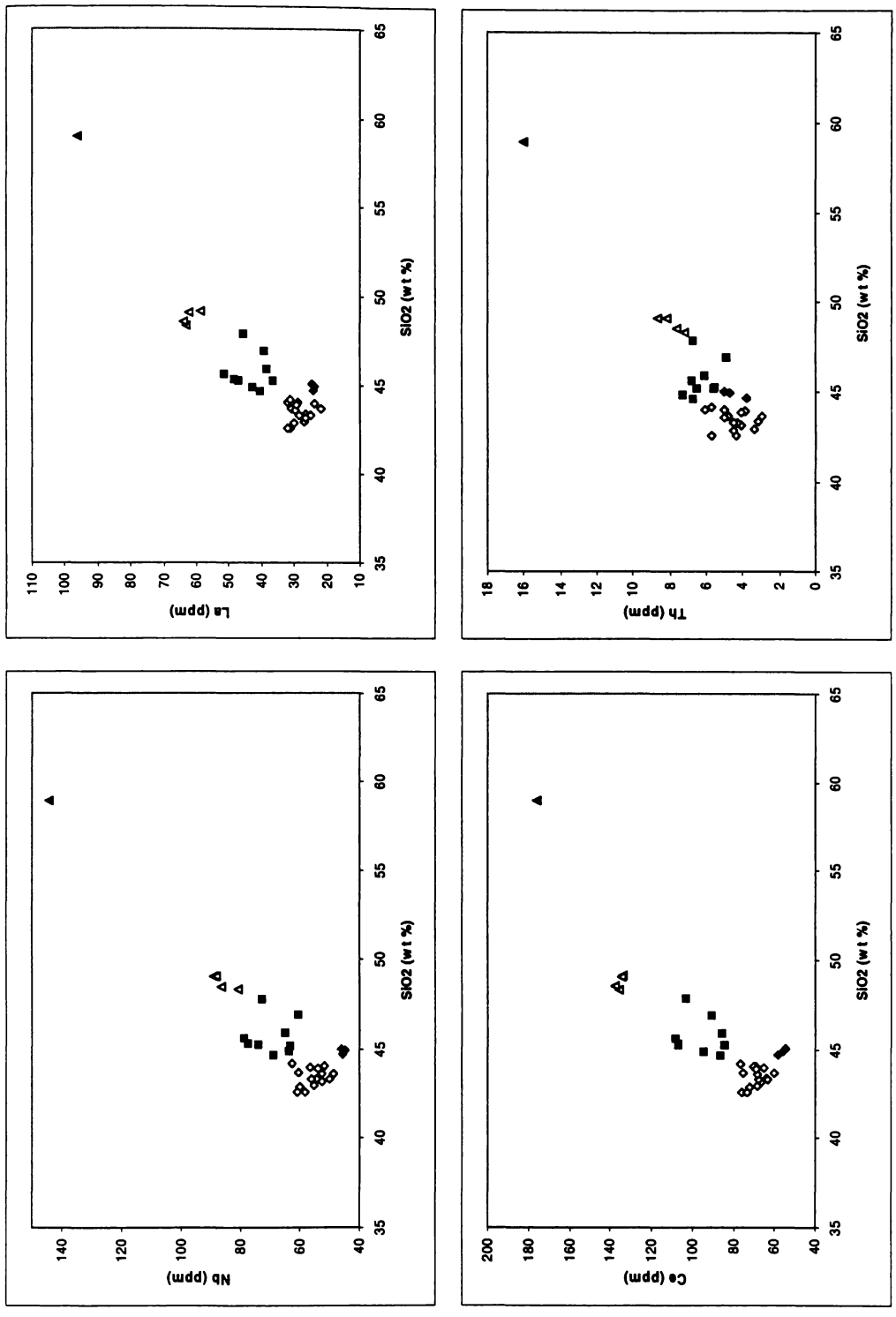

Fig. 4.4*a-d*: Variation of trace elements (Nb, La, Ce, Th) plotted against silica.

olivine, clinopyroxene and titanomagnetite *(Hall, 1987)*. Chromium and nickel show the most striking depletions, decreasing from over 700 and 200 ppm respectively in the most primitive basanites to less than 3 ppm in the highest silica basanites.

The trace and minor elements phosphorous, yttrium and neodymium all behave similarly (Fig.4.3*a-c*), showing progressive enrichment from low to high silica basanites, followed by depletion in the trachyte. These elements are incompatible in the olivine, clinopyroxene, amphibole and titanomagnetite being fractionated as the basanites evolved, but they are compatible in and depleted by the fractionation of apatite *(Hall, 1987)*.

Strontium is progressively enriched through the basanites and then depleted in trachyte (Fig.4.3*d*). It is behaving incompatibly in basanite and then being removed by the fractionation of feldspar or apatite in trachyte. Because feldspar fractionation is thought to be insignificant it is likely that apatite is the main phase removing strontium.

The trace elements rubidium, zircon, niobium, barium, lanthanum, cerium, hafnium, lead and thorium all behave similarly (Fig.4.4*a-d*), showing strongly linear enrichment from primitive to evolved basanite to trachyte. This shows that they are incompatible in the fractionating mineral assemblage and are concentrated in the remaining melt.

4.2 RARE EARTH CHEMISTRY

The rare earth element (REE) chemistry was determined by inductively coupled plasma mass spectrometry (ICP-MS) for a selection of 10 samples representative of the compositional range present.

The samples analysed were;

- Trachyte (sample 95)
- High silica basanite (sample 91)
- Evolved basanite (samples 3, 23, 28, 97, 98)
- Primitive basanite (samples 2, 45)
- Low alkali basanite (sample 21)

The chondrite normalized REE diagram (Fig 4.5) shows a large enrichment of all rare earth elements. The light rare earth elements (La, Ce) are enriched to over 100 times the chondrite values for all samples and the heavy rare earth elements are all enriched to greater than 10 times chondrite values. Enrichment of the light rare earth elements relative to the heavy rare earth elements is typical of alkalic intraplate basalts *(Cook et al., 2005).*

There is a uniform enrichment in all rare earth elements with increasing differentiation from the low alkali → primitive → evolved → high silica basanites, shown by increasing, roughly parallel trend lines on the REE plot. Compared to the basanites, the trachyte shows enrichment in the light and heavy rare earths, and a depletion of the middle rare earth elements.

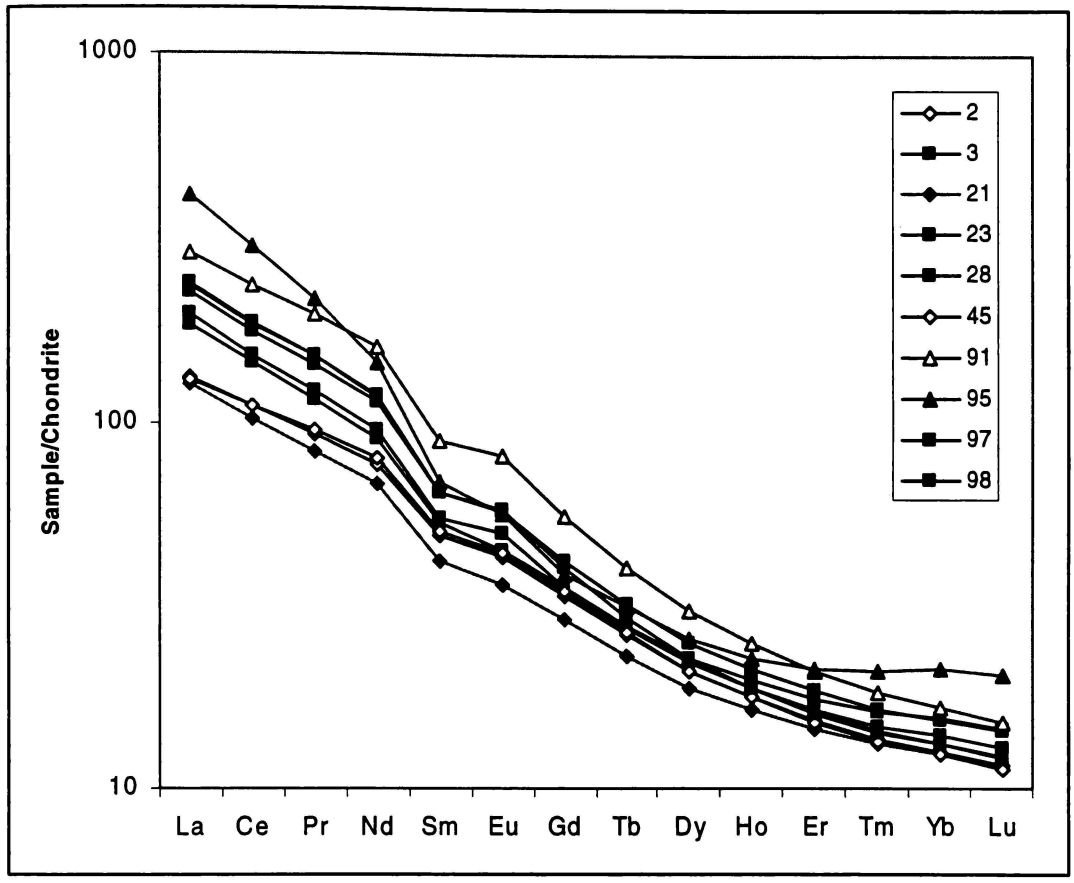

Fig.4.5: Rare earth element chemistry of representative Mount Morning samples. Chondrite normalized using the values of Evenson *(Rollinson, 1993)*.

Figure 4.6 plots the rare earth data normalized against the most primitive basanite in the field area (sample 45), this shows more clearly the variations between each sample. This also shows the enrichment in rare earth elements from the most primitive to the more evolved basanites.

The trachyte is highly enriched in the LREE and HREE and depleted in the middle REE. Kyle *(1979)* reports that fractionation of kaersutite normally results in a large depletion of the middle rare earth elements, so this pattern may indicate a large involvement of kaersutite during the fractionation of this trachyte.

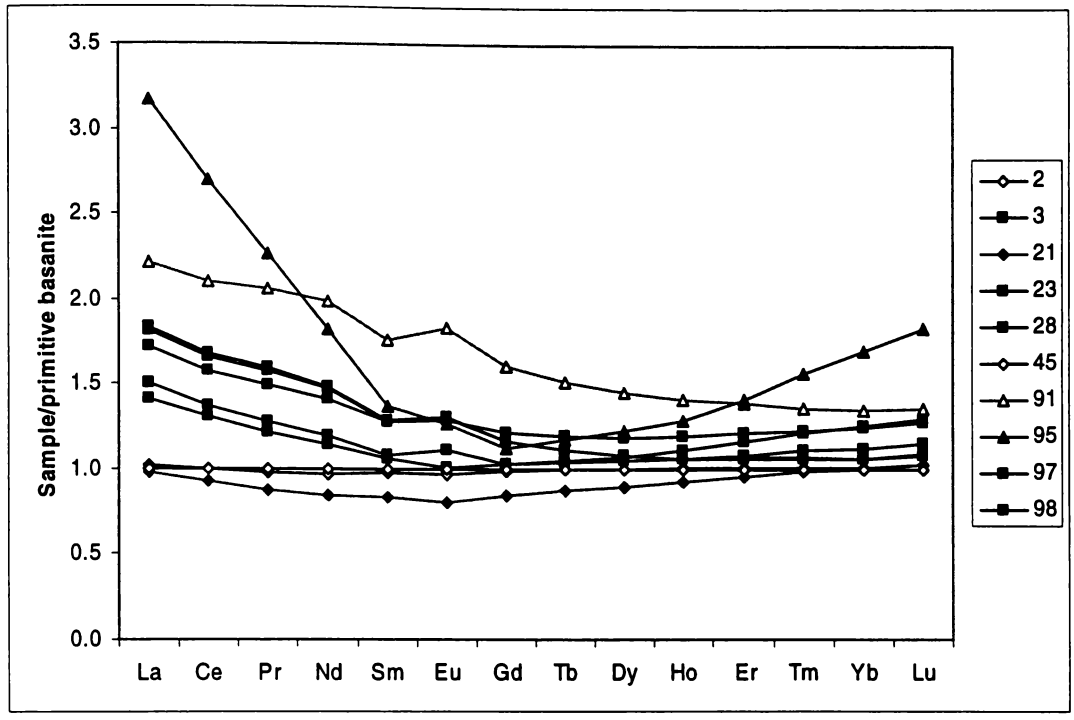

Fig.4.6: Rare earth element chemistry of representative Mount morning samples. Normalised to the most primitive basanite (sample 45)

The basanite samples all show a consistent pattern when plotted on a primitive mantle normalised trace element diagram (Fig.4.7) There is a general decrease from left to right with decreasing incompatibility. The main disruptions to this pattern are a small negative thorium anomaly and a larger positive niobium anomaly. As with the rare earth elements these trace elements also show a uniform increase from the most primitive to the most evolved basanites, this is the result of incompatible elements being concentrated in a melt as fractional crystallization occurs.

Trachyte shows a different pattern to the basanites. It is even more enriched in most elements and shows large negative anomalies for strontium, phosphorous and titanium and positive anomalies of niobium and zirconium.

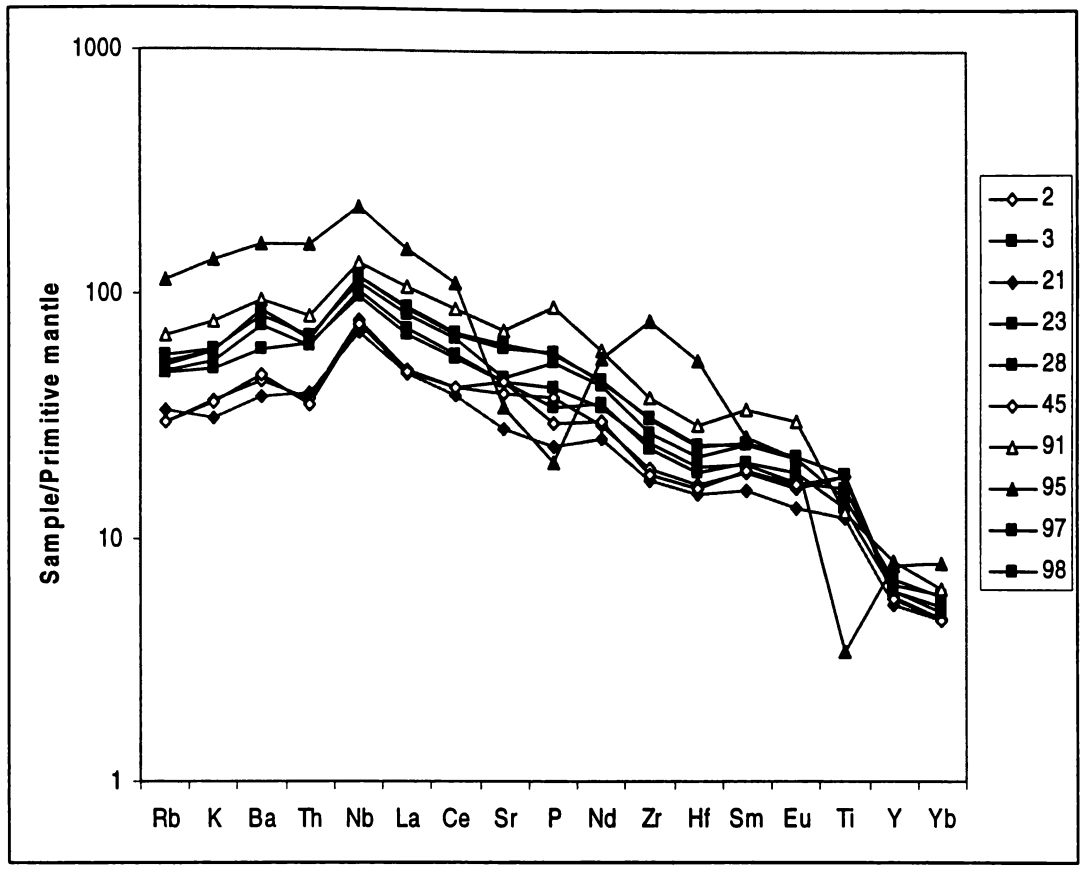

Fig.4.7: Primitive mantle normalized incompatible trace element diagram for selected Mount Morning samples analysed by ICPMS. Normalisation factors from McDonough and Sun *(1995)*.

CHAPTER FIVE XENOLITHS

5.0 INTRODUCTION

Mantle xenoliths or mantle nodules are rock and mineral inclusions of presumed mantle derivation found within host rocks of volcanic origin (*Pearson et al., 2004*). These disrupted fragments of the Earth's upper mantle provide a way of looking at the petrology of the lithosphere and understanding the processes occurring in it (*Gamble et al., 1988*).

Mantle rocks are exposed as peridotite massifs in ophiolite complexes generated at plate boundaries, for example the Dun Mountain ultramafic belt in the South Island of New Zealand *(Coombs et al., 1976)*, and the Troodos Massif in Cyprus *(Moores and Vine, 1971)*. But in many regions, mantle xenoliths are the only samples we have of the underlying mantle. Mantle xenoliths give us a view of the lithospheric mantle characteristics at the time of eruption of the host lava (*Pearson et al., 2004*).

Because xenoliths are rapidly erupted and cooled, the mineralogical and chemical features of their depth of origin are retained (*Pearson et al., 2004*). The texture and composition of xenoliths can be used to estimate the temperature, pressure and stress conditions existing before the xenoliths were entrained in the host lava (*Pearson et al., 2004*). They are inferred to be from the mantle because their mineralogy has been demonstrated by thermobarometric experiments to require high pressure (*Pearson et al., 2004*).

Texture and grain size of olivine in xenoliths have been used to infer stress and strain rates and viscosity as functions of depth or tectonic setting. For example, Ross *(1983)* estimated stress as a function of depth for peridotites from British Columbia using grain-size paleopiezometry and pyroxene thermobarometry.

There are many textural classifications for xenoliths, such as those of Pike and Schwarzman *(1977)* and Harte *(1977)*. Harte's *(1977)* classification scheme is one of the common classifications used. This has four categories;

1. Coarse: Lacking porphyroclasts and formed by grains mostly >2 mm, grain boundaries may be straight, curved or irregular.
2. Porphyroclastic: Contains porphyroclasts (large grains surrounded by much smaller grains) in a fine grained olivine matrix, >10 % of the olivine present occurs as porphyroclasts.
3. Mosaic-porphyroclastic: Contains porphyroclasts in a fine grained olivine matrix, >90 % of the olivine present occurs in small grains with a mosaic texture (approximately equigranular, polygonal).
4. Granuloblastic: Contains few porphyroclasts (<5 %) and is fine grained (typically <2 mm).

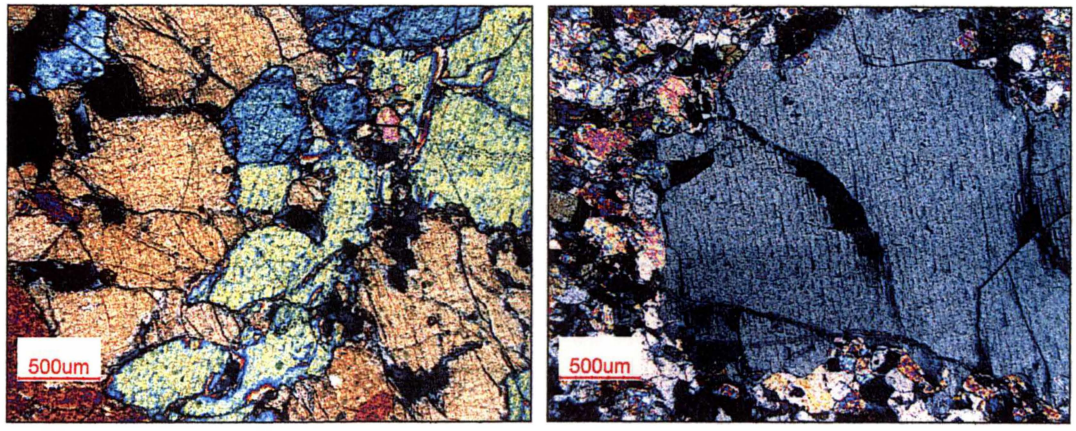

Fig.5.1: Coarse textured xenolith *(a)* comprising equigranular olivine and pyroxene, and a porphyroclastic textured xenolith *(b)* with a large pyroxene crystal set in a matrix of smaller olivine grains.

A coarse texture (Fig.5.1*a*), is thought to represent small constant stresses causing a stable grain size. A porphyroclastic texture (Fig.5.1*b*) with small olivine crystals

between larger and stronger pyroxenes, garnets or spinel indicates higher differential stresses. Some xenolith suites show a gradation between the two textures that appears to be dependent on depth, with porphyroclastic textures occurring at higher temperatures and depths (*Pearson et al., 2004*).

Thermobarometry is the use of rock compositions and mineral assemblages to determine the temperatures (geothermometry) and pressures (geobarometry) at which they were formed *(Hancock and Skinner, 2000).*

Pearson *et al.* (*2004*) noted three main purposes to thermobarometric investigations of mantle xenoliths. They are:

1. Providing a depth interval and minimum lithosphere thickness sampled by a magma.
2. Using inferred temperatures and pressures to give a spatial context between xenolith samples.
3. Defining a pressure-temperature gradient for the time of the eruption.

For example, a thermobarometric study was carried out by Kukkonen and Peltonen *(1999)* on xenoliths found in a kimberlite in eastern Finland. They formed a thermal model of the lithosphere in the area, establishing a lithosphere thickness of 240 km and temperatures of 1200–1400°C at depths of 200–240 km, this is shown graphically in figure 5.2. From this model they estimated an average temperature gradient of 3.7±0.6 °C /km and a heat flow density of 11±4 mW/m^2 in the mantle under this kimberlite pipe area.

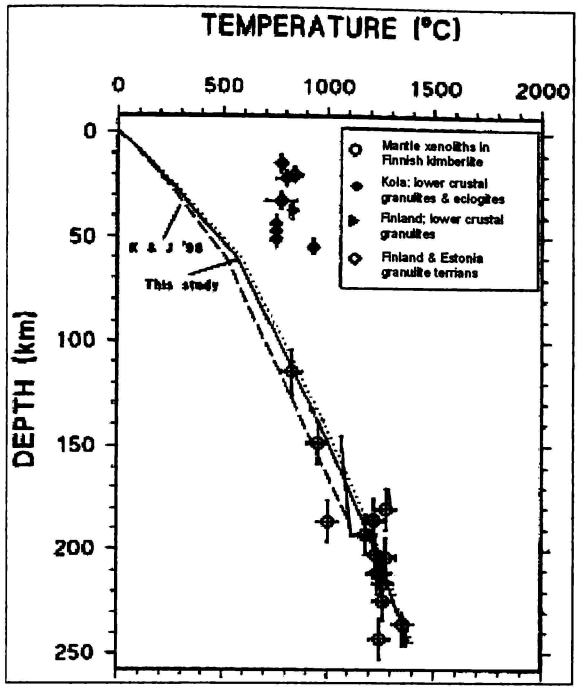

Fig.5.2: Geothermobarometric model calculated by Kukkonen and Peltonen *(1999)* showing their proposed geotherm for the area (solid line) and a model from an earlier study (dashed line) and the calculated depth and temperature conditions for mantle xenoliths and crustal granulites.

There have been a number of thermobarometers developed to estimate the pressure and temperature of mantle xenoliths. Generally these work by using exchange equilibria of various elements between minerals. Most geobarometry is confined to garnet facies xenoliths; there is currently only one quantitative geobarometer available for spinel facies xenoliths (*Pearson et al., 2004*). A geothermobarometric study of mantle xenoliths from Foster Crater, Antarctica by Gamble *et al.* (*1988*) using various methods concluded that the xenoliths formed at temperatures in the range 800-950 °C and pressures near 5 kb. This implies a formation depth of 14-20 km.

Mantle xenoliths are usually found in volcanic rocks where they have been brought to the surface by high velocity alkaline eruptions (*Bailey, 1987*). Mantle xenoliths are most commonly found in three types of alkaline magmas:

1. Alkali basalts
2. Lamprophyres
3. Kimberlites

But they have also been found occasionally in more evolved alkaline magma types such as phonolite and trachyte (*Pearson et al., 2004*).

5.1 XENOLITHS IN ALKALI BASALTS

Peridotites, pyroxenites and megacrysts are commonly found in:

- Basanitic scoria cones
  - e.g. Foster Crater, Transantarctic Mountains, Antarctica (*Gamble et al., 1988*).
- Maar-diatreme tuff rings
  - e.g. Lake Eacham, Australia (*Irving, 1980*).
- Alkaline lava flows
  - e.g. West Eifel Volcanic Field, Germany (*Shaw and Eyzaguirre, 2000*).
  - São Tomé Island, South Atlantic (*Caldeira and Munhá, 2002*).
- Vent plugs
  - e.g. Kauai, Hawaii (*Johnston et al., 1985*).
  - Nunatak Region, Northeast Greenland (*Bernstein et al., 2000*).
- Dikes and sills
  - e.g. Lajitas, Texas, USA (*Barker, 2000*).
- Agglomerates
  - e.g. Igwisi Hills (*Reid et al., 1975*).

In this case the host rock is a conglomerate with a composition similar to kimberlite.

5.2 XENOLITH TYPES

There are two main types of mantle xenoliths; they are generally classified with the nomenclature of Wilshire and Shervais *(1975)*, modified later by Frey and Prinz *(1978)*. This classification scheme assigns common mantle xenoliths into two series;

1. Cr-Diopside series (Type I)
2. Fe-Ti augite series (Type II)

They can be classified using their modal proportions in the nomenclature recommended by the IUGS Subcommision on the Systematics of Igneous Rocks and shown in figure 5.3.

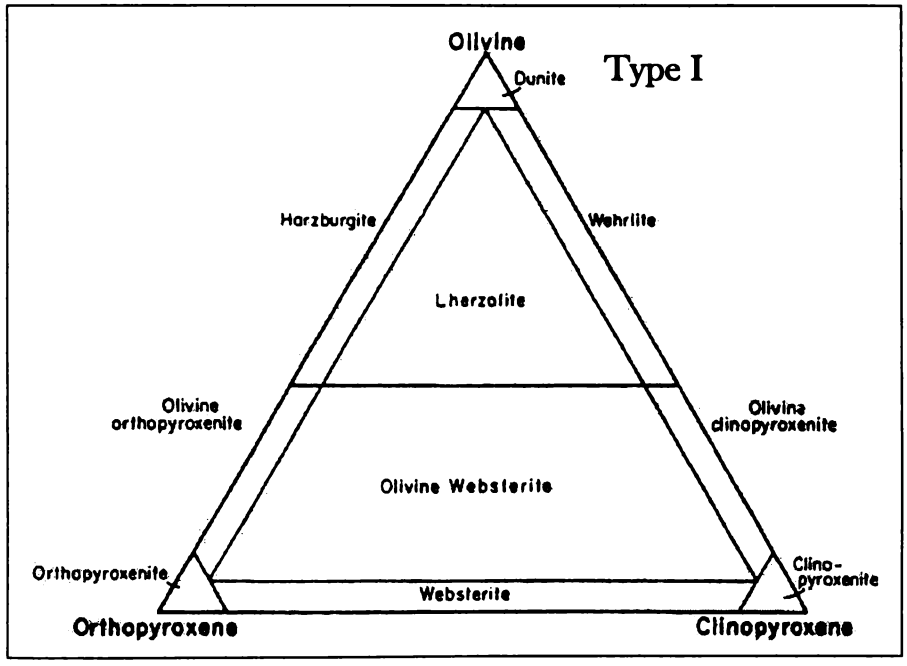

Fig.5.3*a*: Classification diagram for Type I mantle xenoliths *(adapted from Frey and Prinz, 1978).*

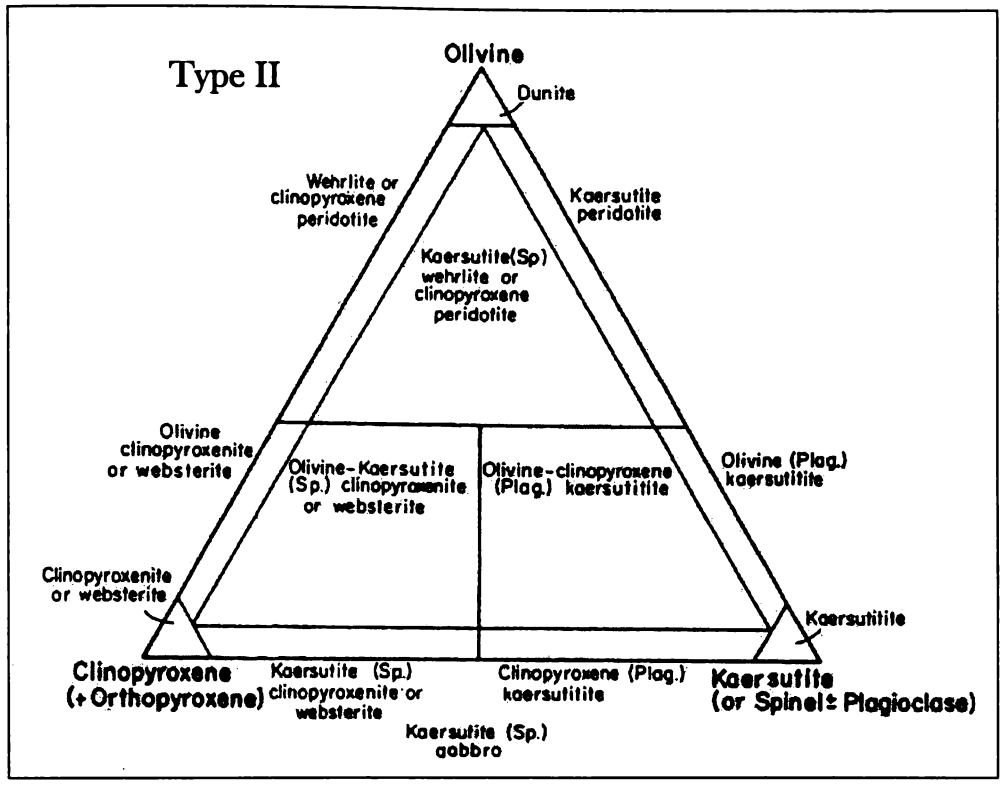

Fig.5.3*b*: Classification diagram for Type II mantle xenoliths *(adapted from Frey and Prinz, 1978).*

Mantle xenoliths of the Cr-Diopside series (Type I) are the most abundant and widespread (*Irving, 1980*) and have a relatively uniform mineralogy and chemistry (*Carswell, 1980*). Type I xenoliths are fragments of mantle wall rock that have been disrupted and carried to the surface by magma. The majority of these nodules are four phase lherzolites containing olivine, orthopyroxene, clinopyroxene and either spinel or garnet. Type I xenoliths found in kimberlites are usually spinel-free garnet lherzolites, while garnet-free spinel lherzolites in usually found in alkali basalts (*Carswell, 1980*).

Garnet free spinel lherzolites can be subdivided (*Carswell, 1980*) into;

- Al-Spinel lherzolites
- Cr-Spinel lherzolites
- Chromite lherzolites

Mantle xenoliths in the Fe-Ti augite series (Type II) are more varied in mineralogy and composition than the Type I xenoliths and are distinguished by being rich in clinopyroxene, usually augite (*Carswell, 1980; Menzies, 1983*). There are several theories to explain their formation, but the processes that form them are still relatively controversial. They are thought to be magmatic cumulates (*Carswell, 1980*) or precipitates (*Menzies, 1983*) from magma types similar to their host rocks. Irving (*1980*) proposed that they are formed as igneous crystal deposits on wall rocks as magma moves through conduits in peridotite at pressures of 15-25 kb.

Megacrysts are very common in kimberlites and are also found in alkali basalts. Megacrysts are large crystals, up to several centimeters in size (*Irving and Frey, 1984*). They can be olivine, clinopyroxene, orthopyroxene, spinel, apatite, amphibole, garnet, anorthoclase, ilmenite, mica, diamond and zircon.

Their origin is still uncertain, but they may be:

- High-pressure phenocrysts from the host magma
- Fragments of xenoliths (Types I, II)
- Fragments of pegmatitic mantle vein systems or cumulates

(*Shaw and Eyzaguirre, 2000*)

Megacrysts can be divided into two groups, A and B, on the basis of their relationship to their host magma. Group A megacrysts are cognate with their host magma and are thought to have crystallized from their host or a very similar magma. Common Group

A megacrysts are Al-rich augite, orthopyroxene, amphibole, spinel and garnet (*Schulze, 1987*).

Group B megacrysts are not in equilibrium with their host magma so are thought to have an accidental origin and can be more correctly called xenocrysts. They probably formed from magmas more evolved than their hosts. Group B xenocrysts include feldspars, mica, clinopyroxene, apatite, ilmenite, zircon, corundum, sphene, magnetite and rutile (*Schulze, 1987*).

In addition to the mantle xenoliths and megacrysts, xenoliths from all levels of the crust may also be entrained and brought to the surface by alkali basalts.

5.3 XENOLITHS IN ANTARCTICA

Mantle and crustal xenoliths have been found in the Cenozoic volcanic deposits of both the McMurdo Volcanic Province (*Kyle et al., 1987*) and the Marie Byrd Land Volcanic Province *(Wysoczanski et al., 1995)* on either side of the West Antarctic Rift system (Fig.1.1), as well as at locations on the Antarctic Peninsula *(Keller and Strelin, 1992; Herve et al., 1996).*

5.3.1 XENOLITHS IN THE MCMURDO VOLCANIC GROUP

Xenoliths have been known to occur in the McMurdo Sound area since 1907 when they were discovered by Ferrar and reported on by Prior (*Kyle et al., 1987*). Further work during the "heroic age" of Antarctic exploration was carried out by Thomson in 1916 who reported on a suite of xenoliths collected from Hut Point Peninsula on Ross Island (*Kyle et al., 1987*).

Xenoliths have been found in the Melbourne, Hallet and Erebus Provinces of the McMurdo Volcanic Group, but the only detailed studies undertaken have all been at localities within the Erebus Province. Kyle *et al.* (*1987*) reported 48 known xenolith localities in the McMurdo Volcanic Group. Others have been discovered since that time and there are likely to be many more unknown xenolith localities under snow and ice cover or at sites not yet investigated.

As well as mantle xenoliths, inclusions from all levels of the crust have been also been discovered in the volcanic rocks of the McMurdo Volcanic Group *(Berg, 1991)*:

- Supracrustal; sandstone and dolerite
- Upper-crustal; granite, quartzite, schist and marble
- Lower-crustal; mafic granulites
- Ultramafic; peridotites, pyroxenites and megacrysts

McGibbon (*1991*) reports that xenoliths are found only in basanitic scoria cones while Berg (*1991*) found xenoliths as bombs in scoria cones and as inclusions in lava flows.

Three main types of ultramafic xenoliths are found in Erebus Province:

1. Spinel lherzolites with Mg,Cr-rich diopside (Type I xenoliths) *(McGibbon, 1991)*
2. Augite clinopyroxenites with Fe,Ti-rich clinopyroxenes (Type II xenoliths) *(McGibbon, 1991)*
3. Fassaitic clinopyroxenites containing calcic clinopyroxenes (only found at Foster Crater) *(Gamble et al., 1988)*

The Type I Spinel lherzolites are thought to be mantle samples with no cognate relationship to the host lavas. The Type II xenoliths (pyroxenites and wehrlites) are thought to be cumulates from undersaturated magmas similar to their host lavas

(*McGibbon, 1991*) No garnet bearing nodules have been identified anywhere in the McMurdo Volcanic Group (*Kyle et al., 1987*)

Megacrysts of clinopyroxene, kaersutite and anorthoclase from Ross Island and vicinity analysed by Stuckless and Erickson (*1976*) were isotopically indistinguishable from their host rocks, and it was therefore suggested that they probably crystallized from the host. Megacrysts usually occur with other ultramafic and crustal xenoliths but some locations are known where megacrysts are the only xenoliths (*Kyle et al., 1987*).

The most common lower-crustal inclusions are two-pyroxene and clinopyroxene granulites (*Berg, 1991*). There are distinct compositional differences between those granulites occurring in the Transantarctic Mountains and the Ross Embayment. The granulites discovered in the Ross Embayment are low in incompatible and high in compatible elements and are thought to have formed as cumulates. Those from locations in the Transantarctic Mountains are higher in incompatible and lower in compatible elements compared to the Ross Embayment granulites, and are thought to represent melt compositions. (*Kalamarides and Berg, 1991*)

Upper-crustal inclusions of granite and metamorphic rocks, mostly quartzites, occur as inclusions throughout the Erebus Province Volcanics but are most common at sites in the Transantarctic Mountains *(Berg, 1991).*

Supracrustal inclusions occur only in McMurdo Volcanic occurrences in the Transantarctic Mountains, such as the Taylor Valley and Roaring Valley. They include Ferrar Dolerite and several sandstones and carbonate rocks *(Berg, 1991).*

5.3.2 XENOLITHS ON MOUNT MORNING

Ultramafic and crustal xenoliths, and megacrysts were found within the field area on Mount Morning. Ultramafic xenoliths were found only in the deposits of Scoria Cone 4. They occur in a flow at the northeast end of the cone, in a large (approximately 1 km long x 1-5 m thick) basanitic dike at Locality 74 on the northwest side of the cone (Figs.2.10, 5.6) and are abundant as xenolith cored bombs in the pyroclastic deposits making up the cone.

Small crustal fragments (up to 5 cm) and pyroxene megacrysts (up to 3 cm) are common as inclusions in scoria cone forming pyroclastic deposits (e.g. Units *58b, c, k*) and in lava flows (locations 3, 4.B) where crustal xenoliths up to 20 cm in size were found (Fig.5.4). Crustal xenoliths are large and abundant in the deposits containing mantle xenoliths on Scoria Cone 4. Crustal xenoliths of granite, granulite, gabbro and diorite have been identified.

Fig.5.4: Granulite xenolith in outcrop at Locality 4.B.

Fig.5.5: Black pyroxene megacryst in outcrop at Locality 75. (Length of penknife ≈ 10 cm)

Fig.5.6: Xenolith rich outcrop at Locality 74. (Length of penknife ≈ 10 cm)

Twelve xenolith types were sampled, representative of the abundant xenoliths present in the basanitic dike at Locality 74 (Figs. 2.10, 5.6). The host basanite of these xenoliths is classified as a primitive basanite.

5.4 XENOLITH PETROLOGY

5.4.1 ULTRAMAFIC XENOLITHS

The ultramafic xenoliths analysed have been classified using an olivine-orthopyroxene-clinopyroxene ternary classification diagram (Fig.5.7) of point-counted modal analyses (Table 5.1). Three classes of peridotite xenolith occur; dunite, harzburgite and lherzolite. Pyroxenite xenoliths found are olivine websterite and websterite. Both the peridotite and pyroxenite xenoliths are thought to be Type I (Cr-diopside series) xenoliths in the classification system of Frey and Prinz *(1978)* due to the absence of kaersutite.

Table 5.1: Model mineralogy of xenoliths determined by point counts.

Xenolith type	Peridotite				
	Harzburgite	Lherzolite		Dunite	
Sample	V	VIII	IX	X	XI
Olivine	67.9	44.5	52.0	88.2	47.6
Orthopx.	15.2	7.8	12.0	2.7	-
Clinopx.	1.8	37.2	18.5	-	-
Spinel	4.3	-	7.3	2.5	-
Opaque	-	7.0	0.3	-	47.0
Vesic.	10.8	3.5	10.0	6.7	6.4
Feldspar	-	rare	-	-	-
Quartz	-	-	-	-	-
Calcite	-	-	-	-	-
Glass	-	-	-	-	-
Count	600	600	600	600	600

Xenolith type	Pyroxenite			Crustal		
	Ol. Websterite		Websterite	Granulite	Granulite	Granite
Sample	I	IV	II	III	VI	VII
Olivine	16.5	19.8		-	-	-
Orthopx.	40.3	25.1	29.8	-	-	-
Clinopx.	29.2	44.4	52.5	48.5	42.3	-
Spinel	4.0	-	-		-	-
Opaque	-	1.0	-	18.8	13.0	-
Vesic.	6.7	9.0	17.8	8.0	5.8	10.7
Feldspar	rare	<0.1	-	9.0	17.0	18.7
Quartz	3.3	-	-	15.0	21.8	46.5
Calcite	-	-	-	0.7	-	-
Glass	-	-	-	-	-	24.7
Count	600	600	400	600	600	600

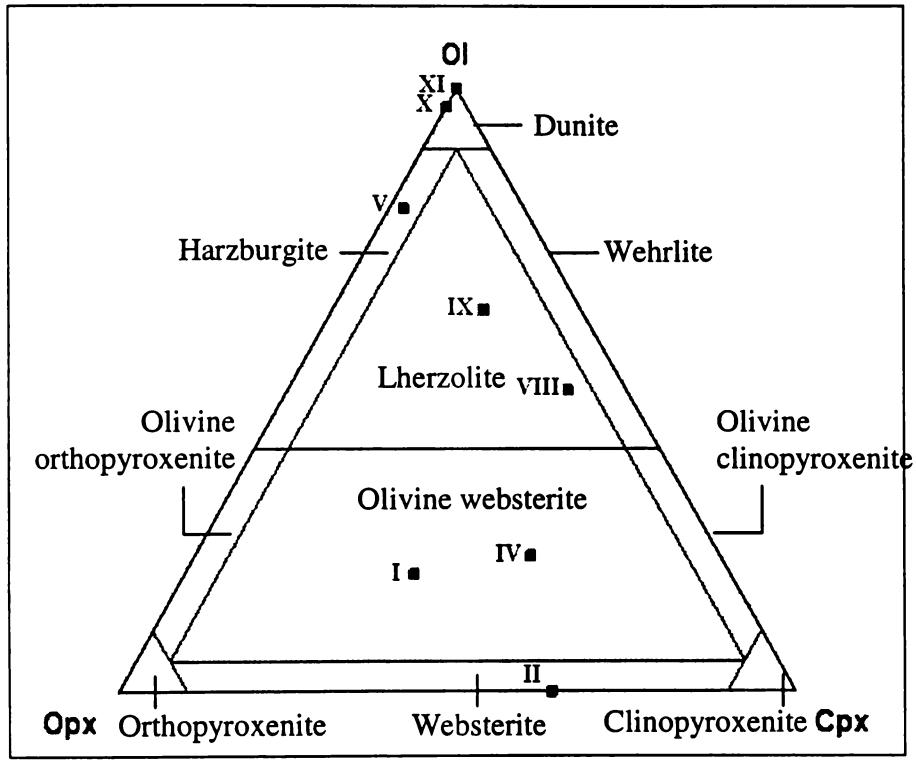

Fig.5.7: Classification of ultramafic xenoliths.

5.4.1a DUNITE

Xenoliths X and XI appear very different but both are classified as dunite because they contain abundant olivine but very little pyroxene (Fig. 5.8).

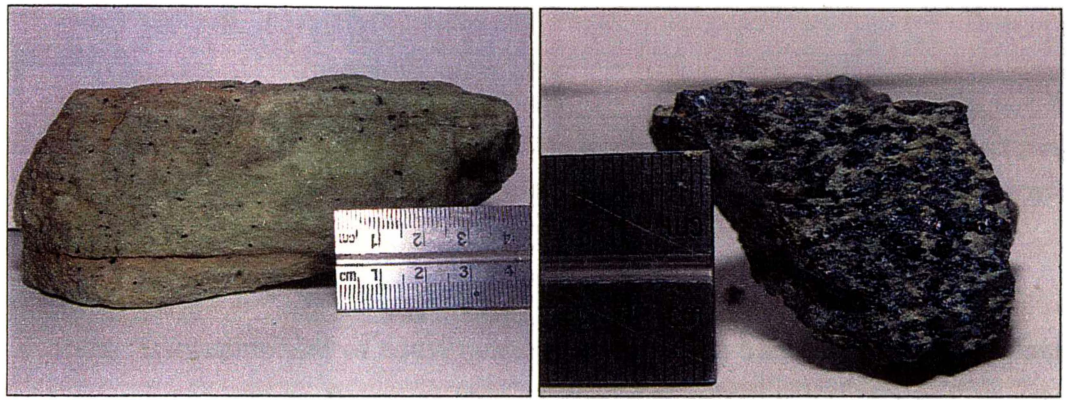

Fig.5.8: Dunite xenoliths X and XI

Xenolith X is pale yellow green in colour, fine grained (<10 mm), with occasional black orthopyroxene crystals up to 1.5 mm in size. This sample shows a foliation in hand specimen, in thin section this foliation is seen to be defined by grain size variations. Coarse (0.5-1.0 mm) and fine (0.1-0.3 mm) grained layers of equant, equigranular olivine crystals alternate and make up the majority (88 %) of this xenolith. Orthopyroxene occurs as rare (< 3 %) pale brown crystals up to 1.5 mm in size. Spinel is also rare (2.5 %) and occurs as dark brown anhedral inclusions up to 1 mm in size, these are probably chromite.

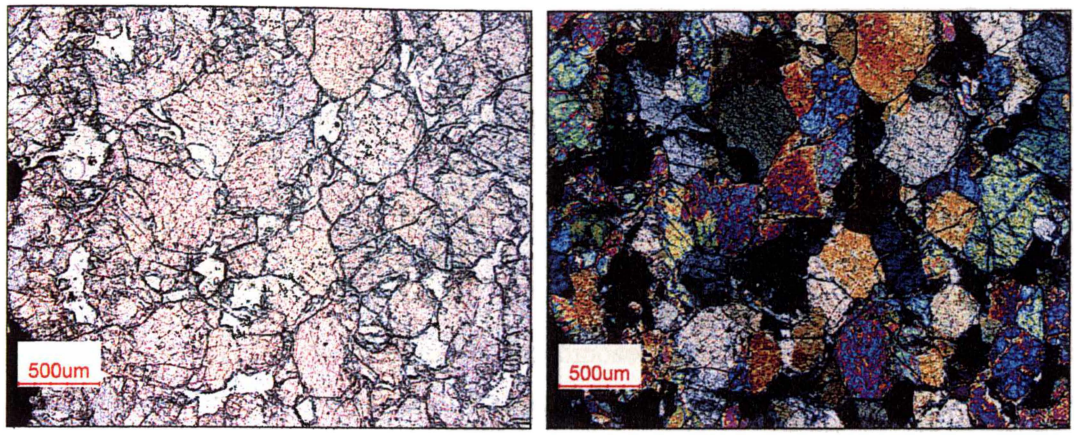

Fig.5.9: Coarse grained section of dunite (X) in plane polarised *(a)* and crossed polarized *(b)* light.

Xenolith XI is composed of equal proportions of a dark blue-black lustrous mineral and very pale yellow olivine. In thin section this xenolith has a porphyroclastic texture of larger (8 mm) opaque crystals in a matrix of finer (0.25-1.5 mm) equant olivine crystals. The opaque mineral is probably chromite or magnetite, these opaque crystals are anhedral with irregular edges, and most show elongation and alignment in a consistent direction.

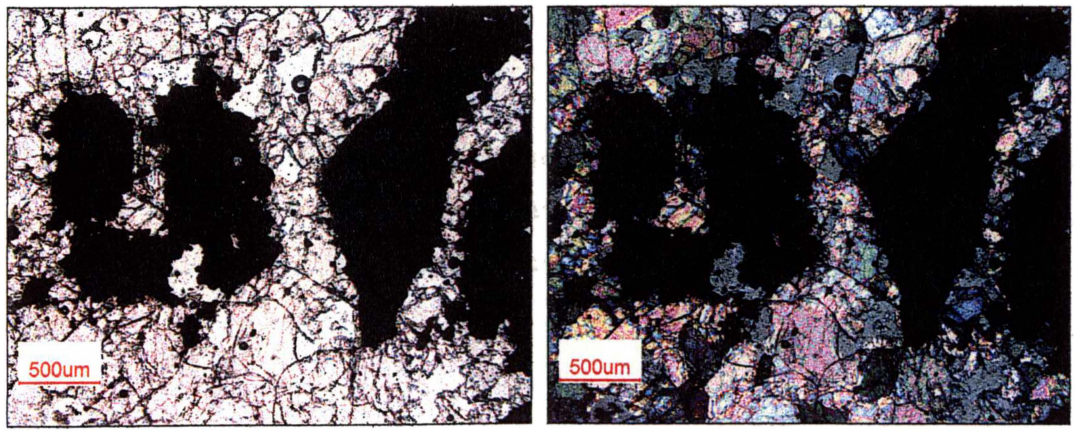

Fig.5.10: Dunite (XI) in plane polarised *(a)* and crossed polarised *(b)* light.

The shear textures in these dunite xenoliths indicate that they underwent a time of differential stress shortly before their entrainment into their host magma (*Pearson et al., 2004*).

5.4.1b HARZBURGITE

Xenolith V is classified as harzburgite, is composed dominantly of olivine (68 %) and orthopyroxene (15 %) with minor clinopyroxene (4 %) and spinel (2 %). In hand specimen (Fig.5.11) this xenolith is pale yellow green with dark pyroxene crystals defining coarse layering.

Fig.5.11: Harzburgite xenolith (V)

The xenolith has a porphyroclastic texture with large (up to 5 mm) orthopyroxene crystals in a fine grained (0.2–0.5 mm) matrix of olivine. Occasional larger (to 2 mm) olivines are rare. Some clinopyroxene crystals show exsolution textures.

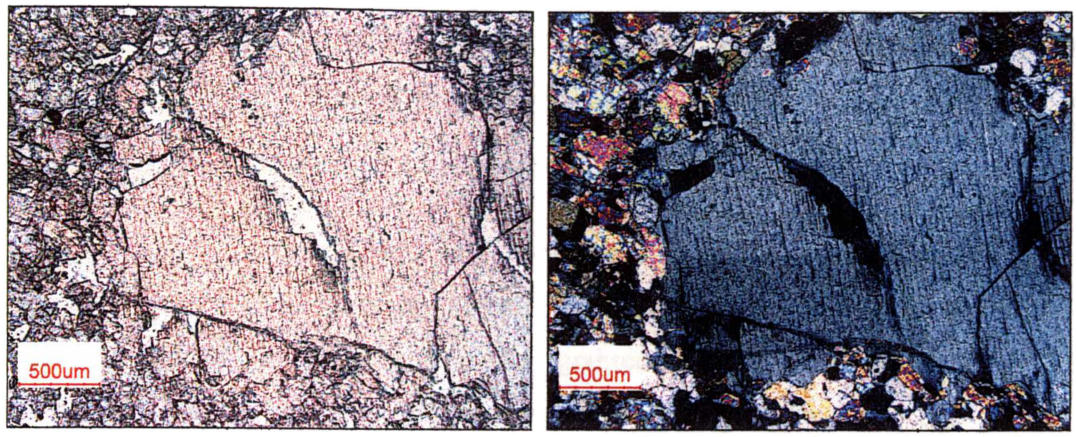

Fig.5.12: Harzburgite xenolith showing porphyroclastic texture in plane polarised *(a)* and crossed polarised *(b)* light. A large clinopyroxene crystal showing exsolution textures is found in a matrix of small olivine grains.

5.4.1c LHERZOLITE

Xenoliths VIII and IX are classified as lherzolite, they are composed dominantly of olivine (44 – 52 %) with lesser amounts of clinopyroxene (18–37 %), orthopyroxene (8–12 %) and opaque oxides (0.3–7 %).

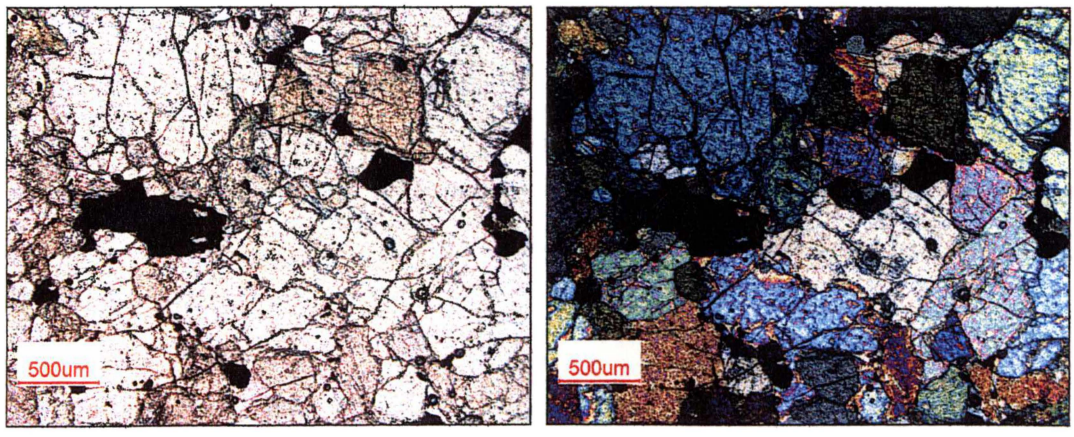

Fig.5.13: Fine grained lherzolite (sample VIII) in plane polarised *(a)* and crossed polarised *(b)* light.

Xenolith VIII is fine grained, (typically <1.5 mm) with equigranular, polygonal grains of olivine, clinopyroxene, orthopyroxene and opaque oxides. Rare (<1 %) feldspar occurs.

Xenolith IX is coarse grained and dark green in colour. This xenolith has a porphyroclastic texture with large crystals of clinopyroxene (<6 mm), orthopyroxene (<4 mm) and olivine (<3 mm), in a finer grained (0.1–0.75 mm) matrix of olivine. Spinel occurs as intergranular infillings, some up to 3 mm in size (Fig.5.14).

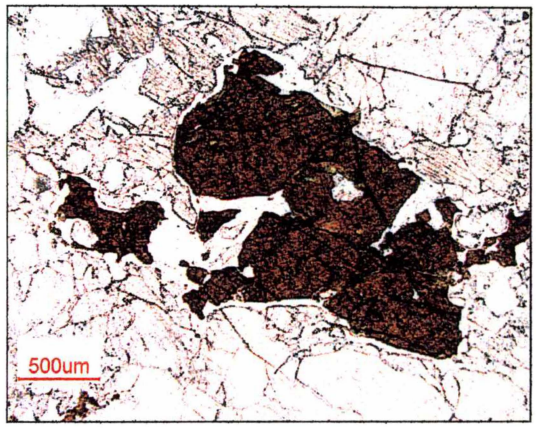

Fig.5.14: Spinel in lherzolite xenolith IX

5.4.1d OLIVINE WEBSTERITE

Xenoliths I and IV contain abundant pyroxene (69 % total pyroxenes) with lesser amount of olivine (16–20 %) and are classified as olivine websterite. Feldspar is rare in both samples (<3 %).

Xenolith I is coarse grained (pyroxene up to 5 mm, olivine to 2.5 mm) and composed of orthopyroxene (40 %), clinopyroxene (29 %), olivine (16 %), with rare (<4 %) spinel.

Xenolith IV is coarse grained (1–3 mm) with an equigranular texture and is composed of clinopyroxene (44 %), orthopyroxene (25 %), and olivine (20 %) with rare opaque oxides (1 %).

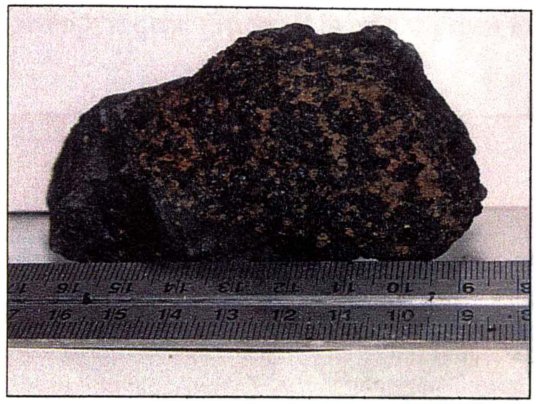

Fig.5.15: Olivine websterite xenolith (IV).

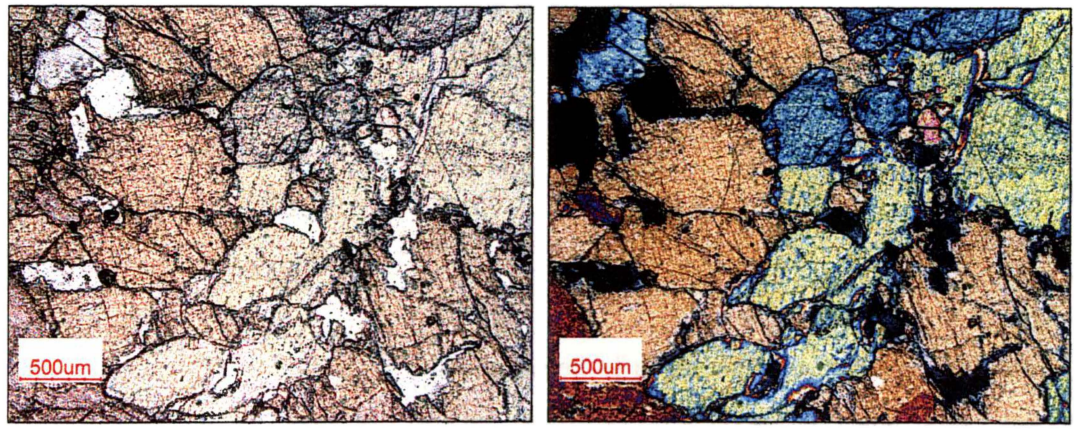

Fig.5.16: Coarse grained olivine websterite (xenolith IV) in plane polarised *(a)* and crossed polarised *(b)* light.

5.4.1e WEBSTERITE

Xenolith II is classified as websterite, and is composed entirely of fine grained (to 0.75 mm), equigranular pyroxene with clinopyroxene (64 %) more abundant than orthopyroxene (36 %) It is bright green in hand specimen.

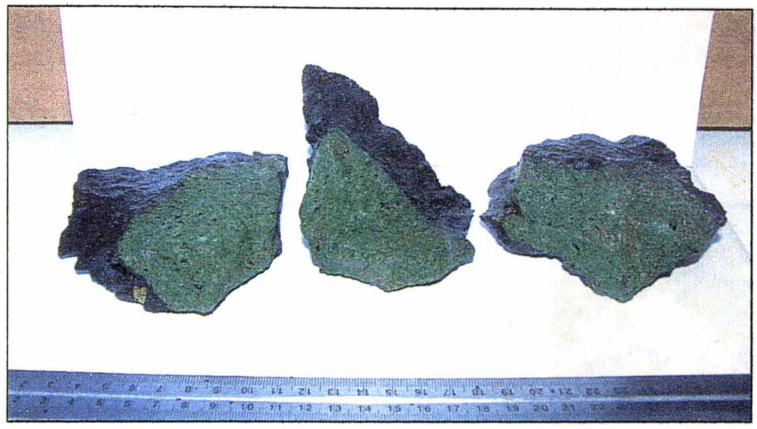

Fig.5.17: Bright green websterite xenoliths (xenolith II).

5.4.2 CRUSTAL XENOLITHS

5.4.2a GRANULITE

Granulite xenoliths III and VI are composed of abundant clinopyroxene (42-49 %), with lesser quartz (15-22 %), opaque oxides (13-19 %) and feldspar (9-17 %). In hand specimen both show a foliated texture of layered dark pyroxene and light quartz and feldspar. These xenoliths are fine grained with typical grain sizes of less than 1 mm.

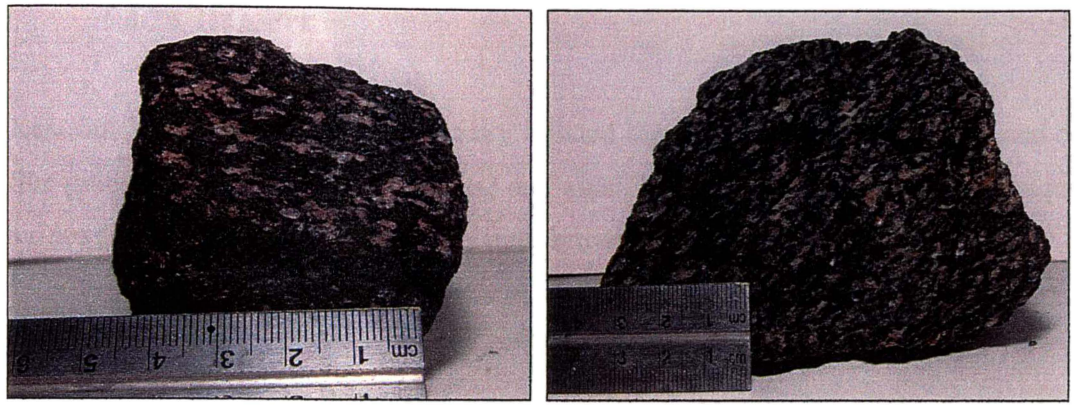

Fig.5.18: Granulite xenoliths III *(a)* and VI *(b)*.

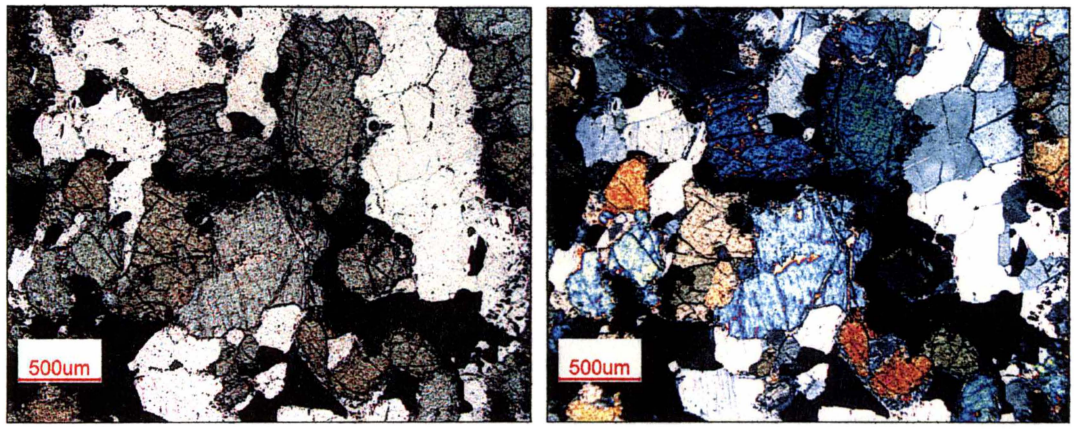

Fig.5.19: Granulite in plane polarised *(a)* and crossed polarised *(b)* light.

5.4.2b GRANITE

Xenolith VII is pale grey with a streaky foliated texture (Fig.5.20). It is composed of fine grained quartz (47 %), plagioclase and alkali feldspar, (19 %) and minor opaque oxides (<2 %) with glass occurring as dark brown spiky growths between grains.

Fig.5.20: Granite xenolith (VII)

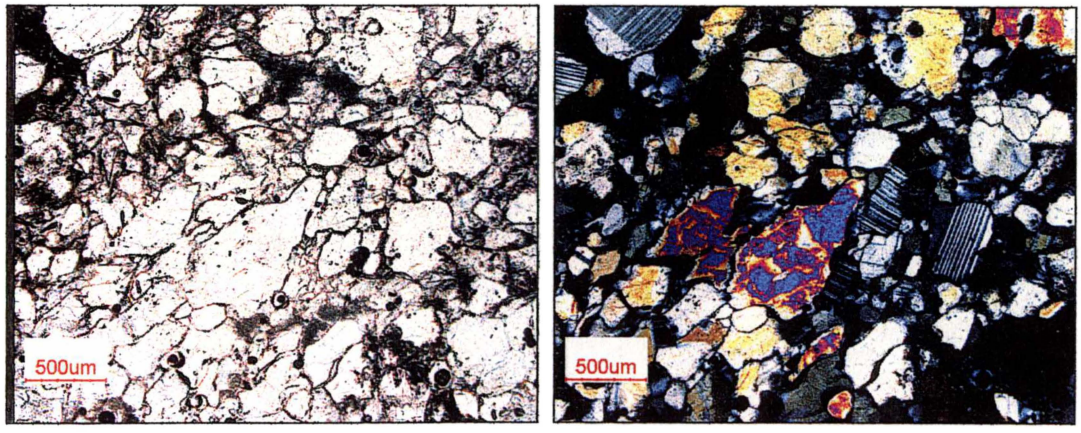

Fig.5.21: Granite (VII) in plane polarised *(a)* and crossed polarised *(b)* light.

CHAPTER SIX DISCUSSION AND INTERPRETATION

6.1 PHYSICAL VOLCANOLOGY

All four scoria cones found in the field area were formed by hawaiian or strombolian style fire fountaining eruptions of basaltic lava. This is shown by the low amounts of fragmentation and small dispersal of clasts from the vent. The typical clasts in these deposits are fine lapilli to small bombs. These are no widespread fine ash deposits present, excluding the possibility of more explosive phreatic or phreatomagmatic eruptions, due to magmatic interaction with ground or surface water. Due to the eroded nature of these cones their full extent and clast dispersal is not known, however they appear to have dispersal distances of up to approximately a kilometer and with deposits covering areas of several square kilometers.

6.1.1 ERUPTIVE PROCESSES

Strombolian and hawaiian style eruptions are one of the least explosive of all volcanic eruptions. Their low intensity and dispersive power is due to the low viscosity of the magma involved, usually basalt or basaltic andesite, and the generally small magma volumes involved. Magmatic gases can easily segregate and escape from the magma relatively slowly compared to the highly viscous magmas involved in more explosive plinian style eruptions (*Vergniolle and Mangan, 2000*). Figure 6.1 compares the explosiveness of eruption styles. Hawaiian and strombolian style eruptions have very low fragmentation, eruption height and dispersal distance of deposit.

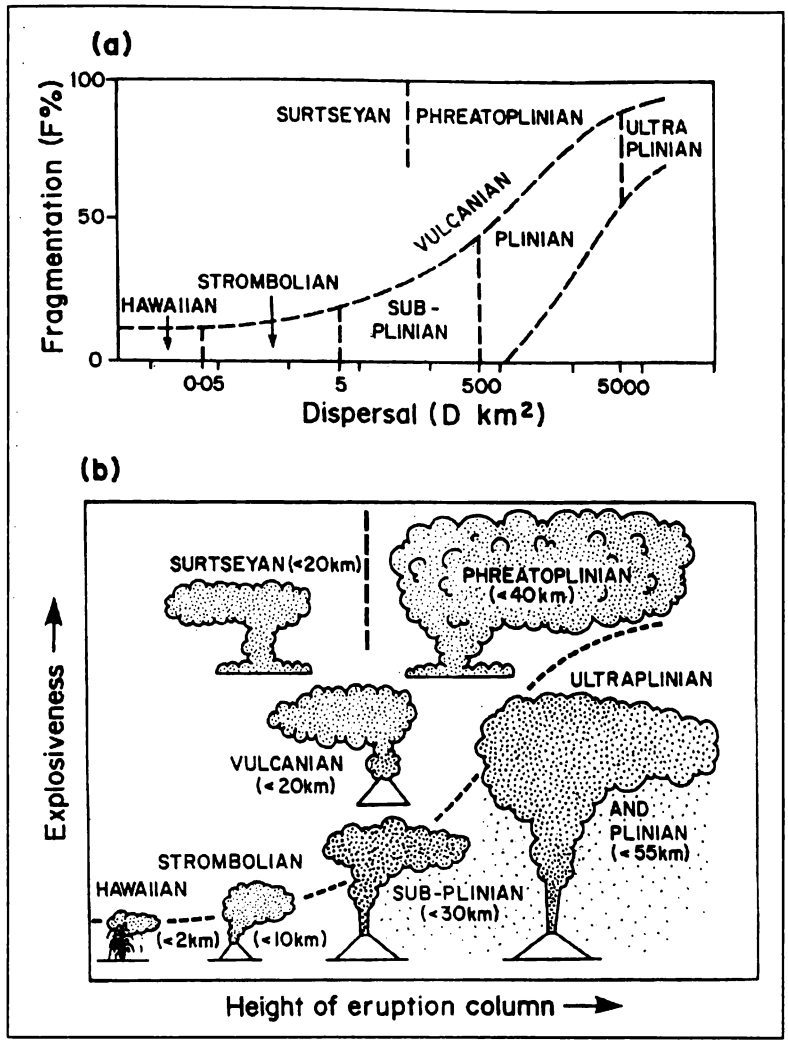

Fig.6.1: Comparison of eruption explosiveness between several eruption styles (*Cas and Wright, 1987*).

Both hawaiian and strombolian style eruptions cause the ejection of molten magma fragments carried by gas. The main difference between the two eruption styles is that hawaiian eruptions occur as sustained fire fountains while strombolian eruptions are much shorter, occurring as discrete showers of lava fragments. There is a continuum between these eruption styles and an eruption may change from one style to the other (*Vergniolle and Mangan, 2000*).

Hawaiian eruptions may begin with an elongate fissure vent, creating a long fountain or 'curtain of fire' that may be several kilometers long. An example of this is the 1 km fissure formed during the eruption of Kilauea, 1983. Over the

hours or days following the initial eruption the vent becomes restricted as parts of the fissure become sealed off. The fountaining becomes constricted to single points and eventually a single vent (*Vergniolle and Mangan, 2000*).

The fountain's structure is a sustained gas jet ejecting centimeter to meter sized molten lava blobs near vertically at velocities of 100 ms^{-1} to heights of 100-500 meters. The highest observed fountains were those of the Izu-Oshima, Japan eruption of 1986-87, where the fountain reached a height of 1600 m. Temperatures inside the fire fountain are hottest in the centre, where they have been reported at 1150-1216 °C. The magma:gas ratio averaged over the eruption is around 70:1 (*Vergniolle and Mangan, 2000*).

Hawaiian style fire fountaining is usually continuous for several hours at a time, although there are more intense pulses at 1-5 second intervals. For example the Kilauea, 1959, eruption had 16 fountaining episodes lasting between 2 and 32 hours each, spread over 4 weeks (*Vergniolle and Mangan, 2000*). There is often a change to effusive activity following a long period of explosive fire fountaining. For example one eruption of Kilauea volcano, Hawaii, began in 1983 and episodes of fire fountaining continued for three years, these were then replaced by lava effusion which has continued until the present day (*Vergniolle and Mangan 2000*).

Strombolian eruptions begin with either a hawaiian style eruption or a more explosive explosion clearing the vent of rock. The magma is often of a higher viscosity than that in Hawaiian eruptions; because of cooler temperatures (1080 °C measured at Etna) and more siliceous magma, usually basaltic andesite. (*Vergniolle and Mangan, 2000*). Gas is separated from the magma and rises and accumulates as a bubble in the conduit, forming a large blister at the surface of the stagnant magma column or lava lake. This bubble swells to several metres in diameter and explodes, expelling the gas and carrying the fragmented bubble lid with it. Gas release is more episodic compared to the sustained fountaining of

hawaiian style eruptions. For example Stromboli volcano erupts semi-regularly 3-5 times per hour. This causes higher gas pressures, more intense eruptions and higher fragmentation of the magma (*Vergniolle and Mangan, 2000*). Gas and magma fragments are ejected at angles of 45-75°, at velocities of 40-100 ms^{-1}, and to heights of greater than 100 m. Strombolian eruptions have a much higher magma:gas ratio of 10^5:1. Because of the more explosive nature of strombolian eruptions the clasts have a finer grain size causing them to cool more rapidly and often land as solidified scoria clasts (*Vergniolle and Mangan, 2000*).

The differences in the gas flow regimes between hawaiian and strombolian style volcanic activity can be seen in the two-phase gas flow models in Figure 6.2. At gas contents of around less than 30 % the magma contains small gas bubbles in suspension and forms effusive lava flows. At gas contents of around 70 % bubbles may coalesce to form gas pockets in the conduit, this regime causes strombolian activity. At gas contents greater than 70 % fire fountaining will result. The gas flow regime can either be annular, where the magma lies on the conduit walls and a gas jet moves up the centre, or dispersed, where the magma is fragmented and carried to the surface in a stream of gas (*Vergniolle and Mangan, 2000*).

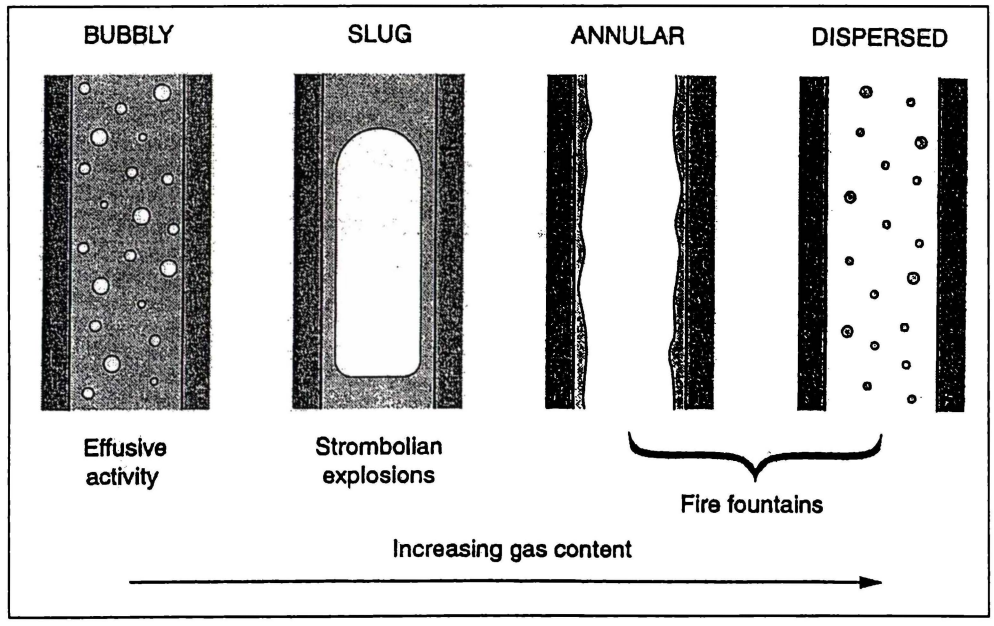

Fig.6.2: Different types of two-phase gas flows and the eruption styles caused by each of these (*Vergniolle and Mangan, 2000*)

6.1.2 ERUPTIVE PRODUCTS

Spatter cones and welded or agglutinated deposits are commonly formed by hawaiian style lava fountaining, while loose non-welded cinder cones are formed by strombolian style eruptions because many clasts are cool on landing *(Vergniolle and Mangan, 2000).*

Scoria cones are one of the most common volcanic features found on land. They form by the subaerial eruption of low viscosity magma, usually basaltic in composition. Scoria cones are formed by the deposits of 'dry' strombolian or hawaiian style eruptions (*Vespermann and Schmincke, 2000*). Figure 6.3 shows the volcanic deposits that result from differing water to magma ratios. If water is involved the eruption is much more violent and a tuff ring is formed. 'Dry' magmatic eruptions produce deposits with coarse grain sizes, massive to coarse bedding, few lithics and high temperature deposits. In contrast 'wet' hydroclastic (or phreatomagmatic) deposits are finer grained, often contain fine layering and cross-bedding, and are very lithic rich, up to 90 % by weight (*Vespermann and Schmincke, 2000*).

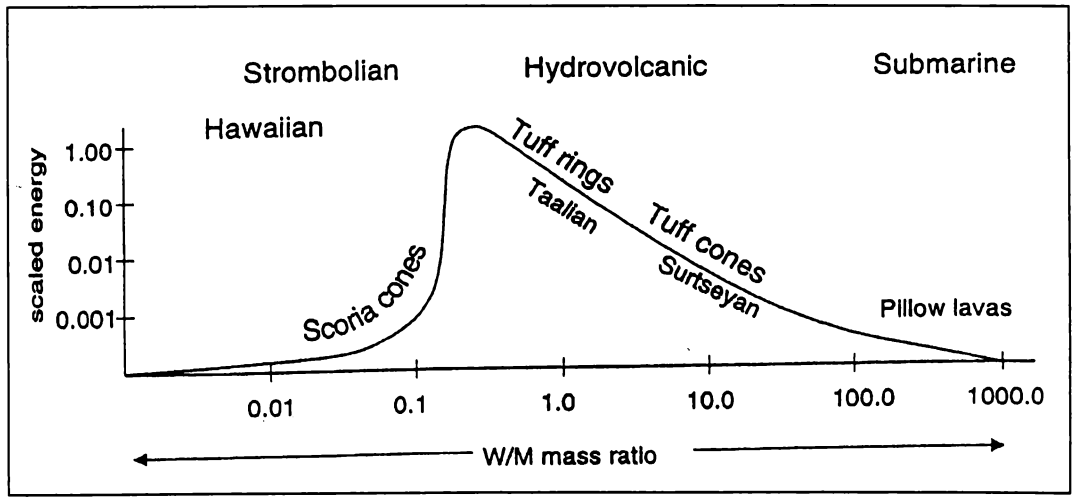

Fig.6.3: The influence of water on eruption style, energy released and deposit type. (*Vespermann and Schmincke, 2000*)

Scoria cones often occur clustered together in volcanic fields that may contain hundreds of monogenetic eruption centers, such as the Eiffel Volcanic Field in Germany and the Trans-Mexican Volcanic Belt in Mexico (*Connor and Conway, 2000*). They are often aligned along zones of stress such as faults and are also common on the flanks of larger composite or shield volcanoes and in calderas (*Connor and Conway, 2000*).

Scoria cones form quickly from deposits of strombolian and hawaiian style eruptions, most commonly lava bombs, scoria, welded lava spatter and occasional ash. (*Vespermann and Schmincke, 2000*). Scoria cones can grow very rapidly, for example; the Paricutin, Mexico scoria cone grew 35 m in one day and reached 167 m in height after one week of activity (*Vespermann and Schmincke, 2000*). Half of all observed scoria cone forming eruptions lasted less than 30 days and the vast majority (95 %) ended in less than one year (*Vespermann and Schmincke, 2000*).

There are two main facies found in scoria cone deposits; an inner crater facies and an outer wall facies (Fig.6.4). The crater facies are relatively heterogeneous and consist of agglutinated lava spatter overlain by lava bombs in a lapilli matrix (*Vespermann and Schmincke, 2000*). The wall facies mainly consists of scoria bombs and lapilli, the welding, compaction and grain size of these deposits decreases with distance traveled away from the vent (*Vespermann and Schmincke, 2000*). If the eruption began with an explosive vent clearing explosion the lowest lying wall deposits may be ash and lithic rich breccias. Reworking of deposits is common, especially on steep slopes where debris and grain flows may occur. These can be seen as inversely graded beds (*Vespermann and Schmincke, 2000*).

Syn-eruptive grain flows were reported on the outer walls during the formation of the Laghetto scoria cone on the upper slopes of Etna during the summer of 2001 *(Calvari and Pinkerton, 2004).*

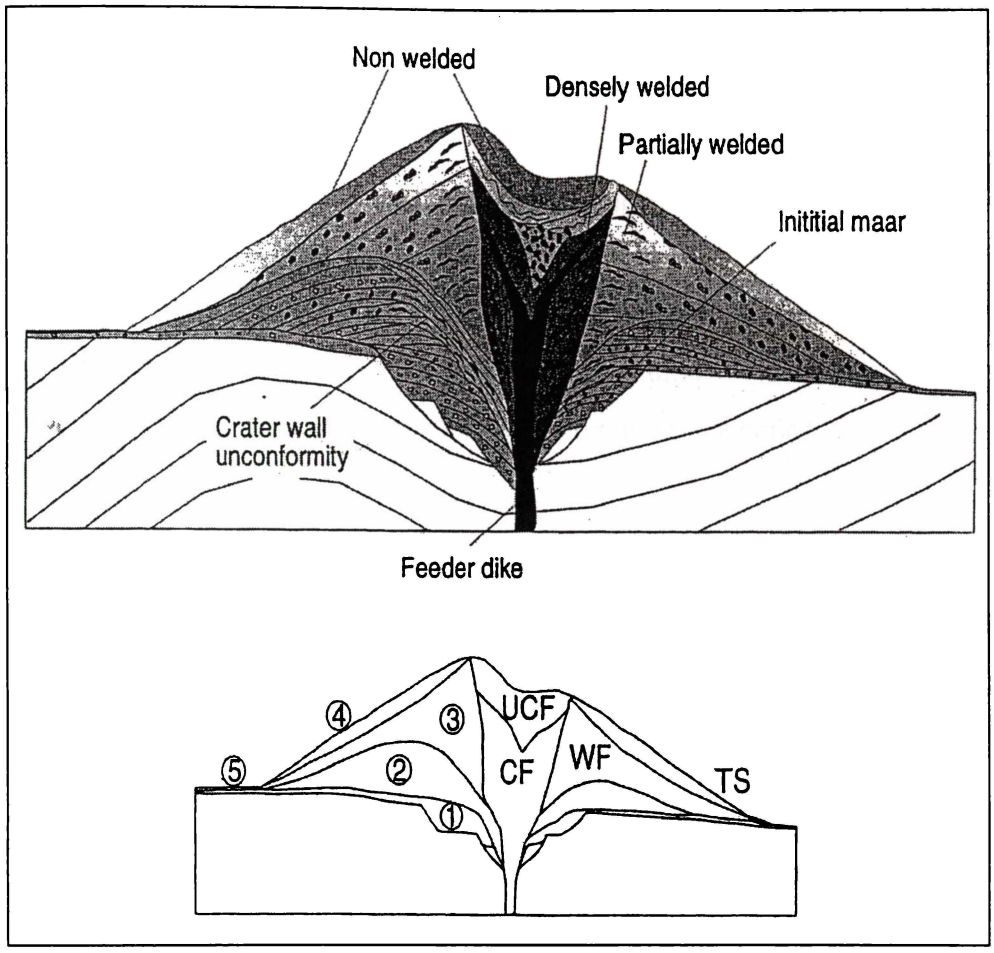

Fig.6.4: Morphology and internal structure of a scoria cone. CF (crater facies), UCF (upper crater facies), WF (wall facies), TS (talus slope), 1. initial phreatomagmatic eruptions, 2. & 3. main strombolian cone building deposits, 4. post-eruption talus slides, 5. distal fallout (*Vespermann and Schmincke, 2000*).

The main factors influencing the morphology of a scoria cone are;

- total volume of material erupted
- range and ejection velocity of ejected material
- ejection angle
- wind speed and direction
- particle size
- lava overflows
- vent geometry
- presence of surface or groundwater

At least three sequences of pyroclastic units make up Scoria Cones 1 and 2, determined by changes in dip direction of the units and unconformities seen. These sequences are;

- The N/NW dipping sequence on the northwestern side of scoria cone 1 consisting of Unit 34 and Units 33*a-n*.
- The E to NE dipping sequence making up the remainder of scoria cone 1, Unit 33*m* and the units of stratigraphic columns 37, 38 and 58.
- The S to SW dipping sequence making up scoria cone 2.

Each of these sequences is thought to have originated from a different vent location. The N/NW dipping sequence requires a vent location to the southeast, and Scoria Cone 3 is a possible origin for these deposits, it is found approximately 1 km to the east. The E/NE dipping sequence requires a vent location to the west or southwest, and the breccia deposits to the southwest at locations 116-120 may mark the vent location of these deposits. The S/SW dipping sequence requires a vent position to the north or northeast. This vent has possibly been eroded or covered during the later deposition of the sequence of E/NE dipping pyroclastic units forming the southern end of Scoria Cone 1.

Angular unconformities between each of these sequences indicate different vent locations and a time and erosional gap between the deposition of each. The E/NE dipping deposits making up the southern end of scoria cone 1 are the youngest of these three sequences as they unconformably overlie both the N/NW and S/SW dipping deposits.

The slope angle of young scoria cones is usually ~30-33° , the angle of repose of loose particles, but can be steeper in more cohesive welded deposits (*Vespermann and Schmincke, 2000*). Pyroclastic units measured in the field area typically had slope angles of 15 to 35 degrees. Large scale deformation and slumping was seen at several locations in the deposits of Scoria Cones 1 and 4. The low dip angle of many deposits may indicate that they mantle an existing feature. Figure 6.5 shows

the pyroclastic sequence described in stratigraphic column 58. The upper units lie nearly horizontally but increase in steepness towards the left of the picture. The units in this sequence overlie those of scoria cone 2 and may be mantling this earlier scoria cone.

Fig.6.5: Part of the pyroclastic sequence described in stratigraphic column 58 of Scoria cone 1.

Lava flows usually extrude once explosive activity has ceased and are often oriented along zones of weakness, faults or stress fields *(Vespermann and Schmincke, 2000).* Small lava domes are the only evidence of any effusive activity related to these scoria cones. Many similar scoria cones nearby on Hurricane Ridge have pahoehoe type lava flows originating in craters and on flanks of cones. The two thick a'a' type lava flows occurring in the field area (Loc. 3, 4) do not appear linked to any scoria cone deposits.

6.1.3 Facies Description and Interpretation

The units of scoria cones 1 and 2 described and drawn in the five stratigraphic columns can be grouped into three facies distinguished by their physical characteristics, such as grain size, sorting and grading, and degree of welding. These represent near-vent, medial and outer flank deposits.

6.1.3a Outer Flank Facies

Several reversely graded units occur, all in section 33. These units are characterised by reverse grading of clasts from a fine grained base into a coarse upper (e.g. Fig 6.6). This grading is especially prominent in units 33*c, e, f* and units 33*h* and *i* have fine grained basal layers (Fig. 2.16) and also show less well defined reverse grading.

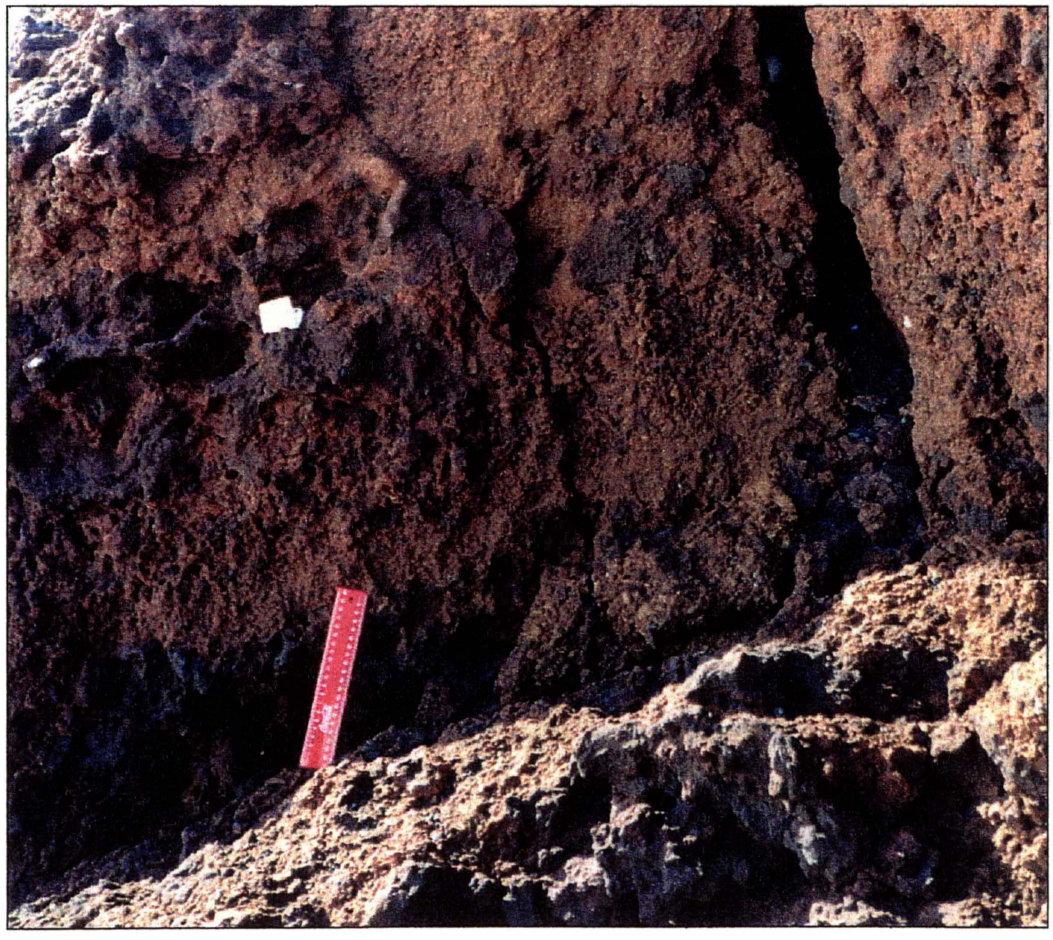

Fig.6.6: The reversely graded unit 33*e*.

These are thought to be formed by syn-eruptive granular flows of scoriaceous lapilli and ash, probably on the outer flanks of the cone. Some of these units are partially to densely welded and contain deformed clasts indicating that collapse and flow must have taken place while the deposit was still hot and plastic.

6.1.3B MEDIAL FACIES

These deposits are massive or coarsely bedded and partially welded, they are common in the stratigraphic columns at locations 33 (units 33*j, l, m*), 37 (Units 37*a, d, f, i, j, l*) and 38 (units 38*q, r, s, t, u*). Units such as 37*l* are typical of this type of deposit, it is a thick, weakly to moderately welded crudely bedded unit with bedding defined by small variations in the grain size and degree of welding, as well as occasional bomb rich layers, finer grained layers and more densely welded deformed streaky layers (Fig.2.20, 21). Few clasts have fluidal surface textures or show deformation, indicating moderately intense activity. Grain size and welding changes are mainly due to variations in eruptive intensity as the deposit was being formed. These deposits were the result of less intense activity than the densely to extremely welded units described below. This may because they are found further from the vent location, were deposited at cooler temperatures or at a slower rate of accumulation. The thin agglutinate beds and bomb rich horizons scattered through these units formed by short periods of more intense activity.

6.1.3C NEAR VENT FACIES

These facies represent deposits formed near to the vent, they are made up of two distinct alternating deposit types, thick densely-extremely welded units with coalesced agglutinate beds and thin partially welded spatter deposits, typically bright red in colour.

Bright red, partially to densely welded spatter deposits are common in the deposits of Scoria Cone 1 at locations 38 (units 38*r, s, t, u*) and 58 (units 58*f, i*),

and Scoria Cone 2 at location 59 (units 59*j, f, d,* and thin beds included in units 59*k, e*). These bright red spatter units are characterised by a fine grain size (typically <50 mm), fluidal clast textures and the rarity of larger bombs and blocks (Fig.6.7).

These units were formed by short bursts of intense activity, causing high clast fragmentation and fine grain sizes. The porous 'tack welded' nature of many the fluidal textured clasts in these deposits indicates high temperatures, but the lack of any agglutination suggests a slower accumulation rate with less weight to compact the deposit and cause dense welding. Because these spatter deposits alternate with agglutinate units (6.1.3D), they may have been formed by more intense activity during sustained fire fountaining or during less continuous periods of activity.

Fig.6.7: A typical example of a bright red, partially welded spatter unit.

Deformed agglutinate and coalesced spatter beds are common in column 58 (units 58*b, c, d, e, k*) of scoria cone 1 and column 59 (units 59*a, b, i, l*) of Scoria Cone 2. These have an extremely welded and completely coalesced agglutinate core

indistinguishable from a massive, jointed flow of olivine rich basanite. These agglutinate cores are up to 1.5 m thick (e.g. unit 59*a*) but are generally thin (15-50 cm) and occur as beds near the top of densely welded grey pyroclastic units. Above and below the core these grade into highly deformed streaky or swirly patterned agglutinate with some visible clast outlines (Figs.6.8, 2.30) and above and below this into rubbly textured agglutinate with all most clast outlines visible and little flattening of clasts. These deposits formed during very intense, sustained fire fountaining eruptions with high clast temperatures and a rapid accumulation rate.

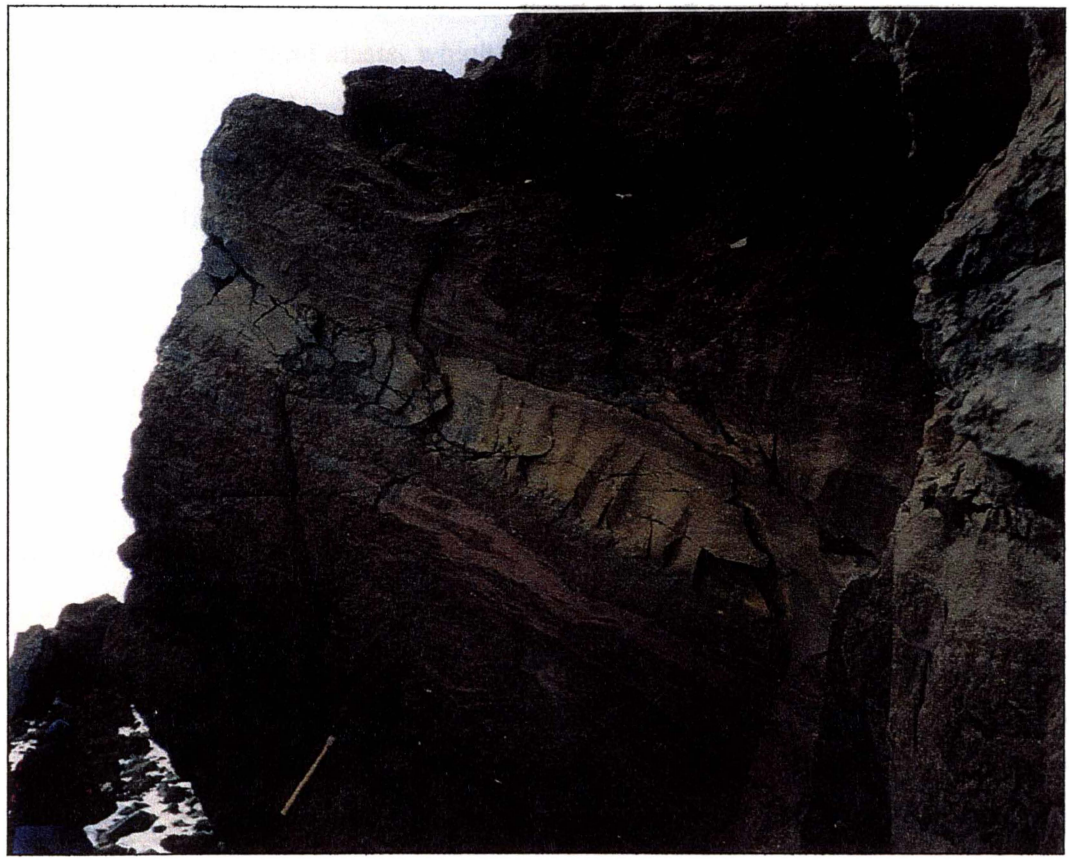

Fig.6.8: Agglutinate deposit showing varying degrees of deformation a completely coalesced core grades out into highly deformed 'streaky' agglutinate.

Sumner (*1998*) investigated flows and discontinuous beds of deformed agglutinate and coalesced spatter at Izu-Oshima, Japan. She identified four textures within the flows, in order of increasing deformation these are;

1. Agglutinate, in which spatter is only moderately flattened and complete clast outlines are preserved
2. Deformed agglutinate, where clasts show extreme flattening but where complete clast outlines are still retained.
3. Highly deformed agglutinate, where >50 % of individual clast outlines are preserved and spatter is deformed into swirling shapes.
4. Coalesced spatter, which shows patchy vesiculation but no unequivocal clast outlines.

Agglutinated scoria beds and clastogenic lavas are common deposits formed by fire fountaining eruptions. They are formed by the rapid accumulation and coalescence of hot, fluid clasts, which occurs most often in hawaiian eruptions of basaltic magma (*Wolff and Sumner, 2000*). Clastogenic or fountain fed lava flows have been observed at many active volcanic areas such as Hawaii, Iceland, Reunion and Japan (*Wolff and Sumner, 2000*) and agglutinate beds are found in many scoria cone deposits, e.g. Red Crater, Tongariro (*Bardsley, 2004*). If complete coalescence of the clasts occurs in a clastogenic lava flow it may be indistinguishable from an effusive flow (*Sumner, 1998; Wolff and Sumner, 2000*).

Welding and agglutination are slightly different processes, although the effects of each are very similar. They both cause compaction, increased coherence and a loss of porosity in the deposit. Welding is the postdepositional deformation of hot, plastic magma fragments due to their own weight. The main factor influencing welding is the accumulation rate of clasts. At high accumulation rates hot clasts will be buried before they cool and the whole mass will remain hot and plastic and able to be deformed (*Wolff and Sumner, 2000*). Figure 6.9 shows the relationship between the pyroclast accumulation rate, temperature and the type of pyroclastic deposit formed.

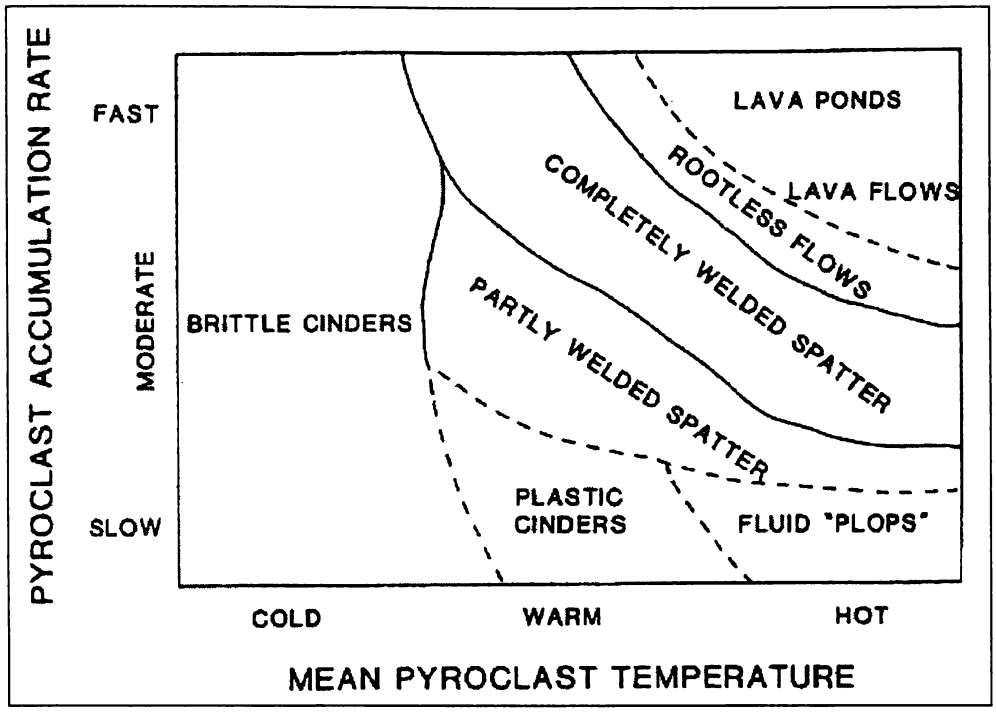

Fig.6.9: Influence of pyroclast accumulation rate and temperature on deposit type (*Head and Wilson, 1989*)

Agglutination is the near instantaneous adhesion and deformation of clasts on deposition due to their kinetic energy (*Wolff and Sumner, 2000*). For agglutination to occur lower viscosities are required than for welding, clasts must be hotter in order to agglutinate (*Wolff and Sumner, 2000*). The main factors influencing agglutination are the magma viscosity and clast size.

6.2 CRYSTAL FRACTIONATION MODELS

Qualitative major element crystal fractionation models for the formation of basanites and trachyte were made by least-squares mass balance methods using the methods of Bryan *et al., (1969)*. Microprobe analyses of crystals from the samples were used. Olivine, clinopyroxene, opaque oxide and plagioclase compositions are from this study (appendix 2.4), amphibole compositions are from Kyle *(1976)* and apatite compositions are stoichometric.

Whole rock major and trace element compositions of rocks were obtained by XRF analysis. Models are based only on the major element chemistry but the fit of the model can be evaluated by calculating the sum of the residuals squared (ΣR^2) and by a comparison of the observed and calculated trace element values.

Trace elements were modelled by applying a simple Rayleigh fractionation process using results from the major element solution. Bulk distribution coefficient values used are those available in M.J. Carr's "IgPet" computer modelling programme.

Kyle *(1979)* emphasises that mass balance calculations are only models and more than one acceptable solution may satisfy a particular fractionation step. In these models fractionation of two different mineral assemblages work equally well for the formation of theoretical daughter compositions close to those observed.

Models with ΣR^2 values of <6 were considered feasible, ideally ΣR^2 values should be as low as possible. Kyle (*1976, 1979, 1981*) developed several crystal fractionation models for rocks of the McMurdo Volcanic Group and these models produced ΣR^2 values of <0.1. The models developed for Mount Morning lavas are inexact but they do provide approximations of possible fractionation assemblages.

Table 6.1: Major element crystal fractionation models for the formation of evolved (3) and high silica basanites (91), and trachyte (95).

Model	Parent→ daughter	Fractionated phases						Total	ΣR^2
		Ol.	Plag.	Amp.	Cpx.	Opq.	Ap.		
1	**21 → 3**	10.12	-	-	31.29	4.77	-	46.18	4.12
2	**21 → 3**	14.34	7.81	-	25.08	3.33	1.18	51.74	3.04
3	**45 → 3**	17.16	14.28	-	8.39	4.05	1.48	45.36	2.76
4	**21 → 91**	12.5	8.51	-	34.96	4.55	0.46	60.98	1.35
5	**45 → 91**	6.87	***3.55***	-	34.11	7.45	***1.27***	43.61	2.77
6	**45 → 91**	11.01	-	-	28.42	7.43	-	48.86	3.33
7	**45 → 95**	21.23	31.2	-	17.47	8.09	2.65	80.64	5.95
8	**3 → 95**	17.16	7.48	-	14.35	7.19	3	59.35	2.35
9	**3 → 95**	-	11.26	35.12	7.07	3.32	1.93	58.7	0.24

(Ol; olivine, Plag; plagioclase, Amp; amphibole, Cpx; clinopyroxene, Opq; opaque oxides, Ap; apatite. Bold italicized values are positive, i.e. cumulates added to the model magma, all others are negative & removals from melt)

Two primitive basanite (21-*low alkali basanite*, 45-*primitive basanite*) compositions were used as parental magmas for modelling the evolution from primitive to more evolved basanites (3-*evolved basanite*, 91-*high silica basanite*). Three possible solutions are given for the formation of each supposed parental composition (Table. 6.1). Two of these (models 1, 6) involve the fractionation of olivine, clinopyroxene and opaque oxides, while the remaining four (models 2, 3, 4, 5) also require fractionation of plagioclase and apatite.

The models show a range of fractionation from 44-61 % and most are dominated by the fractionation of clinopyroxene (25-41 %) and olivine (7-13 %). Model 3 involves the crystallisation of significant olivine (17 %) and plagioclase (14 %) but much less clinopyroxene (8 %).

The largest contribution to the high residuals in these models is made by TiO_2, FeO* and Na_2O. The sodium behaviour is determined by the choice of plagioclase

compositions in the model. Iron and titanium are sensitive to the choice of magmatic composition. Magnetite is a minor but, for these components, significant phase.

The models illustrate that more evolved basanites could have formed by crystal fractionation processes from magmas similar in composition to the primitive basanites found in the field area. The mineral assemblage crystallized was probably olivine, clinopyroxene and opaque oxides, with the possible involvement of plagioclase and apatite.

Models 7, 8 and 9 (Table 6.1) are attempts to produce trachyte (95) compositions by crystal fractionation of primitive basanite (45) and more evolved basanite (3) parent magmas.

Model 7, primitive basanite (45) to trachyte (95), shows high amounts of fractionation (81 %). This model gives a moderately satisfactory result for primitive basanite to trachyte evolution by fractionation of an assemblage of plagioclase, olivine and clinopyroxene with minor opaque oxides and apatite.

Models 8 and 9, evolved basanite to trachyte, show less fractionation (59 %). From a parent of evolved basanite (3) composition two mineral assemblages can be fractionated to give compositions near to trachyte. One of these (model 8) involves the fractionation of mainly olivine, clinopyroxene, plagioclase and opaque oxides, while the other (model 9) involves fractionation of mainly amphibole, plagioclase and clinopyroxene.

There are two main groups of basanite to trachyte crystal fractionation models, those where fractionation dominated by amphibole (models 9) and those where olivine, plagioclase and clinopyroxene are the main fractionated phases (models 7, 8). Models that involve fractionation of olivine, plagioclase and clinopyroxene fit better with the

observed crystal phases in trachyte than those where amphibole is fractionated. Pseudomorphed amphibole is observed as fractionated phase in rocks of the evolved basanite group but not in the high silica basanites or trachyte.

These basanite to trachyte models show it is mathematically possible for the trachyte to have formed by fractional crystallization from magma of composition similar to the basanites found in the field area.

These least-squares mass balance models confirm that rocks of evolved basanite and trachyte compositions could feasibly have been formed by fractional crystallisation of several mineral assemblages from magma of primitive basanite composition. The sum of the residuals squared (ΣR^2) for these models (up to 6) demonstrate only a moderately good fit and they therefore provide only an approximation of possible fractionation pathways. Only one model (model 10) has a ΣR^2 value of <1 (0.24).

6.3 GEOCHEMISTRY DISCUSSION AND CONCLUSIONS

Five petrographic groups have been distinguished on the basis of their major and trace element chemistry;

- Trachyte
- High silica basanite
- Evolved basanite
- Primitive basanite
- Low alkali basanite

Analyses of the primitive, evolved and high silica basanites define an approximately linear trend on major and trace element variation diagrams (Figs. 4.1-4.4), indicating that these rocks are part of a continuous fractionation lineage. The patterns seen in these variation diagrams suggest that the suite of magmas represented by the rocks evolved by crystal fractionation of olivine, clinopyroxene and titanomagnetite, with amphibole, apatite and, to a lesser extent plagioclase also crystallising in the more evolved rocks. Fractionation of feldspar has not been a major factor in the evolution of these rocks because no depletion of europium is seen relative to Sm or Gd (Figs. 4.6, 4.7). Much of the feldspar present may therefore have been sourced from disaggregated crustal xenoliths or have a cumulus origin (*Kyle, 1976*).

Least squares major element crystal fractionation modelling shows that rocks of evolved basanite and trachyte compositions could have been formed by fractional crystallisation from magma of primitive basanite composition. Several fractionated mineral assemblages can account for the transitions modeled, but those that do not involve amphibole fit closest to the observed crystal phases in trachyte.

Kyle (*1979*) suggested a model for the magma evolution in which small pods of primary magma are intruded into upper mantle or crustal magma chambers where

differentiation occurs to form more intermediate compositions (Fig.6.10). Kyle (*1981*) suggested that a number of pods of primary magma fractionating under a range of conditions can account for the highly variable Ni, Cr, Sr, Al_2O_3 and MgO contents in basanites noted by Kyle (*1981*) and also seen in this study (Figs. 4.1, 2, 3). The more strongly fractionated trachytes may have been formed by shallow level fractionation. Kyle (*1979*) developed this model for the Rainbow Ridge eruptive sequence but suggests that it is applicable to most centers in the Erebus Volcanic Province.

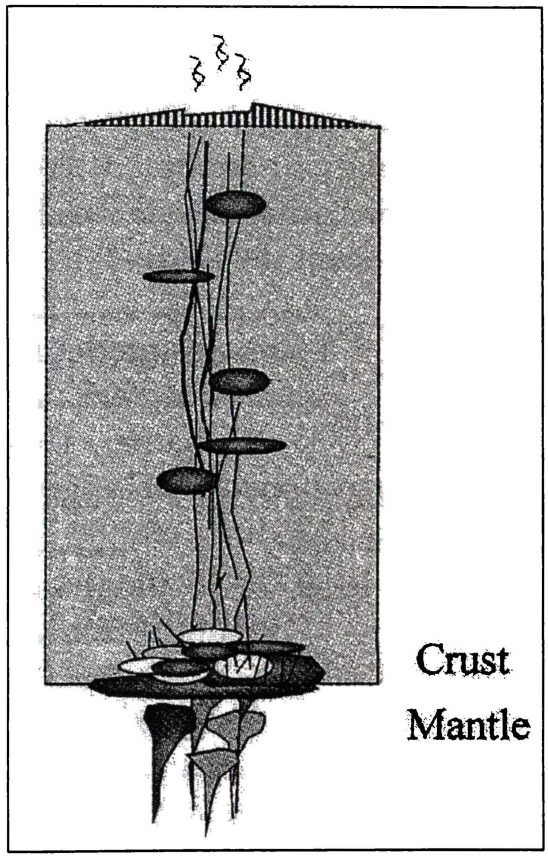

Fig.10: A magma evolution model showing pods of fractionating basanitic magma underplating the crust and distributed throughout the crust. (adapted from *Price et al., 2003*)

Rocks of the low alkali basanite group appear to be unrelated to the other basanites occurring in the field area. This group is petrographically similar to the primitive basanites but can be distinguished geochemically by lower abundances of many incompatible elements, especially the rare earths (e.g. Figs.4.3, 4.4).

The trachyte may be a highly fractionated member of a basanite fractionation sequence. Some of the most evolved members of the Quaternary basanite-phonolite sequence on Mount Morning have slightly trachytic compositions (Fig.3.1) *(Kyle, 1990b)*. This trachyte may also be part of the Miocene subvolcanic complex outcropping on the northeast ends of Hurricane and Riviera ridges. Trachyte from the field area has much higher incompatible trace element ratios than trachyte from the Riviera Ridge subvolcanic complex analysed by Muncy *(1979)*. This indicates that it is derived from a mantle source different from that of either the Miocene trachytes or quaternary basanites.

Table 6.2: Comparison of incompatible trace element compositions of trachyte from this study and a Miocene trachyte from Riviera Ridge.

	Trachyte (95)	**Trachyte** *(Muncy, 1979)*
Zr (ppm)	892	642
Y (ppm)	33	39
Rb (ppm)	65	160
Zr/Y	27.4	16.5
Zr/Rb	13.8	4.0

A comparison of incompatible element ratios between these rocks shows several distinct groups, possibly indicating several different magma sources. Rocks of the low alkali, primitive and evolved basanite groups have similar incompatible element ratios (Table 6.3) and plot on a line passing through the origin in Figures 6.11*a,b,c*. The rocks of the high silica basanite group define two groups, each with different incompatible element ratios. High silica basanites 86.A, 91 and 124 cluster together

at slightly higher values than the other basanites. Sample 118.H, a high silica basanite bomb from the breccia outcrop at locality 118 has lower incompatible element ratios than the other high silica basanites and could have the same mantle source as the low alkali, primitive and evolved basanites. Evolved basanites 97 and 98 have different incompatible element characteristics than all other basanites and to each other, indicating that they are from different mantle sources or that some of these elements have not behaved completely incompatibly.

Table 6.2: Incompatible element ratios for Mount Morning rocks, possibly indicaing several mantle sources.

	Basanite	Evolved basanite (97)	Evolved basanite (98)	High Si basanite (118.H)	High Si basanite (86.A, 91, 124)	Trachyte (95)
Zr/Nb	3.59-4.37	4.44	4.48	3.73	4.72-4.78	6.18
Zr/Y	6.42-9.34	11.54	11.87	8.02	10.96-11.40	27.37
Zr/Rb	8.47-13.63	15.68	8.59	8.31	4.72-4.78	13.79

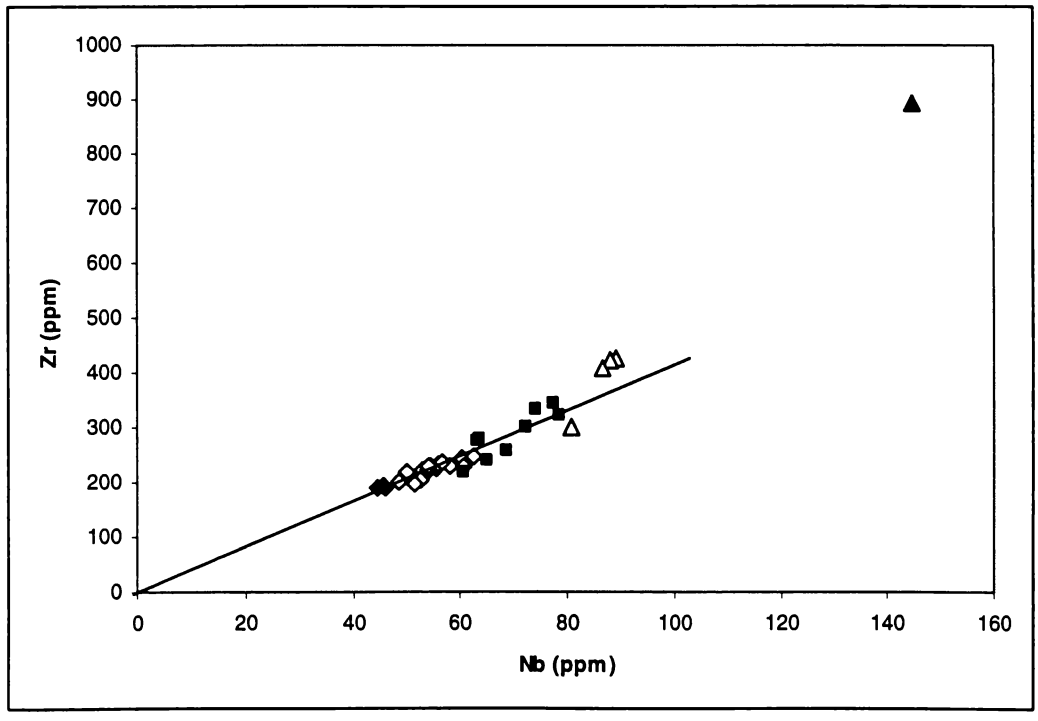

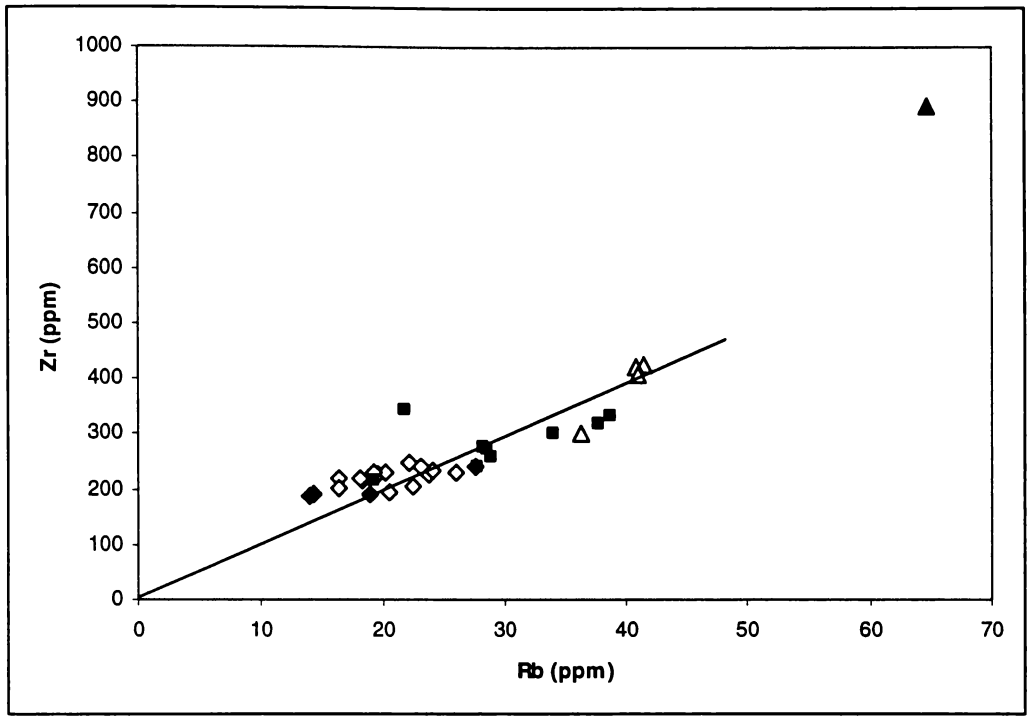

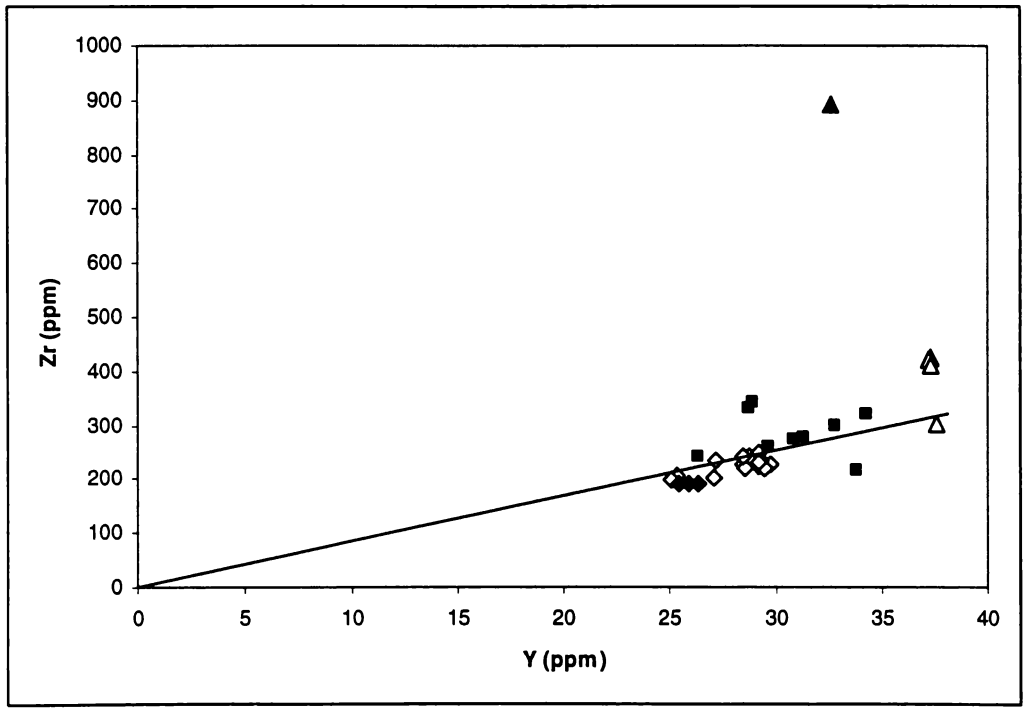

Fig.6.11: Incompatible element plots for basanite and trachytes. (Symbols as in Fig. 3.1)

Two different basanite–phonolite fractionation lineages have previously been identified in the Erebus Province *(Kyle, 1981)*;

- DVDP lineage (Dry Valley Drilling Project)
- Erebus lineage.

Lavas of the DVDP lineage have been described from the Dry Valley Drilling Project drill holes, Hut Point Peninsula and Brown Peninsula. The Erebus lineage is found throughout the Erebus and Discovery centres of the Erebus Province.

The Erebus lineage contains olivine, clinopyroxene and magnetite as the main fractionated phases *(Kyle, 1976; Kyle, 1981)*, with some apatite and feldspar (plagioclase in the intermediate lavas, anorthoclase in the phonolite). The DVDP lineage contains all the same phases as the Erebus lineage but with the addition of kaersutite. Kyle *(1981)* comments that the occurrence of kaersutite is possibly due to lower temperatures and higher water pressure.

The presence of amphibole in rocks of the evolved basanite group indicates that the primitive-evolved-high silica basanite fractionation sequence is part of the DVDP lineage. The unrelated low alkali basanites can not be assigned to either the DVDP or Erebus lineages because none of the more evolved members of this group were found. Even if they were part of the DVDP lineage, the absence of amphibole is expected because amphiboles are uncommon in the basanites of this lineage *(Kyle, 1981)*.

The amphiboles (probably kaersutite) in the evolved basanite group are found altered to pseudomorphic aggragates of olivine, pyroxene and opaques and are similar to others reported in alkaline volcanics elsewhere.

- Kaersutites reported by Kyle *(1981)* from the DVDP lineage were completely altered to olivine + pyroxene + plagioclase + magnetite + possibly rhonite.
- Kaersutites in the Dunedin Volcanics altered to aggregates of clinopyroxene, opaque oxides, feldspar and nepheline *(Coombs and Wilkinson, 1969).*

6.4 PRIMARY MAGMA ?

The primitive basanite group contains some very primitive rocks, they have undergone little fractionation during ascent from the mantle. Cook *(2005)* lists the features required for a sample to be considered a primary magma in equilibrium with a mantle source:

- Cognate peridotite xenoliths
- Magnesium number >68
- MgO >11 wt %
- Ni >300 ppm

No sample meets all these criteria, but the sample closest to being a primary magma is one of the following;

- Sample 45: peridotite microinclusions
  magnesium number of 63.0
  MgO of 11.38 wt%, Ni of 288 ppm.
- Sample 74: abundant large peridotite xenoliths
  magnesium number of 63.6
  MgO of 10.27 wt%, Ni of 206 ppm
- Sample 93: peridotite microinclusions
  magnesium number of 64.7
  MgO of 10.58 wt%, Ni of 184 ppm

The magnesium number is a measure of how evolved a rock is relative to a magma in equilibrium with a mantle source. According to Green *(1970)* a "liquid formed in equilibrium with pyrolite source rock must be very magnesian (Mg# 68-73)". The magnesium number is calculated as (mol Mg / Mg +Fe) *100. The theoretical 'initial magma' of Sato *(1977)* has NiO and MgO contents of 0.0398 and 11.3 wt% respectively. The hypothetical 'pyrolite' upper mantle of Green *(1970)* has a magnesium number of 89, depletion of magnesium through incorporation into fractionated olivine causes the magnesium number to decrease (Fig 6.12). High magnesium and nickel values indicate a primitive rock because both of these are rapidly depleted by the fractionation of olivine. This evidence suggests that none of the basanites occurring in the field area are true primary magmas, but some (e.g. samples 45, 74, 93) are very primitive.

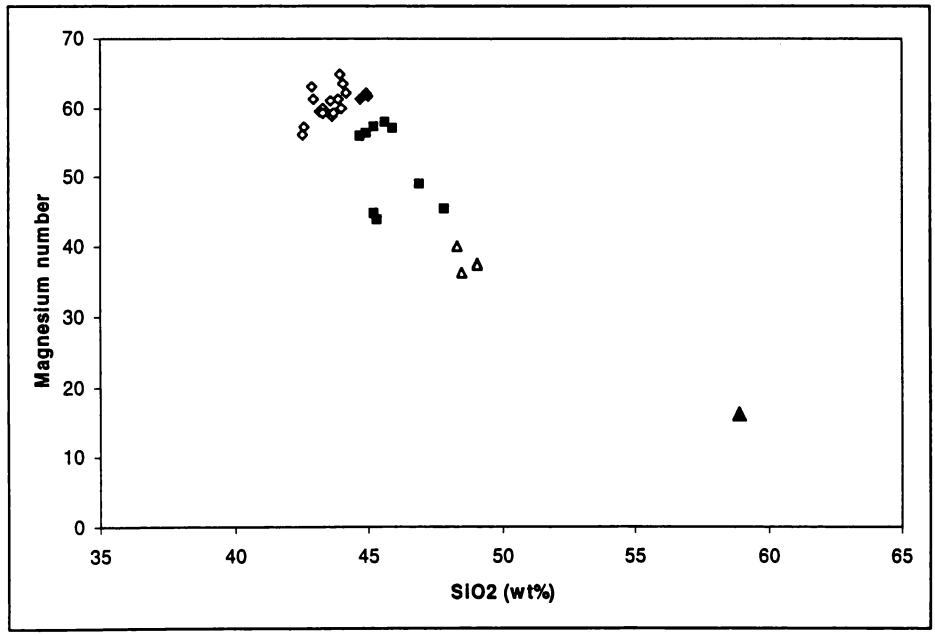

Fig.6.12: Magnesium number plotted against silica for mount Morning samples.

REFERENCES

Armstrong, R.L., 1978. K-Ar dating: Late Cenozoic McMurdo Volcanic Group and dry valley glacial history, Victoria Land, Antarctica. *New Zealand Journal of Geology and Geophysics* 21 (6), 685-698.

Bailey, D.K., 1987. Mantle metasomatism – perspective and prospect. In: Fitton, J.G. and Upton, B.G.J. (Eds), *Alkaline Igneous Rocks*, Blackwell Scientific Publications, 1-14.

Bardsley, C.J. 2004. Physical volcanology of Red Crater, Tongariro. *MSc Thesis*, University of Waikato.

Barker, D.S., 2000. Emplacement of a xenolith rich sill, Lajitas, Texas. *Journal of Volcanology and Geothermal Research* 104, 153-168.

Bernstein, S., Leslie, A.G., Higgins, A.K. and Brooks, C.K., 2000. Tertiary alkaline volcanics in the Nunatak Region, Northeast Greenland: new observations and comparison with Siberian maymechites. *Lithos* 53, 1-20.

Berg, J.H., 1991. Geology, petrology and tectonic implications of crustal xenoliths in Cenozoic volcanic rocks of southern Victoria Land. In: Thomson, M.R.A, Crame, J.A. and Thomson, J.W. (Eds), *Geological Evolution of Antarctica*, Cambridge University Press, 311-315.

Bryan, W.B., Finger, L.W. and Chayes, F., 1969. Estimating proportions in petrographyc mixing equations by least squares approximation. *Science* 163, 926-927.

Buddington, A.F. and Lindsley, D.H., 1964. Iron-titanium oxide minerals and synthetic equivalents. *Journal of Petrol*ogy 5, 310-357.

Caldeira, R. and Munhá, J.M., 2002. Petrology of ultramafic nodules from São Tomé Island, Cameroon Volcanic Line (oceanic sector). *Journal of African Earth Sciences* 34, 231-246.

Carswell, D.A., 1980. Mantle derived lherzolite nodules associated with kimberlite, carbonatite and basaltic magmatism: a review. *Lithos* 13, 121-138.

Cas, R.A.F. and Wright, J.V. 1987. *Volcanic successions, modern and ancient.* Allen and Unwin, London.

Connor, C.B. and F.M. Conway, 2000, Basaltic Volcanic Fields, In: Sigurdsson, H. (Ed), *Encyclopedia of Volcanoes*. Academic Press, San Diego. 331-343.

Cook, C., Briggs, R.M., Smith, I.M.E. and Maas, R. 2005. Petrology and geochemistry of intraplate basalts in the South Auckland Volcanic Field, New Zealand: evidence for two coeval magma suites from distinct sources. *Journal of Petrology* 46 (3), 473-503.

Coombs, D.S. and Wilkinson, J.F.G. 1969. Lineages and fractionation trends in undersaturated volcanic rocks from the East Otago Volcanic Province (New Zealand) and related rocks. *Journal of Petrology* 10 (3), 440-501.

Coombs, D.S., Landis, C.A., Norris, R.J., Sinton, J.M., Born, D.J. and Craw, D., 1976. The Dun Mountain ophiolite belt, New Zealand, its tectonic setting, constitution, and origin, with special reference to the southern portion. *American Journal of Science* 276, 561-603.

Eggins, S.M., Woodhead, J.D., Kinsley, L.P.J., Mortimer, G.E., Sylvester, P. McCulloch, M.T., Hergt, J.M. and Handler. M.R. 1997. A simple method for the precise determination of >40 trace elements in geological samples by ICPMS using enriched isotope internal standardisation. *Chemical Geology* 134, p311-326.

Frey, F.A. and Prinz, M., 1978. Ultramafic inclusions from San Carlos, Arizona: Petrologic and geological data bearing on their petrogenesis. *Earth and Planetary Science Letters* 38, 129- 176.

Gamble, J.A., McGibbon, F., Kyle, P.R., Menzies, M.A., and Kirsch, I., 1988. Metasomatised xenoliths from Foster Crater, Antarctica: implications for lithospheric structure and processes beneath the Transantarctic Mountain Front. *Journal of Petrology Special Issue Lithosphere Edition.* 109-138.

Goldich, S.S. Treves, S.B., Suhr, N.H. and Stuckless, J.S. 1975. Geochemistry of the Cenozoic volcanic rocks of Ross Island and vicinity, Antarctica. *Journal of Geology* 83, 415-435.

Green, D.H. 1970. The origin of basaltic and nephelinitic magmas. *Transactions of the Leinster Literary and Philosophical Society* LXIV.

Haggerty, S.E., 1981. Opaque mineral oxides in terrestrial igneous rocks. In: Rumble, D. (Ed), *Reviews in mineralogy Vol. 3: oxide minerals*. Mineralogical society of America.

Hall, A., 1987. *Igneous Petrology*. Longman Scientific and Technical.

Hancock, P.L. and Skinner, B.J. (Eds), 2000. *The Oxford companion to the Earth.* Oxford University Press.

Harte, B., 1977. Rock nomenclature with particular relation to deformation and recrystallisation textures in olivine-bearing xenoliths. *Journal of Geology* 85, 279-288.

Head J.W. and Wilson, L.,1989. Basaltic pyroclastic eruptions: influence of gas-release patterns and volume fluxes on fountain structure, and the formation of cinder cones, spatter cones, rootless flows, lava ponds and lava flows. *Journal of Volcanology and Geothermal Research* 37, 261-271.

Herve, F., Lobato, J., Ugalde, I. and Parkhurst, R.J., 1996. The geology of Cape Dubouzet, northern Antarctic Peninsula: continental basement to the Trinity Peninsula Group ? *Antarctic Science* 8, 407-414.

Irving, A.J., 1980. Petrology and Geochemistry of Composite Ultramafic xenoliths in alkali basalts and implications for magmatic processes within the mantle. *American Journal of Science* 280-A, 389-426.

Irving, A.J. and Frey, F.A., 1984. Trace element abundances in megacrysts and their host basalts: Constraints on partition coefficients and megacryst genesis. *Geochimica et Cosmochimica Acta* 48, 1201-1221.

Jackson, E.D., 1969. Chemical variation in coexisting chromite and olivine in chromitite zones of the Stillwater Complex. In: Wilson, H.D.B. (Ed), Magmatic ore deposits. *Economic Geology Monograph* 4, 41-71.

Johnston, A.D., Stout, J.H. and Murthy, V.R., 1985. Geochemistry and origin of some unusually oxidized alkaline rocks from Kauai, Hawaii. *Journal of Volcanology and Geothermal Research* 25, 225-248.

Kalamarides, R.I. and Berg, J.H., 1991. Geochemistry and tectonic implications of lower-crustal granulites included in Cenozoic volcanic rocks of southern Victoria Land. In: Thomson, M.R.A, Crame, J.A. and Thomson, J.W. (Eds), *Geological Evolution of Antarctica*, Cambridge University Press, 305-309.

Keller, R.A. and Strelin, J.A., 1992. Alkalic basalts and ultramafic xenoliths on James Ross Island, Antarctic Peninsula. *Antarctic Journal of the U.S.* 27 (5), 22-23.

Kamber, B.S., Greig, A., Schoenberg, R., and Collerson. K.D., 2005. A new estimate for the composition of weathered young upper continental crust from alluvial sediments, Queensland, Australia. *Geochimica Cosmochimica Acta*, 69, 1041-1058.

Kudo, A.M. and Weill, D.F., 1970. An igneous plagioclase thermometer. *Contributions to Mineralogy and Petrol*ogy 25, 52-65.

Kukkonen, I.T. and Peltonen, P., 1999. Xenolith-controlled geotherm for the central Fennoscandian Shield: implications for lithosphere–asthenosphere relations. *Tectonophysics* 304, 301-315.

Kyle, P.R. and Cole, J.W., 1974. Structural control on volcanism in the McMurdo Volcanic Group, Antarctica. *Bulletin Volcanologique* 38 (1), 16-25.

Kyle, P.R. 1976. Geology, Mineralogy and Geochemistry of the Late Cenozoic McMurdo Volcanic Group, Victoria Land, Antarctica. *PhD Thesis*, Victoria University of Wellington.

Kyle, P.R. and Rankin, P.C. 1976. REE geochemistry of late Cenozoic alkaline lavas of the McMurdo Volcanic Group, Antarctica. *Geochimica Cosmochimica Acta* 40, 1497-1507.

Kyle, P.R. Adams, J. and Rankin, P.C., 1979. Geology and petrology of the McMurdo Group at Rainbow Ridge, Brown Peninsula. *Geological Society of America Bulletin, Part 1* 90, 676-688.

Kyle, P.R., 1981. Mineralogy and geochemistry of a basanite to phonolite sequence at Hut Point Peninsula, Antarctica, based on core from the Dry Valley Drilling Project Drillholes 1,2 and 3. *Journal of Petrology* 22 (4), 451-500.

Kyle, P.R., Wright, A. and Kirsch, I., 1987. Ultramafic xenoliths in the late Cenozoic McMurdo Volcanic Group, western Ross Embayment, Antarctica. In: Nixon, P.H. (Ed), *Mantle Xenoliths*, Wiley-Interscience.

Kyle, P.R., 1990a. McMurdo Volcanic Group. In LeMasurier, W.E. and Thompson, J.W. (Eds), *Volcanoes of the Antarctic Plate and Southern Oceans*. American Geophysical Union, Antarctic Research Series 48, 19-25.

Kyle, P.R., 1990b. Erebus volcanic Province. In LeMasurier, W.E. and Thompson, J.W. (Eds), *Volcanoes of the Antarctic Plate and Southern Oceans*. American Geophysical Union, Antarctic Research Series 48, 81-88.

Kyle, P.R., 1990c. Melbourne Volcanic Province. In LeMasurier, W.E. and Thompson, J.W. (Eds), *Volcanoes of the Antarctic Plate and Southern Oceans*. American Geophysical Union, Antarctic Research Series 48, 48-59.

Kyle, P.R., Moore, J.A. and Thirlwall, M.F., 1992. Petrologic evolution of anorthoclase phonolite lavas at Mount Erebus, Ross Island, Antarctica. *Journal of petrology* 33 (4), 849-875.

Lawver, L.A., Royer, J.-Y., Sandwell, D.T. and Scotese, C.R., 1991. Evolution of the Antarctic Continental Margins. In: Thomson M. R. A., Crames J. A. and Thomson J. W. (Eds). *Geological evolution of Antarctica.* Cambridge University Press, Cambridge, England.

LeBas, M.J., LeMaitre, R.W., Streckeisen, A. and Zanettin, B., 1986. A Chemical Classification of Volcanic Rocks Based on the Total alkali-Silica diagram. *Journal of Petrology* 27 (3), 745-750.

LeMasurier, W.E., 1990. Late Cenozoic Volcanism on the Antarctic Plate. In LeMasurier, W.E. and Thompson, J.W. (Eds), Volcanoes of the Antarctic Plate and Southern Oceans. *American Geophysical Union, Antarctic Research Series* 48, 1-17.

Lanyon, R., Varne, R. and Crawford, A.J., 1993. Tasmanian tertiary basalts, the Balleny plume, and the opening of the Tasman Sea (southwest Pacific ocean). *Geology* 21, 555-558

Le Roex A., Cliff, R.A. and Adair, J.I. 1990. Trista da Cunha, South Atlantic: Geochemistry and Petrogenesis of a Basanite-Phonolite Lava Series. *Journal of Petrology* 31 (4), 779-812.

McDonough W.F. and Sun, S. 1995. Chemical and isotopic systematics of oceanic basalts: implications for mantle composition and processes. *Chemical Geology* 120, 223-253.

McGibbon, F.M., 1991. Geochemistry and petrology of ultramafic xenoliths of the Erebus Volcanic Province. In: Thomson, M.R.A, Crame, J.A. and Thomson, J.W. (Eds), *Geological Evolution of Antarctica*, Cambridge University Press, 317-321.

McIntosh and Kyle, 1990. Hallet Volcanic Province. In LeMasurier, W.E. and Thompson, J.W. (Eds), *Volcanoes of the Antarctic Plate and Southern Oceans*. American Geophysical Union, Antarctic Research Series 48, 26-31.

Menzies, M., 1983. Mantle ultramafic xenoliths in alkaline magmas: evidence for mantle heterogeneity modified by magmatic activity. In Hawkesworth C.J. and Norry, M.J. (Eds), *Continental Basalts and Mantle Xenoliths*, Shiva Geology Series .

Moores, E.M. and Vine F.J., 1971. The Troodos Massif, Cyprus and other ophiolites as oceanic crust : evaluation and implications. *Philospophical Transactions of the Royal Society London A.* 268, 443-466.

Morimoto, N, Fabries, J., Ferguson, A.K., Ginzburg, I.V., Ross, M., Seifert, F.A. Zussman, Aoki, K. and Gottardi, G., 1988. Nomenclature of pyroxenes. *American Mineralogist* 73, 1123-1133.

Muncy, H.L., 1979. Geologic history and petrogenesis of alkaline volcanic rocks, Mount Morning, Antarctica. MS Thesis, Ohio State University, Columbus.

Pearson, D.G., Canil, D. and Shirey, S.B., 2004. Mantle samples included in volcanic rocks: xenoliths and diamonds. In Carlson, R.W. (Ed), *Treatise on Geochemistry, Vol. 2: The Mantle and Core*, Elsevier Pergamon, 172-260.

Pike, J.E.N. and Schwarzman, E.C, 1977. Classification of textures in ultramafic xenoliths. *Journal of Geology* 85, 49-61.

Price, R.C., Cooper, A.F., Woodhead, J.D. and Cartwright, I., 2003. Phonolitic diatremes within the Dunedin Volcano, South Island, New Zealand. *Journal of Petrology* 44 (11), 2053-2080.

Reid, A.M., Donaldson, C.H., Dawson, J.B., Brown, R.W. and Ridley, W.I., 1975. The Igwisi Hills extrusive 'kimberlites'. *Physics and Chemistry of the Earth*, Vol. 9, 199-218.

Rollinson, H.R., 1993. *Using geochemical data: evaluation, presentation, interpretation*. Longman Scientific & Technical.

Ross, J. V., 1983. The nature and rheology of the cordilleran upper mantle of British Columbia: Inferences from peridotite xenoliths. *Tectonophysics* 100, 321-357.

Sato, H. 1977. Nickel content of basaltic magmas: identification of primary magmas and a measure of the degree of olivine fractionation. *Lithos* 10, 113-120.

Schulze, D.J., 1987. Megacrysts in alkalic volcanic rocks. In: Nixon, P.H. (Ed), *Mantle Xenoliths*, Wiley-Interscience, 433-451.

Shaw, C.S.J. and Eyzaguirre, J.E., 2000. Origin of megacrysts in the mafic alkaline lavas of the West Eifel volcanic field, Germany. *Lithos* 50, 75-95.

Stuckless, J.S. and Erickson, R.L., 1976. Strontium isotopic geochemistry of the volcanic rocks and associated megacrysts and inclusions from Ross Island and vicinity, Antarctica. *Contributions to Mineralogy and Petrol*ogy 58, 111-126.

Sumner, J.M. 1998. Formation of clastogenic flows during fissure eruption and scoria cone collapse: the 1986 eruption of Izu-Oshima Volcano, eastern Japan. *Bulletin of Volcanology* 60, 195-213.

Sumner, J.M., Blake, S., Matela, R.J. and Wolff, J.A., 2005. Spatter. *Journal of Volcanology and Geothermal Research* 142, 49-65.

Sun, S. and Hanson, G.N. 1976. Rare earth element evidence for differentiation of McMurdo Volcanics, Ross Island, Antarctica. *Contributions to Mineralogy and Petrol*ogy. 54, 139-155.

Vergniolle, S. and Mangan, M., 2000. Hawaiian and strombolian eruptions. In: Sigurdsson, H. (Ed), *Encyclopedia of Volcanoes*. Academic Press, San Diego.

Verwoerd, W.J., Chevallier, L. and Thompson, J.W., 1990. Oceanic Islands on the Antarctic Plate. In LeMasurier, W.E. and Thompson, J.W. (Eds), *Volcanoes of the Antarctic Plate and Southern Oceans.* American Geophysical Union, Antarctic Research Series 48, 397-404.

Vespermann, D. and Schmincke, H.V. 2000. Scoria Cones and tuff rings. In: Sigurdsson, H. (Ed), *Encyclopedia of Volcanoes.* Academic Press, San Diego.

Wilshire, H.G. and Shervais, J.W., 1975. Al-augite and Cr-diopside ultramafic xenoliths in basaltic rocks from the Western United States. *Physics and Chemistry of the Earth* 9, 257–272.

Wolff, J.A and Sumner, J.M. 2000. Lava fountains and their products. In: Sigurdsson, H. (Ed), *Encyclopedia of Volcanoes*. Academic Press, San Diego.

Wörner, G., 1999. Lithosphere dynamics and mantle sources of alkaline magmatism of the Cenozoic West Antarctic Rift System. *Global and Planetary Change* 23, 61-77.

Wright-Grassham, A.C. 1987. *Volcanic geology, mineralogy and petrogenesis of the Discovery volcanic subprovince, southern Victoria land, Antarctica.* Ph.D Thesis, New Mexico Institute of Mining and Technology, Sorocco.

Wright and Kyle, 1987. Mount Morning. In LeMasurier, W.E. and Thompson, J.W. (Eds), *Volcanoes of the Antarctic Plate and Southern Oceans.* American Geophysical Union, Antarctic Research Series 48, 124-127.

Wysoczanski, R.J., Gamble, J.A., Kyle, P.R. and Thirlwall, M.F., 1995. The petrology of lower crustal xenoliths from the Executive Committee Range, Marie Byrd Land Volcanic Province, Antarctica. *Lithos* 36, 185-201.

Appendix 1.1 Analytical Techniques

Abundances of major elements and trace elements were determined by X-ray fluorescence (XRF) analysis for 33 samples using the Spectro X-Lab 2000 at the Department of Earth Sciences, University of Waikato on pressed powder pellets for majors and fused glass discs for traces. USGS Standard BHVO-2 was used for calibration.

Trace elements were analysed on 10 selected samples using a Varian Q-ICPMS at the School of Earth Sciences, University of Melbourne. Sample preparation and analytical procedures used were similar to those of Eggins *et al.* (1997). Two hotplate digestions of W-2, a USGS. diabase standard, were used for external calibration, details of which can be found in Kamber *et al.* (2005).

Minerals from six samples were analysed using the JEOL JXA 8600 superprobe at the Department of Geology, University of Otago. Operating conditions were;

accelerating voltage	15 kV
current	20 nA
beam diameter	5 μm

Calibrations performed using simple oxide standards for all elements except Na (albite), K (adularia) and Ca (wollastonite).

Appendix 1.2: Summary of analyses performed on samples from Mount Morning.

Rock type	Sample	Thin section	XRF, major & trace	ICP-MS, trace & REE	Electron microprobe, minerals analysed	
Low Alkali Basanite	21	✓	✓	✓	✓	Ol, Px, Felds, Opq
	86.B	✓	✓			
	88	✓	✓			
Primitive basanite	1	✓	✓			
	2	✓	✓	✓		
	12.B	✓	✓			
	22	✓	✓			
	24	✓	✓			
	30	✓	✓			
	32	✓	✓			
	45	✓	✓	✓	✓	Ol, Felds, Opq
	47.A	✓	✓			
	58.A.1	✓	✓			
	58.E.1	✓	✓			
	74	✓	✓			
	93	✓	✓			
	121	✓	✓			
	125	✓	✓			
	130	✓	✓			
Evolved Basanite	3	✓	✓	✓	✓	Ol, Px, Felds, Opq
	4.B	✓	✓			
	23	✓	✓	✓		
	28	✓	✓	✓		
	44	✓	✓			
	89	✓	✓			
	97	✓	✓	✓	✓	Ol, Px, Felds, Opq
	98	✓	✓	✓		
	122	✓	✓			
High Silica Basanite	86.A	✓	✓			
	91	✓	✓	✓	✓	Ol, Felds, Opq
	118.H		✓			
	124	✓	✓			
Trachyte	95	✓	✓	✓	✓	Ol, Px, Felds, Opq

Ol = olivine
Px = pyroxene
Felds = feldspar
Opq = opaque oxides

Rock type	Sample	Thin section	XRF, major & trace	ICP-MS, trace & REE	Electron microprobe
Harzburgite	V	✓			
Lherzolite	VIII	✓			
Lherzolite	IX	✓			
Dunite	X	✓			
Dunite	XI	✓			
Olivine websterite	IX	✓			
Olivine websterite	IV	✓			
Websterite	II	✓			
Granulite	III	✓			
Granulite	VI	✓			
Granite	VII	✓			

Appendix 2.1: Description of petrology from hand specimen and thin section.

Rock	Low alkali Basanite												Primitive Basanite							
Sample	21				86.B				88				1				2			
Hand specimen																				
Colour	Grey				Grey				Grey				Dark gray				Dark gray			
Texture	Porphyritic				Porphyritic				Porphyritic				Porphyritic				Porphyritic			
Phenocrysts	Ol, Px				Ol, Px				Ol, Px				Ol				Ol, Felds			
Vesicularity					<1 mm <2 %				<1 mm <1 %				<1 mm 5-30 %				<3 mm 5-40 %			
Thin Section																				
Groundmass					Opq, Px, Felds				Opq, Px, Felds				Felds, Px, Opq				Felds, Px, Opq, Ol?			
	M	**A**	**Sh**	**S**	**M**	**A**	**Sh**	**S**	**M**	**A**	**Sh**	**S**	**M**	**A**	**Sh**	**S**	**M**	**A**	**Sh**	**S**
Phenocrysts	Ol	50	Sub	3.5	Ol	60	Sub	3.5	Ol	70	Sub	4	Ol	80	Sub	2.5	Ol	45	Sub	1.5
	Px	45	Sub	1.75	Px	30	Sub	1.25	Px	30	Sub	0.5	Feld	20	Eu	0.75	Feld	35	Eu	1.25
mineral, abundance,	Feld	5	Sub	0.5	Feld	10	Sub	0.3	Feld	<1	Sub	0.25	Px	<1	An	0.5	Px	20	Sub	2.25
shape, size	Opq	<1	Sub	0.25	Opq	<2	An	0.1	Opq	<1	Sub	0.3	Opq	<1	An	0.1	Opq	<2	An	0.25
Comment					Occ. mantle micro-inclsions. Felds poor gmass				Felds poor gmass				Some alignment of felds in gmass							

M = mineral Ol = olivine
Px = pyroxene
Felds = feldspar
Opq = opaque oxides
Amph = amphibole
Ap = apatite

A = phenocryst abundance as a % of crystals

Sh = phenocryst shape Eu = euhedral
Sub = subhedral
An = anhedral

S = maximum size in mm

Rock	Primitive Basanite																			
Sample	12.B				22				24				30				32			
Hand specimen																				
Colour	Dark gray				Light gray				Gray				Gray				Gray/brown			
Texture	Porphyritic				Porphyritic				Porphyritic				Porphyritic				Porphyritic			
Phenocrysts	Ol, Px, Felds				Ol				Ol, Px				Ol, Px, Felds				Ol, Px, Felds			
Vesicularity	<1 mm		<10 %		<1 mm		<2 %										<2 mm		10-15 %	
Thin Section																				
Groundmass	Felds, Px, Opq				Felds, Px, Opq, Ol?				Felds, Px, Opq				Felds, Px, Opq				Felds, Px, Opq			
	M	**A**	**Sh**	**S**	**M**	**A**	**Sh**	**S**	**M**	**A**	**Sh**	**S**	**M**	**A**	**Sh**	**S**	**M**	**A**	**Sh**	**S**
Phenocrysts	Ol	60	Sub	4	Ol	40	Sub	1.25	Ol	70	Sub	4	Ol	60	Sub	2.5	Ol	70	Sub	2.5
	Feld	30	Eu	1	Px	40	Sub	0.75	Feld	20	Sub	0.75	Felds	20	Sub	0.75	Felds	20	Sub	0.5
min, abundance,	Px	10	Sub	1.25	Feld	15	Sub	0.5	Opq	10	An	0.2	Px	20	An	0.5	Opq	<5	An	0.1
shape, max size	Opq	<1	An	1.5	Opq	5	An	0.1	Px	<2	Sub	2.5	Opq	<2	Sub	0.25	Px	<5	An	0.75
Comment	Some alignment of felds in gmass												Felds rich and opq rich gmass variants							

Rock	Primitive Basanite																			
Sample	45				47.A				58.A.1				58.E.1				74			
Hand specimen																				
Colour	Gray				Gray				Gray				Gray				Gray			
Texture	Porphyritic				Porphyritic				Porphyritic				Porphyritic				Porphyritic			
Phenocrysts	Ol				Ol, Px, Felds				Ol, Px				Ol, Px, Felds				Ol, Px			
Vesicularity					<4 mm		5-15 %										<2 mm		5-15 %	
Thin Section																				
Groundmass	Felds, Px, Opq				Felds, Px, Opq				Felds, Px, Opq				Felds, Px, Opq				Felds, Px, Opq			
	M	**A**	**Sh**	**S**	**M**	**A**	**Sh**	**S**	**M**	**A**	**Sh**	**S**	**M**	**A**	**Sh**	**S**	**M**	**A**	**Sh**	**S**
Phenocrysts	Ol	90	Sub	5	Ol	60	Sub	3	Ol	95	Sub	3.5	Ol	50	Sub	3.5	Ol	85	Sub	2
	Felds	5	Eu	1	Px	35	An	2.5	Felds	2.5	Eu	0.5	Px	45	An	4.5	Px	10	An	1
min, abundance, shape, max size	Opq	5	An	0.5	Felds	5	Sub	1	Opq	2.5	An	0.25	Felds	5	Sub	0.75	Felds	5	Sub	0.5
					Opq	<1	An	0.1					Opq	<1	An	0.25	Opq	<1	An	0.1
Comment	Very ol rich				Occ. mantle micro-inclusions															

Rock	Primitive Basanite																Evolved Basanite			
Sample	93				121				125				130				3			
Hand specimen																				
Colour	Gray				Gray				Gray/brown				Gray				Gray			
Texture	Porphyritic				Porphyritic				Porphyritic				Porphyritic				Porphyritic			
Phenocrysts	Ol				Ol, Px, Felds				Ol, Px, Felds				Ol, Px, Felds				Ol, Px			
Vesicularity	<15 mm		10-20 %						5 mm		5%		<20 mm		10-15 %		<1 mm		10%	
Thin Section																				
Groundmass	Felds, Px, Opq				Felds, Px, Opq				Felds, Px, Opq				Felds, Px, Opq				Felds, Px, Opq			
	M	**A**	**Sh**	**S**	**M**	**A**	**Sh**	**S**	**M**	**A**	**Sh**	**S**	**M**	**A**	**Sh**	**S**	**M**	**A**	**Sh**	**S**
Phenocrysts	Px	45	Sub	4.5	Px	35	Sub	1	Px	50	Sub	0.75	Ol	50	Sub	3.5	Ol	85	Sub	2
	Ol	45	Sub	5.5	Ol	30	Sub	1.5	Ol	25	Sub	25	Px	45	An	4.5	Px	10	An	1
min, abundance,	Felds	10	Sub	1.5	Felds	30	Sub	5	Felds	20	Sub	20	Felds	5	Sub	0.75	Felds	5	Sub	0.5
shape, max size	Opq	<1	An	0.1	Opq	5	An	0.75	Opq	5	An	5	Opq	<1	An	0.25	Opq	<1	An	0.1
Comment	Alignment of vesicles				Feldspar poor groundmass				Extensive reaction rims on feldspars											

Rock	Evolved Basanite																			
Sample	4.B				23				28				44				89			
Hand specimen																				
Colour	Gray				Gray				Gray/brown				Gray				Gray			
Texture	Porphyritic				Porphyritic				Porphyritic				Porphyritic				Porphyritic			
Phenocrysts	Ol				Ol, Px, Felds				Ol, Px, Felds				Ol				Ol, Px, Felds			
Vesicularity	<2 mm		5-20 %		<2 mm		5-15 %		<30 mm aligned & elongated		10-15 %		<40 mm aligned & elongated		10-15 %					
Thin Section																				
Groundmass	Felds, Px, Opq				Felds, Px, Opq				Felds, Px, Opq				Felds, Px, Opq				Felds, Px, Opq			
	M	**A**	**Sh**	**S**	**M**	**A**	**Sh**	**S**	**M**	**A**	**Sh**	**S**	**M**	**A**	**Sh**	**S**	**M**	**A**	**Sh**	**S**
Phenocrysts	Px	45	Sub	4.5	Px	35	Sub	1	Px	50	Sub	0.75	Ol	100	Sub	1.25	Felds	35	Sub	6
	Ol	45	Sub	5.5	Ol	30	Sub	1.5	Ol	25	Sub	25					Px	30	Sub	5
	Felds	10	Sub	1.5	Felds	30	Sub	5	Felds	20	Sub	20					Ol	20	Sub	8
	Opq	<1	An	0.1	Opq	5	An	0.75	Opq	5	An	5					Opq	10	Sub	1.5
min, abundance, shape, max size																	Amph	<5	Sub	1
Comment	Alignment of vesicles				Feldspar poor groundmass				Extensive reaction rims on feldspars				Trachytic groundmass texture				Very large phenocrysts			

Rock	Evolved Basanite												High Silica Basanite							
Sample	97				98				122				86.A				91			
Hand specimen																				
Colour	Gray				Light gray				Gray				Dark red/brown				Gray			
Texture	Porphyritic				Porphyritic				Porphyritic				Aphyric				Aphyric			
Phenocrysts	Ol, Px, Felds				Felds, Px				Ol, Px, Felds				-							
Vesicularity																				
Thin Section																				
Groundmass	Felds, Px, Opq																			
	M	**A**	**Sh**	**S**	**M**	**A**	**Sh**	**S**	**M**	**A**	**Sh**	**S**	**M**	**A**	**Sh**	**S**	**M**	**A**	**Sh**	**S**
Phenocrysts	Felds	35	Sub	3.5	Felds	35	Sub	2.5	Ol	30	Sub	3.5	Felds	65	An	2.5	Felds	60	An	2.5
	Px	30	An	2	Px	25	Sub	2	Px	30	Sub	2.5	Ol	20	Sub	1.5	Ol	15	Sub	1.5
	Ol	30	sub	3.5	Ol	30	Sub	1.5	Felds	35	Sub	2.5	Opq	10	Sub	0.75	Opq	20	Sub	0.75
	Amph	5	An	4	Opq	5	Sub	3.5	Opq	5	An	1	Px	<1	Sub	0.75	Px	<1	Sub	0.75
min, abundance,	Opq	<2	An	8	Amph	<5	An	2.5					Ap	4	Eu	0.5	Ap	4	Eu	0.5
shape, max size	Ap	<1	Eu	0.5	Ap	<1	Eu	0.75												
Comment	Amph is pseudomophed, Mantle micro-inclusions, Calcite infills				Very similar to 97								Strongly trachytic texture				Strongly trachytic texture			

Rock	High Silica Basanite								Trachyte			
Sample	118.H				124				95			
Hand specimen												
Colour	Gray				Gray				Pale gray/brown			
Texture	Aphyric				Aphyric				Aphyric			
Phenocrysts												
Vesicularity												
Thin Section												
Groundmass												
	M	**A**	**Sh**	**S**	**M**	**A**	**Sh**	**S**	**M**	**A**	**Sh**	**S**
Phenocrysts					Felds	70	Sub	1	Felds	95	Sub	1.5
					Ol	25	Sub	1.25	Ol	<2	Sub	0.3
					Opq	5	Sub	0.75	Opq	<2	An	0.25
					Ap	<1	Eu	0.5	Px	<2	An	1.75
min, abundance, shape, max size												
Comment									Px are pale green, Extremely trachytic texture			

Appendix 2.2: Modal mineralogy of selected samples from each rock group.

Rock	Low Alkali Basanite	Primitive Basanite					Evolved Basanite			
Sample	86.B	12.B	30	45	47.A	58.A.1	3	44	89	97
Olivine	10.2	16.3	11.7	27.4	12.3	10.6	9.2	10.7	9.9	21.4
Pyroxene	7.7	3.4	2.2	-	1.9	0.1	3.0	21.5	12.3	4.0
Amphibole	-	-	-	-	-	-	-	-	-	5.8
Feldspar	9.3	14.6	13	7.0	5.5	4.4	33.2	42.6	17.7	42.7
Plagioclase	-	-	-	-	-	-	-	-	13.7	4.0
Opaque	3.3	2.2	7.0	2.2	2.3	4.1	7.3	19	4.1	19.9
Apatite	-	-	-	-	-	-	-	-	-	1.6
Calcite	-	-	-	-	-	-	-	-	-	0.4
Groundmass	65.3	53.9	62.1	62.1	66	78	37.5	-	35	-
Vesicles	4.2	9.5	4.0	1.3	12	2.6	9.8	6.2	7.3	6.2
Counts	600	1000	600	1000	1000	1000	600	600	1500	900

Rock	High Silica Basanite		Trachyte
Sample	91	124	95
Olivine	12.6	7.2	10.2
Pyroxene	-	0.3	14.2
Amphibole	-	-	-
Feldspar	61.6	25	73.7
Plagioclase	-	-	-
Opaque	19.8	5.0	6.0
Apatite	1.7	0.8	0.3
Calcite	4.3	2.7	-
Groundmass	-	59.0	-
Vesicles	-	-	-
Counts	600	600	600

Appendix 2.3: Normative compositions of Mount Morning rocks.

Rock	Low Alkali Basanite			Primitive Basanite						
Sample	21	86.B	88	1	2	12.B	22	24	30	32
Or	0.48	4.25	2.62	6.32	3.01	5.79	-	5.75	0.8	6.85
Ab	-	0.52	-	0.60	-	14.26	-	-	-	1.85
An	17.59	18.48	18.18	14.55	15.22	0.14	14.9	14.04	8.22	14.82
Lc	3.61	-	2.35	-	2.32	0.14	4.96	0.31	4.61	-
Ne	17.65	17.18	17.19	20.08	19.02	20.67	19.21	20.31	27.46	19.99
Di	32.42	31.64	32.33	25.22	24.81	26.1	31.24	26.03	29.78	24.4
Ol	19.29	20.01	19.26	22.56	24.72	21.99	17.72	22.9	18.63	21.37
Mt	2.51	2.51	2.57	2.83	2.91	2.87	2.81	2.86	2.68	2.8
Il	4.65	4.65	4.71	6.78	7.01	7.08	7.18	6.76	6.69	6.8
Ap	0.97	0.93	0.97	1.25	1.18	1.3	1.48	1.23	1.32	1.32

Rock	Primitive Basanite								
Sample	45	47.A	58.A.1	58.E.1	74	93	121	125	130
Or	3.35	7.21	6.8	4.34	-	2.14	1.22	3.56	6.38
Ab	-	0.82	1.02	-	-	-	-	-	-
An	13.29	14.83	11.59	12.09	14.15	15.65	14.3	14.92	15.01
Lc	1.96	-	-	1.93	5.7	4.16	4.19	2.77	0.56
Ne	19.67	19.13	22.96	21.64	19.48	17.56	20.31	19.57	20.17
Di	24.35	25.92	26.24	27.11	29.97	29.06	29.3	28.23	25.76
Ol	26.47	31.36	20.62	22.41	21.68	22.65	21.33	21.79	20
Mt	2.87	2.8	2.78	2.8	2.52	2.39	2.67	2.61	3
Il	7.03	6.78	6.82	6.59	5.2	5.07	5.6	5.47	8.07
Ap	1.2	1.34	1.37	1.3	1.23	1.48	1.27	1.27	1.27

Rock	Evolved Basanite								
Sample	3	4.B	23	28	44	89	97	98	122
Or	9.87	10.76	8.86	8.16	8.27	6.56	9.63	9.81	9.28
Ab	12.30	16.44	2.8	4.04	4.42	7.68	9.54	10.94	4.85
An	11.35	8.71	13.2	12.93	13.04	18.36	7.42	11.43	14.15
Lc	-	-	-	-	-	-	-	-	-
Ne	20.7	21.85	21.63	21.6	21.17	16.24	26.41	21.03	21.07
Di	23.27	20.7	28.01	24.6	24.04	22.46	23.16	20.99	25.05
Ol	12.27	11.18	16.58	18.46	18.91	18.91	11.89	13.64	16.91
Mt	2.51	2.48	2.45	2.73	2.71	2.58	2.84	2.91	2.46
Il	5.72	5.62	5.15	6.21	6.12	5.41	7.05	7.22	5.13
Ap	2.18	2.46	1.48	1.48	1.51	1.99	2.22	2.25	1.27

Rock	High Silica Basanite				Trachyte
Sample	86.A	91	118.H	124	95
Or	12.82	13.06	12.53	12.65	23.34
Ab	24.09	23.17	22.07	21.08	37.26
An	5.73	5.81	6.98	3.2	-
Lc	-	-	-	-	-
Ne	19.36	19.76	18.8	23.05	17.31
Di	16.02	16.14	16.07	18.74	9.86
Ol	10.83	10.89	12.01	9.81	5.6
Mt	2.54	2.58	2.62	2.64	-
Il	5.17	5.17	5.37	5.37	1.23
Ap	3.61	3.59	3.73	3.66	0.58

Appendix 2.4a: Electron microprobe analyses of olivines in Mount Morning rocks

Rock	Low Alkali basanite					Primitive Basanite						
Sample	21	21	21	21	21	45	45	45	45	45	45	45
Position	C	C	C	R	R	C	C	C	C	C	C	R
SiO_2	38.24	39.89	40.22	37.44	38.30	38.05	38.41	38.75	39.42	38.99	38.81	36.77
Al_2O_3	0.00	0.00	0.00	0.00	0.00	0.00	0.00	0.00	0.14	0.00	0.00	0.00
FeO*	19.82	14.53	14.95	27.01	21.50	19.22	14.04	18.82	14.47	15.62	15.09	26.59
MnO	0.26	0.19	0.23	0.60	0.36	0.16	0.07	0.17	0.10	0.06	0.12	0.23
MgO	41.17	45.04	45.13	34.41	38.71	40.67	45.01	41.18	44.56	44.30	44.51	34.48
CaO	0.25	0.33	0.30	0.44	0.41	0.13	0.12	0.13	0.13	0.12	0.12	0.14
Total	99.77	99.98	100.83	99.93	99.26	98.21	97.68	99.07	98.85	99.09	98.68	98.27

Rock	Evolved Basanite						High Silica Basanite			Trachyte	
Sample	3	3	3	97	97	97	91	91	91	95	95
Position	C	C	R	C	C	R	C	C	C	C	C
SiO_2	35.55	37.93	37.83	37.69	37.93	37.46	33.91	34.18	36.07	30.40	30.67
Al_2O_3	0.00	0.00	0.00	0.00	0.00	0.00	0.00	0.00	0.05	0.00	0.67
FeO*	22.26	23.58	22.46	22.08	22.36	25.48	38.95	36.35	28.61	50.32	50.90
MnO	0.15	0.16	0.14	0.30	0.29	0.66	1.35	1.20	0.70	3.12	3.04
MgO	38.59	38.55	38.47	38.70	38.72	36.12	23.39	25.41	32.25	10.95	9.72
CaO	0.08	0.09	0.11	0.20	0.18	0.23	0.25	0.27	0.47	0.84	1.13
Total	96.64	100.31	99.01	99.00	99.49	99.98	97.85	97.46	98.20	95.67	96.64

All values are as weight percents. C = core, R = rim

Appendix 2.4b: Electron microprobe analyses of clinopyroxenes in Mount Morning rocks

Rock	Low Alkali Basanite			Evolved Basanite								
Sample	21	21	21	3	3	3	97	97	97	97	97	97
Position	C	C	C	C	C	C	C	C	R	C	C	R
SiO_2	45.83	49.91	48.12	49.43	46.79	44.49	48.39	47.50	47.30	43.94	44.98	45.47
TiO_2	2.43	1.26	1.78	1.42	2.39	3.26	1.81	2.32	2.41	3.73	3.18	3.00
Al_2O_3	8.68	4.75	6.90	3.26	6.15	8.11	5.09	6.44	6.25	10.65	9.45	9.14
FeO*	6.78	6.49	5.64	9.65	7.91	8.78	8.42	8.70	8.78	8.22	8.13	7.92
MnO	0.13	0.16	0.13	0.43	0.20	0.21	0.21	0.22	0.21	0.13	0.10	0.16
MgO	12.66	15.09	13.64	13.31	12.71	11.45	13.39	12.38	12.23	11.36	11.96	12.18
CaO	22.35	21.59	22.40	21.82	21.63	20.98	21.43	21.29	21.49	20.98	20.91	21.10
Na_2O	0.38	0.32	0.36	0.43	0.53	0.66	0.61	0.62	0.63	0.67	0.62	0.73
Total	99.25	99.57	98.96	99.75	98.31	97.93	99.35	99.50	99.29	99.68	99.32	99.71

Rock	Trachyte	
Sample	95	95
Position	C	C
SiO_2	47.47	49.68
TiO_2	1.01	0.45
Al_2O_3	2.05	0.96
FeO*	19.60	15.05
MnO	0.91	0.88
MgO	4.40	9.24
CaO	19.50	21.45
Na_2O	1.83	0.61
Total	96.86	98.31

All values are as weight percents. C = core, R = rim

Appendix 2.4c: Electron microprobe analyses of feldspars in Mount Morning rocks

Rock	Low Alkali Basanite		Primitive Basanite			Evolved Basanite				
Sample	21	21	45	45	45	3	3	3	3	3
Position	C	C	C	C	C	C	C	R	C	C
SiO_2	49.29	49.48	48.82	48.08	49.50	48.85	49.96	48.50	52.48	51.25
TiO_2	0.08	0.12	0.14	0.13	0.22	0.11	0.08	0.06	0.00	0.00
Al_2O_3	31.47	31.40	31.55	31.66	31.05	31.11	30.54	31.49	29.01	29.62
FeO*	0.82	0.79	0.40	0.60	0.49	0.52	0.48	0.51	0.08	0.06
CaO	15.15	15.28	15.35	15.57	14.09	15.14	14.21	15.15	11.81	12.43
Na_2O	2.69	2.70	2.96	2.89	3.34	3.03	3.45	2.94	4.87	4.44
K_2O	0.15	0.15	0.25	0.17	0.22	0.19	0.22	0.16	0.48	0.28
Total	99.68	99.96	99.47	99.14	98.94	98.96	98.95	98.84	98.72	98.07

Rock	Evolved Basanite									
Sample	97	97	97	97	97	97	97	97	97	97
Position	C	C	R	C	C	R	R	R	C	R
SiO_2	54.45	55.09	54.31	62.10	61.29	53.41	60.70	52.65	56.61	64.56
TiO_2	0.07	0.06	0.17	0.00	0.04	0.15	0.17	0.13	0.03	0.16
Al_2O_3	28.26	27.99	27.67	23.45	23.50	29.64	23.98	29.14	25.74	20.36
FeO*	0.31	0.45	0.39	0.16	0.17	0.29	0.45	0.49	0.29	0.46
CaO	11.00	10.61	10.42	4.93	5.08	12.19	6.68	12.22	7.99	2.29
Na_2O	4.87	4.96	5.23	7.47	7.54	4.45	7.09	4.30	6.41	5.70
K_2O	0.46	0.47	0.37	1.62	1.54	0.25	1.12	0.27	0.73	6.43
Total	99.42	100.02	98.57	99.77	99.16	100.38	100.26	99.18	97.83	100.05

Rock	High silica Basanite					Trachyte				
Sample	91	91	91	91	91	95	95	95	95	95
Position	C	C	C	C	C	C	C	C	C	C
SiO_2	52.88	54.82	54.00	57.05	56.72	59.56	59.56	60.03	59.32	63.34
TiO_2	0.13	0.50	0.14	0.24	0.28	0.03	0.03	0.03	0.05	0.10
Al_2O_3	27.72	22.44	27.61	25.22	25.22	24.07	24.36	23.72	24.25	21.01
FeO*	0.55	1.31	0.57	0.94	1.00	0.16	0.18	0.34	0.28	0.58
MnO	0.00	0.04	0.00	0.00	0.04	0.03	0.00	0.02	0.00	0.00
MgO	0.00	0.47	0.00	0.03	0.10	0.00	0.00	0.00	0.00	0.00
CaO	11.18	7.38	10.53	7.91	7.86	5.92	6.22	5.53	5.97	2.44
Na_2O	4.88	6.62	5.12	6.59	6.31	7.26	7.16	7.42	7.11	7.63
K_2O	0.29	2.84	0.35	0.50	0.83	1.03	1.05	1.23	1.01	3.36
Total	97.64	96.42	98.33	98.48	98.37	98.06	98.55	98.32	97.98	98.46

All values are as weight percents. C = core, R = rim

Appendix 2.4d: Electron microprobe analyses of opaque oxides in Mount Morning rocks

Rock	Low Alkali Basanite			Primitive Basanite				
Sample	21	21	21	45	45	45	45	45
Position	C	C	C	C	C	R	R	C
TiO_2	1.47	1.42	1.50	1.57	1.48	14.81	13.83	1.50
Al_2O_3	20.42	20.49	21.61	28.89	29.14	8.23	8.98	28.10
Cr_2O_3	40.06	40.20	38.97	29.89	29.48	18.60	20.35	30.09
FeO*	23.09	22.24	22.26	26.20	25.99	52.72	51.38	28.22
MnO	0.54	0.53	0.50	0.49	0.51	0.75	0.76	0.54
MgO	12.97	13.02	13.48	12.05	11.91	4.90	4.82	10.15
Total	98.55	97.91	98.33	99.09	98.52	100.00	100.11	98.60
Fe_2O_3	8.00	7.41	7.75	8.05	7.86	15.54	14.77	7.51
FeO	15.90	15.58	15.29	18.95	18.92	38.73	38.10	21.46

Rock	Evolved Basanite				Evolved Basanite			
Sample	3	3	3	3	97	97	97	97
Position	C	C	C	C	C	R	R	C
TiO_2	8.59	9.04	9.16	9.99	42.14	49.74	53.93	48.47
Al_2O_3	8.44	8.40	7.33	4.82	0.92	0.40	0.05	0.40
FeO*	64.99	65.38	65.73	67.44	50.44	43.29	40.28	44.47
MnO	0.30	0.28	0.31	0.41	0.81	0.91	0.89	0.88
MgO	5.83	5.65	5.40	4.47	4.85	5.33	5.52	5.35
Total	88.68	88.81	88.00	87.35	99.16	99.67	100.67	99.58
Fe_2O_3	40.22	39.67	40.03	40.34	0.00	0.00	0.00	0.00
FeO	28.80	29.68	29.71	31.14	50.44	43.29	40.28	44.47

Rock	High silica Basanite				Trachyte		
Sample	91	91	91	91	95	95	95
Position	C	C	C	C	C	C	C
TiO_2	20.75	30.25	19.64	20.53	18.07	17.89	17.96
Al_2O_3	2.51	1.92	2.76	2.75	1.40	1.47	1.45
FeO*	66.40	60.45	68.42	67.38	73.88	72.82	74.56
MnO	1.01	1.00	0.91	0.94	1.28	1.30	1.27
MgO	2.18	2.55	2.01	1.99	0.78	0.77	0.76
Total	92.90	96.61	93.99	93.68	95.51	94.29	96.08

Fe_2O_3	23.87	7.60	26.42	24.46	31.93	31.34	32.51
FeO	44.92	53.62	44.65	45.37	45.14	44.63	45.31

Appendix 3.1: Major element x-ray fluorescence analyses of Mount morning rocks.

Rock		Low Alkali Basanite			Primitive Basanite						
Sample		21	86.B	88	1	2	12.B	22	24	30	32
SiO_2	%	45.02	44.94	44.69	43.35	42.93	43.18	42.60	43.30	43.31	43.63
TiO_2	%	2.58	2.59	2.61	3.76	3.88	3.92	3.97	3.76	3.72	3.78
Al_2O_3	%	14.33	14.14	14.38	14.31	14.03	14.31	13.96	14.19	14.59	14.71
FeO*	%	11.50	11.55	11.64	13.10	13.24	13.03	12.84	13.10	12.33	12.85
MnO	%	0.18	0.18	0.18	0.20	0.19	0.19	0.20	0.19	0.19	0.20
MgO	%	9.37	9.59	9.33	9.80	10.54	9.68	8.71	9.88	9.06	9.26
CaO	%	12.87	12.82	12.91	10.48	10.46	10.68	12.71	10.59	10.34	10.34
Na_2O	%	2.82	3.02	2.82	3.32	3.12	3.38	3.23	3.33	4.66	3.41
K_2O	%	0.91	0.75	0.99	1.13	1.06	1.05	1.12	1.10	1.19	1.22
P_2O_5	%	0.43	0.43	0.44	0.56	0.54	0.57	0.67	0.56	0.62	0.61
Total	%	100	100	100	100.00	100.00	100.00	100.00	100.00	100.00	100.00
LOI	%	-0.36	-0.42	-0.41	-0.37	-0.63	-0.48	0.12	-0.60	-0.55	-0.25

Rock		Primitive Basanite								
Sample		45	47.A	58.A.1	58.E.1	74	93	121	125	130
SiO_2	%	42.88	43.69	44.00	43.59	44.04	43.94	43.89	44.19	42.57
TiO_2	%	3.90	3.77	3.75	3.66	2.91	2.89	3.11	3.04	4.46
Al_2O_3	%	13.57	14.18	14.51	13.97	14.05	13.82	14.18	14.26	14.55
FeO*	%	13.22	12.85	12.41	12.74	11.64	11.41	12.25	11.98	13.61
MnO	%	0.20	0.20	0.20	0.20	0.19	0.19	0.20	0.20	0.20
MgO	%	11.38	9.46	9.33	10.06	10.27	10.58	9.81	9.95	8.79
CaO	%	10.00	10.80	10.20	10.53	11.90	12.29	11.56	11.36	10.69
Na_2O	%	3.28	3.20	3.78	3.46	3.14	2.86	3.28	3.19	3.31
K_2O	%	1.04	1.27	1.21	1.19	1.30	1.36	1.16	1.26	1.25
P_2O_5	%	0.54	0.59	0.62	0.60	0.57	0.65	0.58	0.58	0.57
Total	%	100.00	100.00	100.00	100.00	100.00	100.00	100.00	100.00	100.00
LOI	%	-0.64	-0.42	-0.55	-0.44	1.14	0.06	-0.14	-0.05	-0.39

Rock Sample		Evolved Basanite								
		3	4.B	23	28	44	89	97	98	122
SiO_2	%	46.96	47.88	45.65	44.68	44.92	45.23	45.34	45.26	45.95
TiO_2	%	3.12	3.06	2.86	3.43	3.38	2.98	3.87	3.94	2.84
Al_2O_3	%	16.24	16.61	15.31	15.25	15.22	15.71	16.19	16.06	15.85
FeO*	%	11.25	11.08	11.19	12.43	12.32	11.63	12.79	13.11	11.20
MnO	%	0.20	0.22	0.21	0.20	0.20	0.20	0.20	0.20	0.20
MgO	%	5.47	4.64	7.75	7.96	8.02	7.89	5.05	5.38	7.52
CaO	%	9.63	8.56	11.03	10.07	9.92	10.90	8.85	9.08	10.31
Na_2O	%	4.41	4.98	3.80	3.88	3.89	3.38	5.02	4.27	3.89
K_2O	%	1.73	1.88	1.56	1.44	1.46	1.16	1.68	1.72	1.65
P_2O_5	%	0.99	1.10	0.65	0.66	0.68	0.91	1.01	0.99	0.58
Total	%	100.00	100.00	100.00	100.00	100.00	100.00	100.00	100.00	100.00
LOI	%	0.02	0.55	-0.08	-0.46	-0.43	-0.24	0.52	0.76	-0.27

Rock Sample		High Silica Basanite				Trachyte
		86.A	91	118.H	124	95
SiO_2	%	49.10	49.09	48.34	48.52	58.92
TiO_2	%	2.82	2.82	2.92	2.91	0.67
Al_2O_3	%	16.47	16.42	16.28	16.31	18.09
FeO*	%	11.45	11.53	11.73	11.80	7.40
MnO	%	0.24	0.24	0.24	0.24	0.25
MgO	%	3.49	3.47	3.94	3.38	0.72
CaO	%	7.39	7.39	7.70	7.55	2.72
Na_2O	%	5.17	5.18	5.01	5.45	6.90
K_2O	%	2.26	2.27	2.17	2.20	4.07
P_2O_5	%	1.62	1.60	1.67	1.63	0.27
Total	%	100.00	100.00	100.00	100.00	100.00
LOI	%	0.68	1.19	2.23	0.77	0.72

Appendix 3.2: Trace element x-ray fluorescence analyses of Mount morning rocks.

Rock		Low Alkali Basanite			Primitive Basanite						
Sample		21	86.B	88	1	2	12.B	22	24	30	32
S	ppm	47	86	37	12.1	165	43	252	46	11.0	78
Cl	ppm	420	309	398	322	438	450	724	466	607	423
Ti	%	1.62	1.60	1.65	2.41	2.40	2.47	2.48	2.34	2.35	2.35
V	ppm	340	349	347	330	333	346	407	335	376	331
Cr	ppm	400	403	351	363	380	369	347	406	331	315
Ni	ppm	148	162	124	176	197	170	114	195	168	169
Cu	ppm	67	63	64	47	47	65	73	52	30	49
Zn	ppm	87	84	88	95	92	92	89	92	89	90
Ga	ppm	21	19.2	21	20	20	19.4	20	19.6	21	20
Br	ppm	1.4	1.1	1.1	1.8	1.7	1.2	1.7	1.3	1.5	1.3
Rb	ppm	18.9	13.9	14.3	19.2	20	16.4	24	18.3	19.2	20
Sr	ppm	554	554	556	816	802	815	924	784	835	843
Y	ppm	26	25	26	29	30	29	29	29	29	29
Zr	ppm	190	190	191	228	226	221	228	218	230	232
Nb	ppm	46	45	46	54	55	53	58	50	54	56
Mo	ppm	3.0	3.0	2.7	2.8	3.3	4.0	3.8	4.7	3.2	3.6
Ba	ppm	253	251	249	286	293	292	353	269	295	298
La	ppm	25	24	24	26	27	27	31	25	29	29
Ce	ppm	54	56	58	64	68	67	76	63	69	68
Nd	ppm	24	28	23	36	33	34	38	32	31	40
Hf	ppm	3.5	3.7	< 3.2	3.8	2.6	< 3.3	3.2	< 3.1	< 2.8	3.3
Pb	ppm	1.4	1.2	0.8	0.8	1.7	1.0	1.9	1.4	1.6	1.6
Th	ppm	5.0	4.7	3.8	3.2	3.4	4.1	4.4	4.3	4.1	4.5
U	ppm	4.4	3.7	4.5	3.2	3.4	3.7	3.4	4.3	3.4	2.9

Rock Sample		Primitive Basanite								
		45	47.A	58.A.1	58.E.1	74	93	121	125	130
S	ppm	73	199	98	67	123	95	255	155	103
Cl	ppm	418	673	676	528	750	482	488	383	159
Ti	%	2.41	2.35	2.39	2.37	1.83	1.79	1.84	1.80	2.77
V	ppm	320	338	310	329	317	320	300	287	357
Cr	ppm	695	480	443	474	702	552	379	338	360
Ni	ppm	288	187	185	200	206	184	190	135	132
Cu	ppm	39	57	48	52	59	47	54	54	44
Zn	ppm	97	95	97	97	87	90	91	88	96
Ga	ppm	19.4	21	19.9	19.5	18.5	18.9	18.4	18.1	19.2
Br	ppm	1.3	1.8	1.7	1.4	1.7	1.4	1.0	1.5	0.6
Rb	ppm	16.4	23	22	28	24	26	22	21	18.1
Sr	ppm	872	895	944	887	677	715	818	830	990
Y	ppm	27	29	29	29	27	29	25	25	30
Zr	ppm	202	243	248	242	235	229	205	197	220
Nb	ppm	49	60	62	60	57	61	53	52	54
Mo	ppm	2.9	4.7	4.3	4.1	3.2	3.4	3.2	3.5	3.3
Ba	ppm	307	347	365	343	318	378	405	425	344
La	ppm	22	30	31	31	29	32	30	32	24
Ce	ppm	60	72	76	75	69	73	68	70	65
Nd	ppm	32	35	36	38	35	36	37	31	32
Hf	ppm	2.4	2.8	3.0	3.6	5.2	3.3	< 3.1	3.7	2.5
Pb	ppm	1.5	2.1	1.1	1.8	2.1	2.6	1.6	1.8	1.3
Th	ppm	3.0	4.5	5.7	4.8	6.1	5.7	5.0	5.0	3.9
U	ppm	3.1	3.3	3.1	2.6	3.9	3.3	3.3	2.6	2.8

Rock Sample		Evolved Basanite								
		3	4.B	23	28	44	89	97	98	122
S	ppm	1359	113	472	399	2858	115	276	600	162
Cl	ppm	753	837	744	495	528	78	698	725	337
Ti	%	1.95	1.88	1.78	2.08	2.07	1.91	2.42	2.34	1.70
V	ppm	222	223	250	284	269	259	247	263	238
Cr	ppm	78	19	316	237	265	175	9.1	8.0	226
Ni	ppm	37	15	103	118	120	71	22	27	108
Cu	ppm	31	23	45	45	43	37	28	31	44
Zn	ppm	92	95	95	86	90	97	85	84	91
Ga	ppm	19.9	20	21	20	20	21	20	20	19.9
Br	ppm	2.0	1.8	2.5	1.3	1.5	0.4	2.1	2.1	1.2
Rb	ppm	34	38	29	28	29	19.2	22	39	28
Sr	ppm	922	970	867	909	903	804	1305	1250	973
Y	ppm	33	34	30	31	31	34	29	29	26
Zr	ppm	300	321	258	277	274	217	343	332	240
Nb	ppm	73	79	69	63	63	61	77	74	65
Mo	ppm	4.2	9.2	4.2	3.0	3.2	3.1	4.2	3.9	3.9
Ba	ppm	542	676	496	392	390	394	575	572	648
La	ppm	46	51	40	43	36	39	48	47	38
Ce	ppm	103	108	86	94	84	90	107	107	85
Nd	ppm	42	52	32	35	37	46	47	43	37
Hf	ppm	6.8	6.2	3.5	4.2	4.6	3.8	5.8	2.8	3.1
Pb	ppm	3.7	4.3	3.2	3.1	3.0	2.2	3.9	2.2	2.8
Th	ppm	6.7	6.8	6.7	7.3	6.5	4.9	5.5	5.6	6.1
U	ppm	3.2	3.3	3.5	3.2	4.1	3.0	2.1	1.2	2.4

Rock		High Silica Basanite				Trachyte
Sample		86.A	91	118.H	124	95
S	ppm	395	864	260	189	96
Cl	ppm	1113	783	915	1075	1061
Ti	%	1.70	1.68	1.80	1.82	0.40
V	ppm	140	146	143	147	32
Cr	ppm	< 1.3	< 1.3	< 1.3	< 1.3	< 0.9
Ni	ppm	4.1	2.1	3.0	2.6	2.9
Cu	ppm	6.1	4.9	5.3	4.7	4.3
Zn	ppm	103	101	102	105	111
Ga	ppm	20	19.5	19.7	19.5	24
Br	ppm	2.8	2.3	2.1	2.6	3.1
Rb	ppm	42	41	36	41	65
Sr	ppm	1484	1477	1465	1492	704
Y	ppm	37	37	38	37	33
Zr	ppm	425	422	302	409	892
Nb	ppm	89	88	81	87	145
Mo	ppm	5.1	4.9	4.1	5.8	5.9
Ba	ppm	625	626	603	616	1052
La	ppm	59	62	63	64	96
Ce	ppm	134	134	136	138	176
Nd	ppm	66	59	67	70	60
Hf	ppm	7.5	6.4	6.0	8.0	15.8
Pb	ppm	3.8	3.4	3.7	3.4	6.5
Th	ppm	8.7	8.2	7.2	7.6	16.0
U	ppm	< 1.5	< 1.5	< 1.5	1.2	3.5

Appendix 3.3: Trace and rare earth element analyses of Mount Morning rocks analysed by ICP-MS.

Rock		Low Alkali Basanite	Primitive Basanite		Evolved Basanite					High Silica Basanite	Trachyte
Sample		21	2	45	3	23	28	97	98	91	95
Li	ppm	4.84	4.61	4.74	7.51	6.76	7.25	4.90	6.14	6.23	6.14
Be	ppm	1.24	1.34	1.28	1.97	1.69	1.83	1.93	1.89	2.46	1.89
CaO	wt%	12.31	10.10	9.71	9.26	10.62	9.69	8.67	8.73	7.14	8.73
Sc	ppm	33.34	25.33	22.79	19.02	23.79	22.53	16.42	17.29	11.62	17.29
Ti	ppm	14605.90	21951.27	21871.54	17622.15	16066.64	19283.83	22035.74	22130.56	15625.52	22130.56
V	ppm	287.81	291.07	268.53	191.37	221.18	247.25	213.96	224.68	86.09	224.68
Cr	ppm	316.41	339.29	493.25	81.60	277.38	230.34	24.82	28.89	0.04	28.89
MnO	wt%	0.18	0.19	0.19	0.20	0.20	0.19	0.20	0.19	0.23	0.19
Ni	ppm	128.13	199.43	245.42	34.81	89.45	116.79	22.46	24.76	0.61	24.76
Cu	ppm	61.89	38.90	33.87	25.86	37.88	36.17	25.32	23.96	2.17	23.96
Zn	ppm	58.10	44.54	68.37	67.07	80.72	52.99	31.76	37.28	81.18	37.28
Ga	ppm	18.19	17.71	16.76	19.37	19.06	18.50	18.53	18.42	18.66	18.42
As	ppm	1.08	1.15	1.32	2.13	1.95	1.82	2.12	1.58	2.60	1.58
Rb	ppm	19.91	17.81	17.99	34.00	29.10	28.50	30.75	32.16	40.75	32.16
Sr	ppm	561.17	787.68	881.68	908.95	888.52	884.76	1266.72	1199.77	1421.41	1199.77
Y	ppm	22.93	24.92	24.58	29.54	26.21	27.77	26.37	26.33	34.69	26.33
Zr	ppm	184.18	205.50	195.02	284.56	245.30	259.59	325.84	329.63	397.72	329.63
Nb	ppm	46.78	52.14	49.83	74.38	69.16	65.50	78.97	77.65	89.40	77.65
Mo	ppm	2.12	2.01	2.19	3.27	3.21	2.24	3.22	3.17	3.87	3.17
Cd	ppm	0.07	0.10	0.09	0.14	0.16	0.13	0.19	0.13	0.16	0.13
Sn	ppm	1.46	1.80	1.70	2.08	1.87	1.94	2.09	1.93	2.37	1.93
Sb	ppm	0.04	0.03	0.04	0.08	0.06	0.06	0.15	0.15	0.10	0.15
Cs	ppm	0.21	0.18	0.19	0.43	0.34	0.27	0.37	0.33	0.41	0.33
Ba	ppm	263.39	278.79	319.78	549.92	518.39	390.51	603.88	580.39	638.09	580.39

Rock		Low Alkali Basanite	Primitive Basanite		Evolved Basanite					High Silica Basanite	Trachyte
Sample		21	2	45	3	23	28	97	98	91	95
La	ppm	30.86	32.11	31.63	54.31	47.67	44.70	57.97	57.24	70.09	57.24
Ce	ppm	65.02	70.12	70.48	111.06	96.29	92.12	118.60	117.01	147.68	117.01
Pr	ppm	8.04	8.95	9.16	13.71	11.71	11.10	14.58	14.46	18.86	14.46
Nd	ppm	32.05	36.59	37.89	53.62	45.14	43.10	56.01	55.67	75.13	55.67
Sm	ppm	6.48	7.57	7.78	9.97	8.40	8.25	9.99	9.96	13.71	9.96
Eu	ppm	2.08	2.49	2.58	3.32	2.88	2.61	3.38	3.34	4.71	3.34
Gd	ppm	5.95	6.92	7.03	8.54	7.26	7.26	8.17	8.17	11.31	8.17
Tb	ppm	0.87	0.99	1.00	1.19	1.03	1.05	1.11	1.10	1.51	1.10
Dy	ppm	4.82	5.38	5.36	6.36	5.61	5.76	5.81	5.81	7.76	5.81
Ho	ppm	0.93	1.02	1.01	1.20	1.07	1.12	1.07	1.08	1.42	1.08
Er	ppm	2.42	2.55	2.52	3.07	2.73	2.92	2.68	2.69	3.50	2.69
Tm	ppm	0.34	0.35	0.34	0.42	0.38	0.42	0.37	0.37	0.47	0.37
Yb	ppm	2.06	2.07	2.06	2.55	2.31	2.58	2.19	2.19	2.77	2.19
Lu	ppm	0.29	0.29	0.28	0.36	0.33	0.37	0.31	0.31	0.39	0.31
Hf	ppm	4.28	4.74	4.53	6.11	5.31	5.64	6.77	6.89	8.32	6.89
Tl	ppm	0.00	0.01	0.02	0.01	0.04	0.02	0.01	0.02	0.02	0.02
Pb	ppm	1.31	1.37	1.36	3.27	2.52	2.79	3.67	2.30	3.22	2.30
Th	ppm	3.17	2.99	2.81	5.43	4.89	4.99	5.26	5.27	6.50	5.27
U	ppm	0.95	1.14	0.83	1.63	1.49	1.38	1.57	1.57	1.92	1.57

Appendix 4.1: Modal mineralogy of xenoliths

Xenolith type	Peridotite				
	Harzburgite	Lherzolite		Dunite	
Sample	V	VIII	IX	X	XI
Olivine	67.9	44.5	52.0	88.2	47.6
Orthopx.	15.2	7.8	12.0	2.7	-
Clinopx.	1.8	37.2	18.5	-	-
Spinel	4.3	-	7.3	2.5	-
Opaque	-	7.0	0.3	-	47.0
Vesic.	10.8	3.5	10.0	6.7	6.4
Feldspar	-	rare	-	-	-
Quartz	-	-	-	-	-
Calcite	-	-	-	-	-
Glass	-	-	-	-	-
Count	600	600	600	600	600

Xenolith type	Pyroxenite			Crustal		
	Ol. Websterite		Websterite	Granulite	Granulite	Granite
Sample	I	IV	II	III	VI	VII
Olivine	16.5	19.8		-	-	-
Orthopx.	40.3	25.1	29.8	-	-	-
Clinopx.	29.2	44.4	52.5	48.5	42.3	-
Spinel	4.0	-	-		-	-
Opaque	-	1.0	-	18.8	13.0	-
Vesic.	6.7	9.0	17.8	8.0	5.8	10.7
Feldspar	rare	<0.1	-	9.0	17.0	18.7
Quartz	3.3	-	-	15.0	21.8	46.5
Calcite	-	-	-	0.7	-	-
Glass	-	-	-	-	-	24.7
Count	600	600	400	600	600	600

Appendix 5.1: GPS points of field locations

Location	Latitude	Longitude	Altitude (m)
1	78.37671	163.81	605
2	78.37794	163.79629	688
3	78.37679	163.79599	689
4	78.37680	163.79461	693
5	78.37615	163.79544	680
6	78.37459	163.78593	675
7	78.37522	163.78270	714
8	78.37552	163.77920	765
9	78.37488	163.78133	830
10	78.37356	163.79470	603
11	78.37458	163.79220	616
12	78.37532	163.80601	562
13	78.37343	163.79579	608
14	78.37319	163.79634	624
15	78.37285	163.79847	581
16	78.37284	163.80239	570
17	78.37170	163.80447	562
18	78.37095	163.80519	558
19	78.37013	163.80656	578
20	78.36892	163.80035	587
21	78.36750	163.80403	610
22	78.36897	163.80911	550
23	78.37300	163.80683	549
24	78.37341	163.81336	551
25	78.37294	163.81605	524
26	78.37316	163.81731	515
27	78.37271	163.82045	490
28	78.37232	163.83586	465
29	78.37319	163.82959	474
30	78.37348	163.82828	479
31	78.37442	163.82288	507
32	78.37405	163.81496	544
33 a	78.37752	163.81230	613
33 b	78.37783	163.81411	618
33 c	78.37785	163.81562	622
34	78.37846	163.80193	622
35	78.37887	163.80258	672
36	78.37920	163.80031	669
37	78.37980	163.80572	711
38	78.37952	163.80854	711
39	78.37935	163.80917	683
40	78.37927	163.81034	690
41	78.37658	163.81952	543
42	78.37563	163.82755	504
43	78.37642	163.83228	495
44	78.37678	163.83587	500
45	78.38068	163.83482	532
46	78.38063	163.83357	536
47	78.38062	163.82900	581
48	78.37975	163.82708	569
49	78.37972	163.82275	572
50	78.38045	163.81658	624

51	78.38090	163.81475	640
52	78.38368	163.80632	593
53	78.38367	163.80875	602
54	78.38287	163.80265	622
55	78.37983	163.81168	669
56	78.37980	163.81300	663
57	78.37994	163.81446	659
58 a	78.38181	163.80908	632
58 b	78.38160	163.81230	661
58 c	78.38165	163.81286	682
59 a	78.38227	163.80866	674
59 b	78.38201	163.80657	715
73	78.39720	163.83093	630
74	78.39837	163.82784	686
75	78.39951	163.82623	731
76	78.40120	163.82360	752
77	78.40171	163.82577	786
78	78.40210	163.82257	776
79	78.40232	163.81937	773
80	78.40347	163.81821	792
81	78.40313	163.82193	787
82	78.40350	163.83855	833
83	78.37753	163.78510	736
84	78.37679	163.78328	747
85	78.37655	163.77043	868
86	78.37622	163.76748	917
87	78.37592	163.76546	926
88	78.37539	163.76130	951
89	78.37678	163.76506	902
90	78.37701	163.76428	893
91	78.37721	163.76395	892
92	78.37766	163.76354	887
93	78.37797	163.76366	878
94	78.37884	163.76419	884
95	78.37921	163.76285	889
96	78.37978	163.76060	923
97	78.38028	163.75899	905
98	78.38194	163.75766	929
99	78.38320	163.77995	738
116	78.38381	163.79480	632
117	78.38457	163.79373	640
118	78.38487	163.79012	683
119	78.38481	163.78873	695
120	78.38479	163.78888	720
121	78.38464	163.78470	728
122	78.38472	163.78016	753
123	78.38628	163.77708	794
124	78.38613	163.77477	808
125	78.38348	163.78535	700
126	78.38278	163.78588	699
127	78.38192	163.78442	704
128	78.38304	163.78789	676
129	78.38424	163.78883	694